Ab initio study of silica and hydrated silica during giant impacts

Renata Brandelli Schaan

▶ To cite this version:

Renata Brandelli Schaan. Ab initio study of silica and hydrated silica during giant impacts. Earth Sciences. Ecole normale supérieure de lyon - ENS LYON, 2022. English. NNT : 2022ENSL0002 . tel-04048922

HAL Id: tel-04048922
https://theses.hal.science/tel-04048922

Submitted on 28 Mar 2023

Numéro National de Thèse : 2022ENSL0002

THÈSE
en vue de l'obtention du grade de Docteur, délivré par
L'ÉCOLE NORMALE SUPÉRIEURE DE LYON

École Doctorale N° 52
Physique et Astrophysique de Lyon

Discipline : Sciences de l'Univers

Soutenu publiquement le 02/09/2022 par :

Renata BRANDELLI SCHAAN

Ab initio study of silica and hydrated silica during giant impacts

Étude ab initio de la silice et de la silice hydratée pendant les impacts géants

---

Devant le jury composé de :

SVERJENSKY, Dimitri	Professeur des Universités	Johns Hopkins University	Rapporteur
BLANCHARD, Marc	Directeur de Recherche	Université de Toulouse III	Rapporteur
DANIEL, Isabelle	Professeure des Universités	Université Claude Bernard Lyon 1	Examinatrice
MICHAUT, Chloé	Professeure des Universités	École Normale Supérieure de Lyon	Examinatrice
ROSKOSZ, Mathieu	Professeur des Universités	Muséum National d'Histoire Naturelle	Examinateur
CARACAS, Razvan	Directeur de Recherche	Inst. Physique du Globe de Paris	Directeur de thèse

Abstract

The Moon Impact formation theory was first proposed in 1975 by Hartmann and Davis. To this day, it is still the prevalent theory to explain the unique aspects concerning the Earth-Moon system. Although well accepted in the scientific community, this theory is still subject of debate regarding the conditions of the impact and the resulting scenario. It is still challenging to encompass in a single solution the problematic aspects of chemical equilibration that took place post-impact. Different models of impact have been proposed over the years in order to address the aforementioned issues. These models often rely on equations of state to describe the behavior of the materials present in the Earth and the Moon. Equations of state (EOS) describe the distribution of materials' phases and they are used on collision models based in hydrodynamic simulations to predict the final composition. The use of precise EOS lead to more correct post-impact chemical models where phases can be estimated correctly.

The majority of minerals present on rocky bodies in the Solar System are SiO_2 based and they are the building blocks of the Earth and the Moon. In terms of composition, SiO_2 represents more than 44% of lunar mare basalts and highlands, and about 45% of Earth's primitive mantle. However similar in parts of their composition, Moon and Earth differ considerably when it comes to the presence of volatile elements, where H_2O is arguably the most relevant. The impart of energy given by the large impact is sufficient to melt and vaporize silicate minerals. It produces a silicate atmosphere, where physicochemical properties and geochemical signatures of the resulting scenario depend on the fractionation of liquid-vapor. The presence of volatiles can change the behavior of typical equations of state of silicate materials and eventually be responsible for increasing the amount of vapor and supercritical material in such conditions.

We aim to construct equations of state for the silica-water binary system and subsequently study structural and transport properties of such system, comparing the behavior of the main elements under different conditions. We employ ab initio molecular dynamics (AIMD) methods where forces and energy are calculated with density functional theory as implemented in the VASP® package. We start by building a supercell containing 72 molecules of SiO_2 and describe its behavior under temperatures from 4000 to 7000 K and densities from 0.2 to 2.33 g/cm^3. We follow by inserting 9, 18, 36 and 72 H_2O molecules inside the SiO_2 supercell to obtain four different water-silica ratios and compare changes in the thermodynamic behavior as well as potential effects in elemental structural and transport properties. We study the four systems at temperatures of 2000, 3000, 4000 and 5000 K and densities of 0.34 to 2.77 g/cm^3 depending on the system. We calculate the critical point of SiO_2 in between 5000 and 5500 K, from 0.6 to 0.85 g/cm^3 and 0.15 to 0.25 GPa. The presence of water has a direct effect on the placement of the critical point, reducing it in more than 2000 K at specific conditions. Our results show that supercritical state materials are often underestimated in moon forming hydrodynamic models, which may impact elemental mixing in the outcome of the Giant Impact.

Résumé

La théorie de la formation de la Lune par un impact géant a été proposée pour la première fois en 1975 par Hartmann et Davis. À ce jour, c'est toujours la théorie qui prévaut pour expliquer les aspects uniques concernant le système Terre-Lune. Bien qu'elle soit bien acceptée dans la communauté scientifique, cette théorie fait encore débat quant aux conditions de l'impact et au scénario qui en résulte. Il est toujours difficile d'intégrer au sein une solution unique les aspects problématiques de l'équilibrage chimique qui ont eu lieu après l'impact. Différents modèles d'impact ont été proposés au fil des années afin de résoudre les problèmes susmentionnés. Ces modèles s'appuient souvent sur des équations d'état (EOS) pour décrire le comportement des matériaux présents sur la Terre et la Lune. Les EOS décrivent la distribution des phases des matériaux et sont utilisées sur des modèles de collision basés sur des simulations hydrodynamiques pour prédire une composition finale. L'utilisation d'EOS précises conduit à des modèles chimiques post-impact plus exacts pour lesquels l'estimation des phases est plus rigoureuse.

La majorité des minéraux présents sur les corps rocheux du Système solaire sont à base de SiO_2 et sont les éléments constitutifs de la Terre et de la Lune. En termes de composition, SiO_2 représente plus de 44% des mare basaltes et des hauts plateaux lunaire, et environ 45% du manteau primitif de la Terre. Bien que similaires sur certains aspects de leur composition, la Lune et la Terre diffèrent considérablement en ce qui concerne la présence d'éléments volatils, où H_2O est sans doute le plus pertinent. L'apport d'énergie donné par le grand impact est suffisant pour faire fondre et vaporiser les minéraux silicatés. Il produit une atmosphère silicatée, dont les propriétés physico-chimiques et les signatures géochimiques du scénario résultant dépendent du fractionnement liquide-vapeur. La présence de volatils peut modifier le comportement des équations d'état typiques des matériaux silicatés et éventuellement être responsable de l'augmentation de la quantité de vapeur et de matériau supercritique dans de telles conditions.

Notre objectif est de construire des équations d'état pour le système binaire silice-eau afin d'en étudier les propriétés structurelles et de transport, en comparant le comportement des principaux éléments dans différentes conditions. Nous utilisons des méthodes de dynamique moléculaire ab initio (AIMD) où les forces et l'énergie sont calculées selon la théorie fonctionnelle de la densité telle qu'implémentée dans le package VASP. Nous commençons par construire une supercellule contenant 72 molécules de SiO_2 et décrivons son comportement sous des températures s'étendant de 4000 à 7000 K et des densités allant de 0,2 à 2,33 g/cm^3. Nous insérons 9, 18, 36 et 72 molécules H_2O à l'intérieur de la supercellule SiO_2 pour obtenir quatre rapports eau-silice différents et comparer les changements dans le comportement thermodynamique ainsi que les effets potentiels sur les propriétés structurelles et de transport élémentaire. Nous étudions les quatre systèmes à des températures de 2000, 3000, 4000 et

5000 K et des densités allant de 0,34 à 2,77 g/cm^3 selon le système. Nous calculons le point critique de SiO_2 entre 5000 et 5500 K, de 0,6 à 0,85 g/cm^3 et de 0,15 à 0,25 GPa. La présence d'eau a un effet direct sur le placement du point critique, le réduisant à plus de 2 000 K dans des conditions spécifiques. Nos résultats montrent que les matériaux à l'état supercritique sont souvent sous-estimés dans les modèles hydrodynamiques de formation de lune, ce qui peut avoir un impact sur le mélange élémentaire dans le résultat de l'impact géant.

To my mother.
May her laughter echo forever.

Acknowledgements

A thesis is the result of the collective work of many people. I'm grateful to the École Normale Supérieure de Lyon, the Centre National de la Recherche Scientifique and the European Research Council for the opportunity of doing this PhD. I would also like to extend my appreciation to the École Doctorale de Physique et Astrophysique, represented by Dany Davesne and Sylvie Flores, for taking such good care of students. I'm specially thankful to the people of Université Claude Bernard Lyon 1, Thierry Alboussière, Eric Debayle, Isabelle Daniel, Emanuela Mattioli and Yannick Ricard, for welcoming me during the pandemic and for all the support they continued to give me to this day.

A big shout-out to my friends and colleagues for the great moments and discussions together. Laëtitia, Anaïs, Gabriel, Alistair, Anastasis, Elham, Ali, Tim, Zhi, Mandy, Sam, Misha, the encouragements and laughter made this journey easier.

I would also like to thank my family, which stood by my side in every step showing nothing but love. And, finally, I would like to show my deepest gratitude to my greatest supporter and the reason I made it this far: my mother, Valéria Brandelli.

Contents

Chapter 1

Introduction

Contents

1.1 Solar System Overview

The Solar System is largely formed by hydrogen and helium, where all the other elements represent only 2% of the total elemental abundances. The solar mass represents nearly 99% of the total mass and represents the mean composition of the Solar System (Lodders, 2020). The remaining ∼1% of the mass is distributed in the form of planets, satellites, asteroids, comets and other diverse bodies. The diversity of objects in the Solar System seems in contrast with its actual composition, especially considering that they are assumed to originate from the same initial composition (Taylor and McLennan, 2009). However, a different theory based on titanium isotopes suggests that thermal processing in the disk before the period of accretion lead to condensation from a non-solar composition (Trinquier et al., 2009). Nonetheless, the differences in size, structure and composition observed throughout the Solar System are a result of formation and evolutionary processes in the protoplanetary disk.

The understanding of processes involved during the formation of planetary bodies and their satellites are still cause of debate. In the protoplanetary disk, radial variations in physico-chemical conditions affected the stability of the elements and altered the composition of the disk with increasing solar distance (Russell et al., 2006, and references therein), as shown in

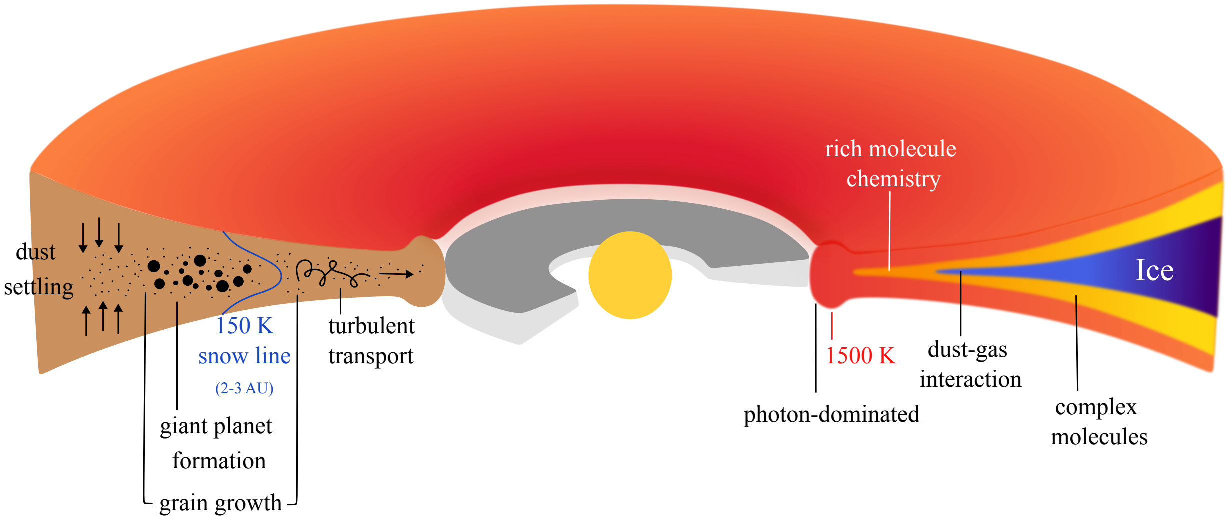

Figure 1.1: Schematic structure of a protoplanetary disk around a Sun-like star with a 1-5 Myr. Figure adapted from Henning and Semenov (2013).

Figure 1.1. Far from the radiation and high temperatures of the Sun, the outer part of the disk had cryogenic temperatures. Temperature estimates for this region can vary from 50 to 150 K (Boss, 1998). In these conditions, volatile elements condensed and resulted in the formation of icy planets and moons (Chambers, 2003). However, closer to the Sun, the inner part of the disk had higher temperatures, reportedly varying from 500 to 1500 K (Boss, 1998), where evidence suggests silicates to be partially vaporized (Chambers, 2003; Messenger et al., 2006). In this region, the protoplanetary disk was rich in silicate material and refractory elements, originating essentially rocky bodies.

Accretion in the inner part of the disk happened in several steps. The direct condensation of micrometer sized grains from the gas, together with the later processing of these grains, lead to the formation of the oldest solids known, such as calcium-aluminum inclusions (CAIs), ameboid-olivine aggregates (AOA) and chondrules (Russell et al., 2006), which are all present in carbonaceous chondrites. Condensation and evaporation were dominant processes in the first stages of accretion and happened much more rapid than in later stages, where larger bodies and planetesimals were already formed. Planetary embryos underwent a period of stochastic events of accumulation, often involving giant impacts. At the same time, these bodies were subject to secondary processes in the form of aqueous alteration and thermal metamorphism, which involved transformation of the mineralogical phases already present. Furthermore, they also underwent a certain degree of melting and differentiation, resulting in the formation of cores and layered structures.

Models of accretion still struggle to yield an accurate description of the current structure of the Solar System and also depend on types of collisions considered as a mechanism in place during this period (Chambers, 2013). Nevertheless, it is currently understood that planets, asteroids and the more than 200 satellites formed as a result of surrounding conditions regarding their positioning in the protoplanetary disk and the posterior processes that took place. The unique combination of such processes resulted not only in different sizes and structures, but, most importantly, in different chemical signatures for every single parent body in the Solar System. The study of the imprinted signatures shed light into the evolution of planetary bodies and relied strongly on materials available for in situ analysis, which for many years were made essentially by meteorites, micrometeorites and interplanetary dust particles (Grady and Wright, 2006).

With the beginning of the Space Age in 1957 and subsequent space missions up to the present-day, samples could be directly gathered from the parent body and returned to Earth. The Apollo program was responsible for returning more than 300 kg of lunar material and lead to remarkable discoveries on the isotopic signature of the Moon and to breakthroughs regarding the Earth-Moon system. The analysis of lunar oxygen isotopic composition revealed to be surprisingly nearly identical to that of the Earth, calling for new models of formation of the Earth-Moon system that could explain such similarity (O'Neil and Adami, 1970; Clayton et al., 1973). Questions on the nature of the processes involved during the formation of the Moon remain unclear to this day.

1.2 The Earth-Moon system

Inner planets and satellites of the Solar System are largely composed of silicate materials, where SiO_2 is the major building block. The silicate portion often envelopes a metallic core made essentially of Fe-Ni alloy (Li and Fei, 2014). The formation of the core is a result of the silicate-metal fractionation during the period of accretion, when the energy imparted by impacts and decay of radioactive elements resulted in high temperatures that facilitated the formation of magma oceans (Elkins-Tanton, 2012; Day and Moynier, 2014). At these conditions, denser materials displace towards the nucleus and lighter materials ascent towards the surface, resulting in a fully differentiate body. It is also at this stage that large-scale degassing can happen, leading to significant loss of volatile elements (Elkins-Tanton, 2012). The silicate fraction can be separated into a deeper portion, called mantle, and a more superficial part, called crust. Because of the increasing pressure, minerals in the mantle tend to present a tighter packing than those found in the crust. Furthermore, the crust is exposed to superficial secondary processes, such as cratering and, in systems that have an atmosphere, these processes can also include alteration by weathering (Taylor and McLennan, 2009).

The Earth and the Moon are differentiated bodies with crust, mantle and core. The primitive silicate composition of the Earth was established by McDonough and Sun (1995) and is referred to as the Bulk Silicate Earth (BSE). This estimate defines the composition of the silicate portion before mantle-crust differentiation and after core formation (Palme and O'Neill, 2014). Formed shortly after accretion, Earth's core has more than 3000 km of radius and represents roughly 16% of the total volume (Li and Fei, 2014), as represented in Figure 1.2a. With respect to solar abundances, the Earth is depleted in moderate volatile and volatile elements (Halliday, 2014). A diagram describing the variation on terrestrial elemental concentrations with respect to carbonaceous chondrites composition values in Anders and Grevesse (1989) is shown in Figure 1.3.

Lunar composition is less accessible in comparison to the Earth and it depends on lunar samples and seismic data. Seismic velocity measurements show that the lunar core is signifi-

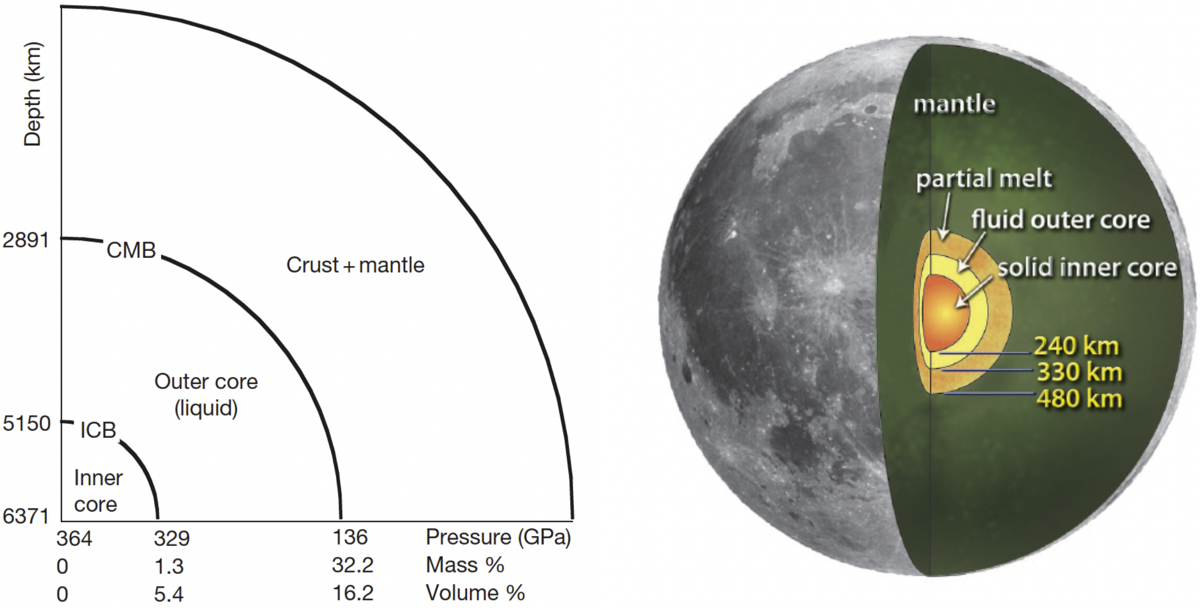

(a) (b)

Figure 1.2: The Earth and the Moon schematic representation. Please note that the thickness of terrestrial inner layers is shown in depth with respect to the surface, whereas the lunar inner structure is indicated as radius from the center. a) Representation of the internal structure of the Earth. On the left side, values of depth are shown for the core-mantle boundary (CMB) at 2891 km, for inner core-outer core boundary (ICB) at 5150 km and for Earth's total radius (6371 km). Respective pressure, mass and volume values are also shown for each boundaries. Figure from Li and Fei (2014). b) Estimate internal structure of the Moon. The solid inner core is represented in orange with radius of 240 km, predicted fluid outer core is indicated in yellow with a radius of 330 km, partial melt enveloping the core is in dark yellow with a radius of 480 km, mantle is indicated in green and crust in grey. Figure adapted from Weber et al. (2011).

cantly smaller than the terrestrial core (Weber et al., 2011) and represents about 2 to 3% of its volume (Taylor and McLennan, 2009), as shown is Figure 1.2b. Such evidence when associated with the mean density estimate for the Earth (5.54 g/cm^3) and the Moon (3.55 g/cm^3), indicate a depletion on lunar contents of iron with respect to that of the Earth (Taylor and McLennan, 2009). Furthermore, the Moon also shows depletion in moderate volatile and volatile elements when compared to terrestrial values (Lock et al., 2018, and references therein). Conversely, measurements of refractory elements on lunar samples show higher contents than in the BSE. A compilation of bulk silicate Moon compositional values can be found in (Melosh, 2014). Nevertheless, the satellite-to-parent mass ratio of the Earth-Moon system is the largest observed in the Solar System (Taylor and McLennan, 2009). The only other system where orbiting satellite and parent body show a larger ratio is Pluto-Charon.

The uniqueness of the Moon does not come solely from being the only satellite orbiting the Earth. Besides the compositional differences observed, the Earth and the Moon share unique aspects that are not generally observed elsewhere in the Solar System. The roughly identical isotopic composition on many stable isotopes is a key feature that constraint models of lunar formation and need to be addressed when modeling different scenarios.

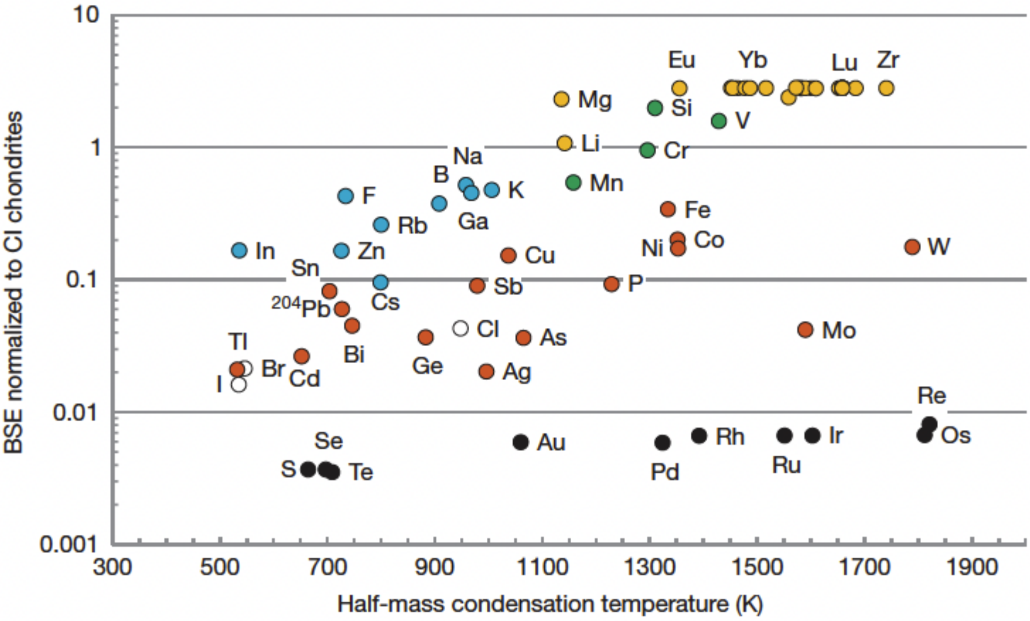

Figure 1.3: Bulk Silicate Earth composition normalized to CI chondrites as a function of the half-mass condensation temperature in K. Colors represent different geochemical behaviors. Black circles are highly siderophile and chalcophile elements; open circles are halogens; red circles are moderately siderophile elements; green circles are slightly siderophile elements; yellow circles are litophile elements; blue circles are volatile litophile elements. Figure from Halliday (2014).

1.2.1 Isotopic composition

First in situ measurements of oxygen isotopes in lunar samples revealed a virtually identical composition with respect to terrestrial values (O'Neil and Adami, 1970; Clayton et al., 1973) and similar values continue to be reported by following authors (Clayton and Mayeda, 1975; Wiechert et al., 2001; Hallis et al., 2010). A discrete deviation in Δ^{17}O values has been described in the literature, where authors argue that this divergence can originate from a contribution from late veneer impactors (Greenwood et al., 2018). Other authors argue that Δ^{17}O variations can be a result of condensation of SiO_2 in the presence of hydrogen from a silicate atmosphere in the aftermath of a giant impact (Cano et al., 2020). However, this deviation is not in agreement with values previously reported in the literature (Wiechert et al., 2001). A comprehensible review on the oxygen isotopic composition of Solar System bodies has been published by Ireland et al. (2020), showing the contrasting isotopic signatures on analytically accessible bodies, such as meteorites, asteroids, satellites and planets.

Further analysis on lunar samples showed persistent identical values not only for oxygen isotopes, but on a range of stable nuclides, such as titanium (Zhang et al., 2012), silicon (Armytage et al., 2012) and chromium (Mougel et al., 2018). As reported on titanium and chromium measurements, the exposure to cosmic rays generates secondary effects that can modify the isotopic composition and, thus, corrections on such effects can broaden the range of near identical values for the Earth-Moon isotopic composition. However, the similarity in the isotopic signature is not observed for some of the short-lived nuclides that are sensitive to differentiation and planetary formation processes, such as the ^{182}Hf-^{182}W system (Kruijer and Kleine, 2017;

Jacobsen and Harper Jr., 1996; Jacobsen, 2005). Terrestrial mantellic heterogeneities have been observed in tungsten isotopes (Touboul et al., 2012) and new measurements on lunar vanadium isotopes indicate a chondritic component compared to the bulk silicate Earth (Nielsen et al., 2021).

The isotopic similarities in the Earth-Moon composition require a model with a common origin for both bodies. Mechanisms that have been described in order to explain such observations consider either the inheritance of nuclides from an identical isotopic reservoir in the protoplanetary disk, or the mixing and equilibration as a result of a giant impact (Pahlevan and Stevenson, 2007; Canup, 2012; Cuk and Stewart, 2012; Lock et al., 2018). Given the heterogeneity of the protoplanetary disk in terms of chemical distributions, the simultaneous accretion from an identical reservoir is unlikely. Therefore, models that consider the formation of the Earth-Moon system from a giant impact remain the best hypothesis to this day to explain the identical isotopic signatures.

1.2.2 Water

Regardless of the similarity in isotopic compositions, Moon and Earth differ considerably concerning the abundance of volatile species. Their contents can differ concerning sodium, potassium and others (Melosh, 2014, and references therein). Being the basis of life as we know, H_2O is arguably the most relevant volatile specie to be consider. The presence of water affects properties of materials, such as viscosity and melting, but also can give evidence on the origin and formation of planetary bodies (Day and Moynier, 2014). Water is ubiquitous on Earth and measurements of oxygen isotopes on zircon crystals suggest the presence of a terrestrial water ocean as early as 4.4 Gyr (Wilde et al., 2001; Valley et al., 2002). The origin of the water on Earth is still not entirely understood. However, studies show that more than 70% of water present today was accreted prior to the Moon forming impact and up to 30% from later chondritic contribution during the late veneer (Greenwood et al., 2018). With the lack of visible liquid water or ice caps, the Moon was thought to be completely anhydrous for many years (Taylor et al., 1995). The improvement in instrumental accuracy made possible to detect H_2O contents on lunar rocks, revealing a more hydrated Moon than previously thought (Hauri et al., 2015). Depending on the lithological type, lunar H_2O can vary from 3 to 292 ppm (Canup et al., 2021).

In general, volatile loss can be a result of degassing during volcanic eruptions or during a magma ocean stage. Saal et al. (2008) analyzed lunar glass beads in sample cross section, where results showed an increasing depletion in H_2O contents and further volatiles species from the center towards the rims, indicating significant degassing during volcanic eruptions. Furthermore, the authors also argue that a deep layer of ilmenite may hold volatiles during the crystallization of the lunar magma ocean (LMO) and prevent a complete volatile loss. Conversely, Day and Moynier (2014) argue that volcanic degassing is not sufficient to explain the water contents and that the volatile depletion can only be explained by degassing during the lunar magma ocean. Nevertheless, water contents can be expected to increase towards the end of crystallization of magma oceans (Figure 1.4; Elkins-Tanton, 2011), meaning also an increase of its effects on the residual melt. The inclusion of water in models of lunar formation is important in order to provide a better understanding of the processes involved (Saal et al.,

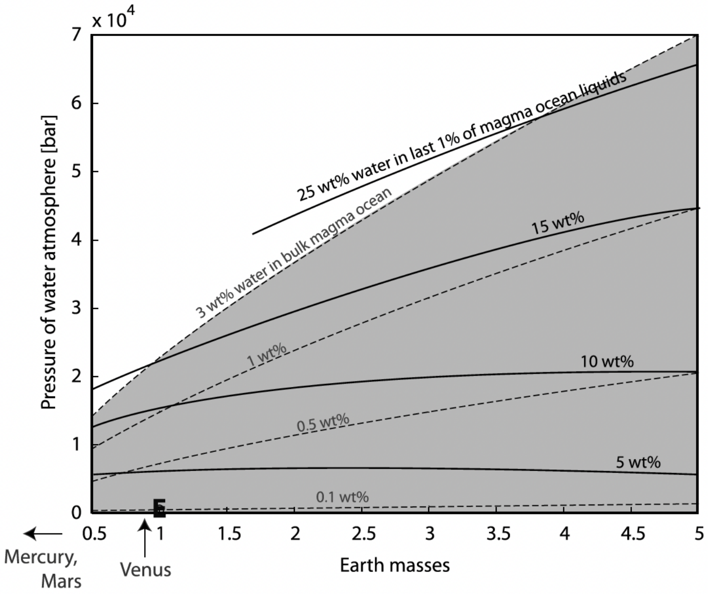

Figure 1.4: Pressure of water atmosphere as a funcition of planet mass and initial water content produced by degassing of magma ocean. Dashed lines represent initial bulk water contents in the magma ocean. Bold lines represent the water content in the final 1 vol% liquid in magma ocean, close to full crystallization of the planet. Shaded area represents the range of water content in achondritic meteorites. Figure from Elkins-Tanton (2011).

2008).

1.3 Lunar formation models

Before Apollo missions, the Moon was said to be cold and primitive. As a general rule, satellites can accrete from an early debris disk, but they can also be captured objects. Early models of lunar formation proposed before Apollo missions were fission (Darwin, 1879), capture (Urey, 1966) and coaccretion (Schmidt, 1959). In the fission model, a rapidly spinning Earth would become so elongated that would eventually rupture, giving origin to the Moon from the separated fragment. However, it fails to explain the origin of such high angular momentum and what would be the processes involved to dissipate it afterwards. The model proposed by Urey (1966), considers that the Moon accreted in a different region of the protoplanetary disk and was later captured into the terrestrial orbit. The capture theory had difficulties conciliating the velocities involved and the mechanisms of capture. With the isotopic measurements in the following years, this theory was discarded. The leading most accepted theory was croaccretion (Schmidt, 1959; Wood, 1986), where the Moon and the Earth were believed to have accreted from the same protoplanetary disk region. Even though this model would agree with posterior isotopic observations, it failed to explain the differences in bulk compositional values, angular momentum and evidences of existence of a magma ocean (Wood, 1986). Apollo's returned samples shed light into the composition of the Moon and showed a differentiated body with igneous activity. Since the first oxygen isotopic measurements made on lunar returned samples, considerable progress was made to address the questions relative to the formation of the Moon. It became clear that the Moon and the Earth must had shared a common origin. Seismic data and further analytical measurements, continue to reveal characteristics that need to be considered and explained by any lunar formation model. Large impacts were already believed to be a mechanism of accretion occurring throughout the Solar System and were also responsible for melting processes after the extinction of ^{26}Al (Elkins-Tanton, 2012). To this day, the theory that seems to better address the singular aspects of the Earth-Moon system is the Giant Impact Theory.

1.3.1 Giant Impact Theories

In the Giant Impact Theory, the Moon was formed by accretion from a dust and gas disk formed in the aftermath of a large collision between the proto-Earth and an impactor. This theory was first proposed by Hartmann and Davis (1975), followed by Cameron and Ward (1976) and has continued to evolve ever since. Different scenarios mostly based on smoothed particles hydrodynamic simulations have been invoked over the years (e.g. Hartmann and Davis, 1975; Canup, 2012; Cuk and Stewart, 2012; Reufer et al., 2012; Rufu et al., 2017; Lock et al., 2018), challenged to explain the Moon's large mass, orbit inclination, isotopic composition, volatile budget and iron depletion within a single solution. They consider different initial settings which affect possible final elemental distributions in the protolunar disk. Many reviews on the Moon formation problematic have been published recently (Asphaug, 2014; Barr, 2016; Lock et al., 2020; Canup et al., 2021) with an accurate description of the solutions presented and also the potential inadequacies of each model. Here, we are going to describe briefly two current models of impact found in the literature: the canonical impact (Canup, 2012) and the fast-spinning Earth model (Cuk and Stewart, 2012; Lock et al., 2018).

1.3.1.1 Canonical Impact model

The canonical impact model generally considers a low-velocity oblique collision by a large impactor (Canup, 2014). It has been described extensively in the literature with varying initial simulation settings (Canup and Asphaug, 2001; Canup, 2004; Salmon and Canup, 2012; Canup, 2012). The model proposed by Canup (2012) starts from the collision between two differentiated bodies and consider a much larger impactor than previous studies, where the mass of the impactor is similar to the target's mass. The scenarios with most fitting results consider an impactor-to-total mass ratio between 0.4 and 0.5, where the impactor contributes in similar proportions to the disk and to the target. The collision creates a disk with 50 to 90% of its mass in the vapor phase where the material comes mostly from the impactor's mantle. The composition of the disk is homogeneous and depleted in iron. The impactor composition was taken to be similar to Mars and results showed that the final silicate composition diverges less than 1%. Temperatures in this model can vary roughly from 2000 K to more than 6400 K in an 80,000 km across disk. The total simulated time was 1 day and, once particles are in the disk, they can accumulate at a distance of 3.8 Earth's radius to form the Moon. In a concomitant work, the period necessary for the complete accretion of the Moon from the disk was estimated in about 100 years (Salmon and Canup, 2012). Oxygen represents the biggest constraint in previous canonical impact models, since most disk material originates from the impactor (Canup et al., 2021). However, the large mass proposed in the work of Canup (2012) allows the homogenization of the composition before accretion. Nevertheless, the model still struggles to resolve the excess in the angular momentum and also applies a model with simple composition, where it only considers iron for the core particle and a dunite mantle. Furthermore, recent studies indicate that the probability to conciliate the homogeneity observed in different isotopic systems as an outcome of the standard giant impact scenario (i.e. the canonical model) is of less than 0.5% (Fischer et al., 2021).

1.3.1.2 Fast-spinning Earth impact model

The fast-spinning Earth model of lunar formation considers a high energy collision between a small impactor and a fast-spinning proto-Earth. In the model proposed by Cuk and Stewart (2012), the average terrestrial period of rotation is 2.5h at the moment of impact, where posterior orbital resonance between the Sun and the Moon would reduce the angular momentum. In this model, most of disk material comes from the target. The high energy of the impact vaporizes silicates and forms a silica atmosphere and vapor rich disk. Although the mixing could resolve isotopic signatures of the Earth-Moon system, modeling of the chemical evolution is necessary to further investigate final compositions. The density profile of the debris disk varies from 20 g/cm^3 in the center to 0.01 g/cm^3 within the Roche limit and towards 10^{-4} g/cm^3 in the outermost parts. Lock and Stewart (2017) proposed that an impact in a fast-spinning body would produce a new planetary object, which was named synestia. Lock et al. (2018) describe a Moon forming impact with the formation of a synestia, where moonlets form from condensation and equilibration with a BSE atmosphere in low pressure regions outside the Roche limit, where equilibration temperatures would be close to 4000 K. This model projects enough mass in the disk to account for the large lunar mass with mixing of impactor and target material. The authors consider that partitioning of volatiles in the vapor would explain the observed lunar budget, but the model is not consistent with current estimates of water contents (Saal et al., 2008) in the Moon.

1.4 Equations of state and phase diagrams

Equations of state (EOS) summarize the thermodynamic properties of a given material, usually expressed as a functional relation connecting the parameters that describe the material in the form of P(p,T) (Melosh, 2007). They are an essential input in current smoothed-particle hydrodynamics (SPH) impact simulations because they predict pressure-temperature-velocity variations, ultimately governing the final outcome of any scenario. For instance, the distribution of the mass in the disk is affected not only by the choice of material, but also by the equation of state the describe the material (Benz et al., 1989), showing ultimately an influence in mass injection, elemental distribution and multiphase partitioning.

The EOS initially used in SPH simulations was the one developed by Tillotson (1962). Observations on problematic representation of the thermodynamic behavior of multiphase states showed a significant misrepresentation of the effects of pressure gradients in the gas (Benz et al., 1989), favoring the utilization of a different equation of state, called ANEOS. ANEOS was developed by Thompson and Lauson (1974) and it was based on analytical approximations for application in metallic systems. It gave a better representation of mixed phases, but it treated the gas as only monoatomic particles. This assumption lead to a high-energy standard for vaporization, underestimating of post-impact gas formation. Melosh (2000) corrected the previous assumption that the gas is monoatomic with a new formulation of the ANEOS, allowing the presence of clusters and, therefore, leading to a higher gas proportion in final simulations. In a comparison between the original and the modified version, the author demonstrated an increase of a factor of 3 in the amount of vapor that could be generated from impact (Melosh, 2007). However, the description of the gas only accommodates diatomic molecules, which can be problematic for materials presenting a gas phase largely dominated by molecules with more than two atoms, such as water. Furthermore, the improvement in ANEOS made by Melosh (2000) was also reported to impact the amount of the total mass in the disk and to increase its contents of iron (Canup, 2004).

1.5 Goal of the thesis

Models of lunar formation rely strongly in equations of state that describe the behavior of materials. The main goal of this work is to provide accurate information concerning key materials involved in the formation of the Moon at conditions relevant to current models available. To do so, we specifically focus on the behavior of silica and silica-water systems at low-density and high-temperature regimes.

SiO_2 is one of the major building blocks of the Earth-Moon system and plays a central role in lunar formation processes. We aim to describe SiO_2 behavior in better detail focusing on the construction of a reliable phase diagram in the liquid-vapor region and in establishing an accurate critical point. Subsequently, we focus on the study of structural and transport properties under varying conditions, comparing the behavior of the main elements at every step. Furthermore, we aim to assess the influence of the presence of water in the silicate system, in terms of positioning of the critical point and variation of phases, where we also focus on the potential effects on structural and transport properties of individual particles. To do so, we construct four hydrated systems and then compare the variations with the anhydrous SiO_2 baseline.

Chapter 2

Methodology

Contents

2.1 Multiscale modeling

For many years, the grounds for understanding the behavior of a particular system was mostly given by theoretical formulation and experimentation. In order to accurately describe the implications of certain conditions to a material, theory and empirical knowledge were always confronted with each other. With the exponential increase in computing power and numerical methods, modeling became an essential tool to predict behaviors of systems or to design and test potentially interesting new materials. Moreover, it can often complement experimental work by allowing modeling at extreme conditions. Particularly, planet forming scenarios often involve extremely high temperatures and low densities, conditions generally difficult to reach and that generate limited data points in most current experimental setups.

In the past few decades, it became possible to bridge between scales and describe larger systems from finer scales with the introduction of multiscale modeling. As shown schematically in Figure 2.1, with this technique, a system of interest can be modeled by combining methods of different complexities, given that the physics at finer scale is better understood than that at coarser scale (Fish et al., 2021). For instance, macroscale description of plastic and elastic behavior of a given material can be coupled with modeling of microscale dislocations in order to provide information concerning discrete phenomena that needs understanding in better detail, such as chemical reactions or local defects (Weinan, 2011). By applying multiscale modeling, is also possible to combine models that provide information essentially regarding displacement of particles in space, such as molecular dynamics, with subatomic models that describe the behavior of the electrons, i.e. ab initio methods. The choice of the method depends on the aimed resolution and it must balance accuracy and complexity, since finer-scale calculations can rapidly become too complex to handle even by modern supercomputers.

Ab initio methods describe subatomic scales of a given material from a quantum mechanics view point. It consider electrons and nuclei as the basic particles and depend essentially on the physics of the atomic species present in the system to be simulated (Lee, 2017). The combination of ab initio methods with molecular dynamics approaches allows the description of the trajectory of the particles while calculating force and energy from first principles. It provides accurate thermodynamic information and also allows the analysis of electronic and magnetic properties. Density functional theory (DFT) is among the most popular approaches of ab initio calculations (van Mourik et al., 2014) with the goal to solve Schrödinger equation by recasting the problem and maintaining accuracy. Coupled with molecular dynamics methods (MD), it is a powerful tool to derive equations of state and estimate phase diagrams under various conditions (Söderlind and Young, 2018). The DFT-MD approach will be detailed in the next section. Further reading concerning multiscale modeling and current available methods can be found in Frenkel and Smit (2002), Fish (2014), Fish et al. (2021) and references therein.

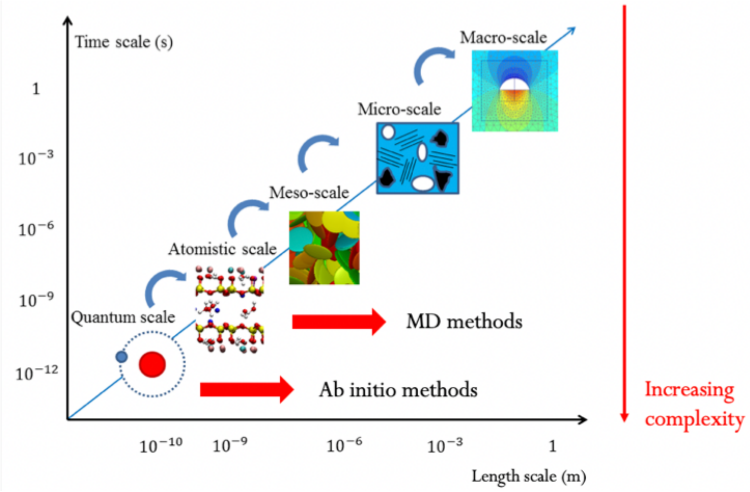

Figure 2.1: Multiscale modeling scheme on a time-length diagram. Ab initio methods are given in quantum scale, described from physical laws. At a coarser scale, molecular dynamics (MD) methods apply hard-sphere models at larger time scales. Modelisation complexity increases towards finer scales. Figure modified from *Andrew J. Whittle's Research Group at MIT, Multiscale modeling of clay-water systems* (accessed: June 16th 2022, *https://ajw-group.mit.edu/multiscale-modeling-clays*).

2.2 Ab initio molecular dynamics simulations

Until the mid-80s, available molecular dynamics methods relied on empirical interatomic potentials which did not allow access to any information regarding the electronic structure. The first combined approach of molecular dynamics with density functional theory was proposed by Car and Parrinello (1985), where the electronic wavefunctions are introduced as dynamic variables and the update of the electronic structure is calculated on-the-fly with ionic motion (Boero and Oshiyama, 2015). By coupling these techniques, it was possible for the first time to compute ground-state electronic properties of larger systems from first principles while having the ionic motions given by classical mechanics. In modern DFT, the Born-Oppenheimer approximation was introduced, where the motion of nuclei and electrons are decoupled and the ground-state energy is calculated at every timestep. In a nutshell, ab initio molecular dynamics (AIMD) aims to describe accurately dynamic systems from a quantum mechanics perspective by solving Schrödinger equation. The means to realistically do so requires a series of approximations that can be computationally demanding (Table 2.1).

Table 2.1: System size scaling of various methods and their maximum number of atoms. Table from Lee (2017).

Methods	Scaling	N_{max} (atoms)
Schrödinger	$O(e^N)$	1
Hartree-Fock	$O(N^4)$	~50
DFT	$O(N)$-$O(N^3)$	~200
MD	$O(N)$	$10^{(7\text{-}11)}$

2.2.1 Schrödinger equation

In quantum mechanics, the Schrödinger equation describes the time evolution of particles for a given quantum state of a system. For a one-dimensional space, the time-dependent equation can be described as:

$$i\hbar \frac{\partial}{\partial t}\psi = \hat{H}\psi \tag{2.1}$$

where the wavefunction ψ contains all the system properties for every particle in n-dimensional space at a given time t. In a system that do not change with time, the Schrödinger time-independent equation can be generally written as:

$$E\psi = \hat{H}\psi \tag{2.2}$$

where E is the energy and $\hat{H}$ is the Hamilton operator. The Hamiltonian $\hat{H}$ can be expressed as:

$$\hat{H} = \hat{T}_e + \hat{T}_n + \hat{V}_{en} + \hat{V}_{nn} + \hat{V}_{ee} \tag{2.3}$$

where $\hat{T}_e$ and $\hat{T}_n$ are the kinetic energy operator for the electrons and nuclei, respectively, and $\hat{V}_{en}$, $\hat{V}_{nn}$ and $\hat{V}_{ee}$ are the potential energy operators accounting for nucleus-electron, nucleus-nucleus and electron-electron given via the Coulomb potential. Due to its high dimensionality with 3N coordinates for N particles, the complexity of this equation allows it only to be solved for atoms with small number of particles, such as hydrogen and helium. Solving Schrödinger equation for complex systems requires a number of approximations in order to address the many-particle problem. Reformulations implemented in the DFT method applied in the calculations of this work are going to be briefly described in the following sections.

2.2.2 Born-Oppenheimer approximation

In the approach proposed by Born and Oppenheimer (1927), the motion of nuclei and electrons is separated from each other based on the assumption that their large difference in mass results in a difference in motion rates, with the light electrons adjusting to the dynamic of the heavier nuclei. Considering nuclei as fixed in space, the electronic wavefunction, then, depends parametrically on the position of the nucleus and remain at their instantaneous ground-state, providing a potential energy surface in which the nucleus would move. By decoupling the movement of the particles, nuclear and electronic wavefunctions can be expressed as a product and treated separately, where the electronic Hamiltonian is then expressed as:

$$\hat{H}_e = \hat{T}_e + \hat{V}_{en} + \hat{V}_{ee} \tag{2.4}$$

The Born-Oppenheimer approximation helped to develop electronic methods that do not explicitly depend on nuclear motion. With its implementation in ab initio molecular dynamics methods, the energy is minimized and forces are calculated at each DFT cycle, with minor restrictions concerning the length of the timestep (Kühne, 2014).

2.2.3 Density Functional Theory

Density functional theory (DFT) is the result of the work from Hohenberg, Kohn and Sham on a series of theorem and equations in the 1960s. Hohenberg and Kohn (1964) determined in a two-folded theorem that the ground-state energy is a functional of the electronic density, ultimately replacing the wavefunction by the electron density n($\mathbf{r}$). Kohn and Sham (1965) mapped the many-body interacting problem on an non-interacting manner, where the unknown terms are placed in the exchange-correlation functional and the minimizing density is established in terms of single-particle orbitals. DFT became more predictive in the with the development of more appropriate forms of the exchange-correlation functionals that increase the accuracy of the method. The theorems will be presented briefly herein.

2.2.3.1 Hohenberg and Kohn theorem

Inspired by the precedent Thomas-Fermi theory (Fermi, 1927; Thomas, 1927; Kohn, 1999) that introduced the main idea of electron density n($\mathbf{r}$), Hohenberg and Kohn (1964) applied the concept to the treatment of the many-body electron problem. In general terms, the two-folded theorem demonstrate that the energy is a functional of the electron density and, therefore, all ground-state observables depend only on the electron density. The relation that expresses the ground-state energy functional $E_{HK}[n]$ can be written as:

$$E_{HK}[n] = F_{HK}[n] + \langle \hat{V}_{ext} \rangle \tag{2.5}$$

where $\langle \hat{V}_{ext} \rangle$ is the external potential. The free energy $F_{HK}[n]$ is a functional dependent on the kinetic $\hat{T}$ and potential electron-electron interaction $\hat{V_{ee}}$ operators, which can be express as:

$$F_{HK}[n] = \langle \hat{T} \rangle + \langle \hat{V_{ee}} \rangle \tag{2.6}$$

The ground-state density is given by energy minimization through a variational approach with trial wavefunctions. In this approximation, the solution depends only on the electronic positions as a function of 3 dimensional coordinates and independently of N.

2.2.3.2 Kohn-Sham equations and exchange-correlation functional

The Kohn-Sham approach (Kohn and Sham, 1965) mapped the interacting particle problem on a non-interacting manner, where the minimization of the energy is not given with respect to the many-body wavefunction, but in terms of single-particle orbitals (Marx, 2006). The free energy contains only terms that can be calculated exactly where the remaining unknown quantities are incorporated in the exchange-correlation term. The energy can then be expressed as:

$$E_{KS}[n] = T_{ip}[n] + \langle \hat{V}_{ext} \rangle + E_H[n] + E_{xc}[n] \tag{2.7}$$

where T_{ip} is the kinetic energy of independent particles and E_H is the Hartree potential energy. The exchange-correlation energy is the relation between the known quantities with the approximated terms, given by:

$$E_{xc}[n] = \langle \hat{T} \rangle - T_{ip}[n] + \langle \hat{V_{ee}} \rangle - E_H[n] \tag{2.8}$$

where $\langle \hat{T} \rangle$ is the exact kinetic energy and $\langle \hat{V_{ee}} \rangle$ is the exact interaction energy term. The one-particle Schrodinger equation can be written as:

$$\left(-\frac{\hbar^2}{2m} + v_{eff}(\boldsymbol{r}) \right) \phi_i(\boldsymbol{r}) = \epsilon_i \phi_i(\boldsymbol{r}) \tag{2.9}$$

where $\hbar$ is Planck's reduced constant, m is mass and the electron density, eigenvectors ϕ_i and eigenvalues ϵ_i are given by:

$$n(\boldsymbol{r}) = \sum_{n=1}^{\infty} f_i |\phi_i(\boldsymbol{r})|^2 \tag{2.10}$$

where f_i is the integer occupation number of the i_{th} ϕ_i orbital. The minimum energy for a fixed number of particles yields the effective potential v_{eff} (Martin et al., 2016), as in:

$$v_{eff}(\boldsymbol{r}) = v_{ext}(\boldsymbol{r}) + \frac{\delta E_H[n]}{\delta n(\boldsymbol{r})} + \frac{\delta E_{xc}[n]}{\delta n(\boldsymbol{r})} \tag{2.11}$$

These three equations (2.9 - 2.11) enter a self-consistent cycle in order to be solved since the effective potential that yields the orbitals which determine the density is also a functional of the density. Furthermore, the quality of the approximation used for the exchange-correlation energy term sets the quality of the electronic structure calculation (Iftimie et al., 2005). The local-density approximation (LDA) was introduced in the original KS work (Martin et al., 2016). Generalized-gradient approximation (GGA) was introduced later on and improved accuracy in structure and bonding estimations in comparison with LDA (Martin et al., 2016). Different exchange-correlation functionals have been introduced over the years and extensive research has been done comparing the effects of the functionals over properties of materials (Fritsch and Schorr, 2020). Further explanation of the Kohn-Sham approximation can be found in Martin et al. (2016) and Woods et al. (2019).

2.2.4 Molecular dynamics

The molecular dynamics method allows the computation of equilibrium and transport properties of a many-body system using classical mechanics solving Newton's law of motion (Frenkel and Smit, 2002). In this method, atoms are treated as hard spheres with established initial positions and move by the integration of net forces over incremental timesteps that can vary roughly from femtoseconds (fs) to picoseconds (ps). In classical MD, the forces acting on atoms are calculated from interatomic potentials, whereas, coupled with DFT, forces are calculated from first principles, as explained previously in section 2.2.3.

In a MD cycle, every atom starts from unique initial positions and velocities. The interatomic forces acting on each atom are calculated based on the method of choice and the net value is then computed. From the net forces, the velocities are estimated from Newton's law of motion, based on the assumption that they are constant over short time increments. The velocities are ccontrolled with the help of a thermostat in order to assure the energy of the system remain stable. Once the new forces and velocities are established, the positions of the atoms are updated through integration algorithms (e.g. Verlet or Leap-Frog). The MD cycle restarts systematically until an appropriate preestablished number of iterations is achieved, where equilibrium is reached and the macroscopic properties can be calculated. Thermostat, integration algorithms and timestep balance the accuracy of the method, where a comprise with the speed of calculations should be made.

The constraints imposed to the collection of iterations from the MD cycle represents the statistical ensemble on which the simulation is performed (Mazurek et al., 2021). These constraints can be chosen based on the properties of interest and typically concern energy (E), pressure (P), temperature (T) and number of particles (N). For instance, the canonical ensemble fixes the number of particles, the volume and the temperature and is, therefore, abbreviated as NVT. In such ensemble, the temperature is regulated with a thermostat, where it is allowed to oscillate around the nominal value. Examples of different possible ensembles are also the microcanonical (NVE) and the isobaric-isothermic (NPT). Further explanation can be found in Frenkel and Smit (2002), Rapaport (2004), Lee (2017) and references therein.

In this work, we employ the DFT-MD method as implemented in the Vienna Ab initio Simulation Package (VASP®; Kresse and Furthmüller, 1996), which is schematically represented in Figure 2.2. The simulation cycle starts from the initial position of the ions, where the electron density is initially guessed and the free energy is calculated based on the single-particle orbital approximations derived by Kohn-Sham. The DFT loop is repeated until the energy is minimized to be then plugged-in into Newton's equation of motion for the nuclei, where the positions are updated. The properties of the system are computed at the end of each cycle.

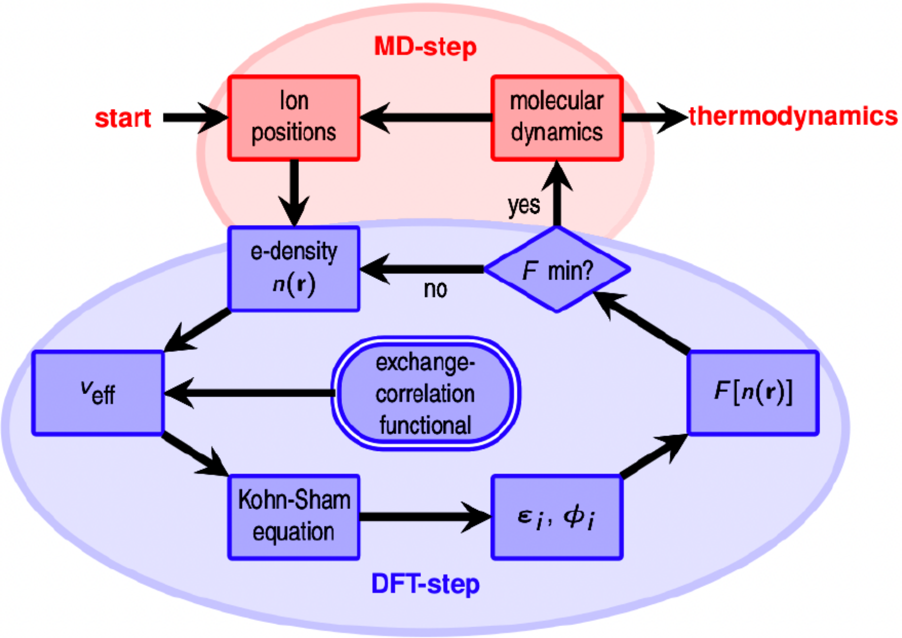

Figure 2.2: Schematic representation of the DFT-MD cycle as implemented in VASP®. Illustration from Lorenzen (2012)

2.3 Initial configurations

The initial positions of atoms used as input in our AIMD simulations were obtained from the cristobalite mineral structure from Downs and Palmer (1994), available in the American Mineralogist Crystal Structure Database. Cristobalite is one of the low-pressure and high-temperature polymorphs of SiO_2, typically stable up to 2000 K, and with a tetragonal structure. Its unit cell contains 12 atoms with lattice parameters established at $a = 4.97170$, $b = 4.97170$

and $c = 6.92230$ Å. At this configuration, SiO_2 has 16 electrons and 2.33 g/cm^3 at ambient conditions. In order to obtain a better representativeness of the system, we build a supercell by placing additional unit cells adjacently to each other, observing that the final shape approaches a cubic structure to maintain the isotropy of forces acting on the system. The unit cell was multiplied in a $3x3x2$ proportion along the aforementioned axis and resulted in a supercell with $a = 14.91510$, $b = 14.91510$ and $c = 13.84460$ Å as lattice parameters, summing 216 atoms and 1152 electrons. The new structure was, then, forced into a cubic structure with 15 Å of lattice (Figure 2.3) and served as the material for the subsequent pure SiO_2 simulations and as basis for the construction of the silica-water mixtures. The modification of the structure represents a difference of less than 10% in volume from the original supercell and does not have a significant impact on final results given that this study focus on equilibrated fluid phases.

The unit cell of cristobalite was used as basis for the construction of silica-water mixtures, where H_2O units were manually placed in the intermolecular space of the silicate chain, in order to have a evenly distribution of molecular types. We placed one, two and four H_2O molecules inside the unit cell and then continued to build the supercell in the same manner as previously done for pure SiO_2, resulting in three mixtures with silica-water proportions of 4:1, 2:1 and 1:1. The fourth system was constructed by removing alternately half of the H_2O molecules of the system, forming a 8:1 silica-water proportion. In terms of weight percent of H_2O, these systems vary from 3.61to 23.07 wt%. The respective concentrations, together with the total number of particles and electrons of each system is indicated in Table 2.2.

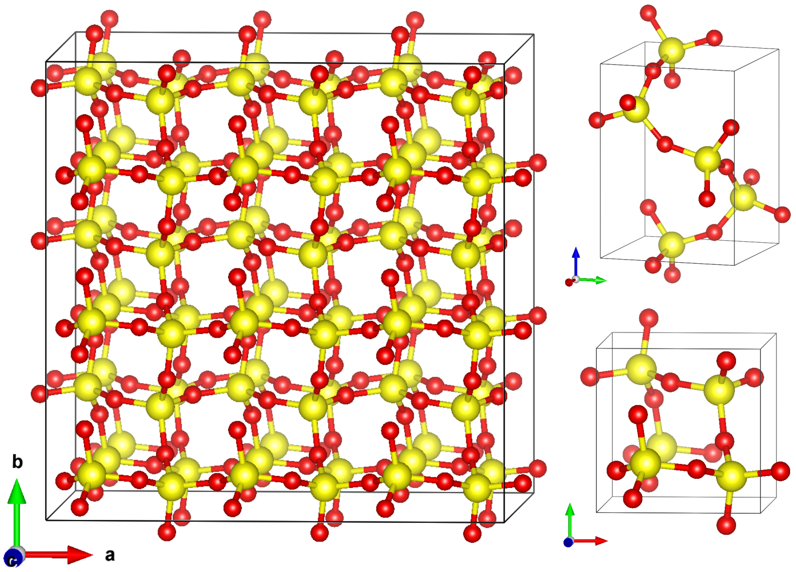

Figure 2.3: Initialization of the SiO_2 system structure. On the right upper side, the unit cell is represented along the a axis and on the right lower side it is represented along the c axis for a complete view of the cell. On the left side, is the final supercell with the inital atomic position adopted as starting configuration of the pure SiO_2 simulations. Red spheres represent oxygen atoms and yellow spheres represent silicon atoms.

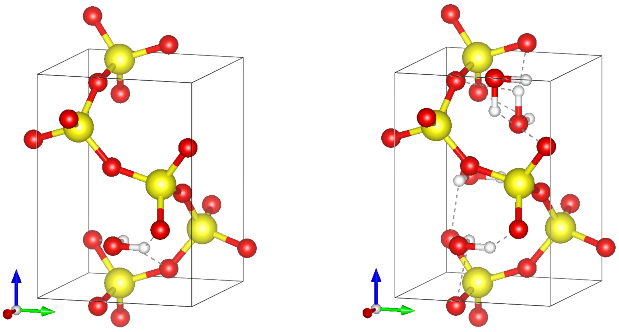

Figure 2.4: Unit cells of SiO_2 with interatomic water. On the left, the unit cell contains one molecule of water and on the right side, it contains 4 molecules of water. Hydrogen atoms are presented as white spheres.

Table 2.2: Summary of calculated systems at their fixed conditions.

System	Temperatures (K)	Densities (g/cm^3)	N° atoms	N° electrons
SiO_2	4000 - 7000	2.33 – 0.20	216	1152
$9H_2O.72SiO_2$	3000 - 5000	2.72 – 0.34	243	1224
$18H_2O.72SiO_2$	3000 - 5000	2.29 – 0.35	270	1296
$36H_2O.72SiO_2$	2000 - 4000	2.45 – 0.38	324	1440
$72H_2O.72SiO_2$	2000 - 4000	2.77 – 0.43	432	1728

2.4 Computational details

This work was carried using ab initio molecular dynamics methods (AIMD) applying density-functional theory (DFT) implemented in the Vienna Ab Initio Simulation Package (VASP; Kresse and Furthmüller, 1996). The exchange-correlation functional was treated based on Perdew-Burke-Erzenhof (PBE; Perdew et al., 1996) generalized gradient approximation (GGA), which considers the electron density and its gradient at a given point (Lee, 2017). The wave-functions are represented in the project-augmented wave (PAW; Blöchl, 1994) pseudopotentials, where the core electrons are frozen and only the valence electrons are explicitly considered in the calculations, with a cutoff energy to determine how many planewaves are used. The cutoff energy was set at 550 eV and the augmentation sphere at 800 eV, and the Brouillon zone was sampled at the gamma-point. Convergence tests can be found in the Appendix A.

The atoms were placed inside a cubic cell with periodic boundary conditions, according to the method described in the previous section. The simulations were performed in the canonical ensemble (NVT), where the temperature was controlled by the Nosé-Hoover thermostat (Nosé, 1984; Hoover, 1985). The choice of density and temperature was based on available phase diagrams for silicate systems (Melosh, 2007) along with predicted protolunar disk conditions (see Section 1), aiming specifically for the most likely region where the critical point is placed.

Simulations on anhydrous SiO_2 were performed on a cell containing 72 formula units, summing 216 atoms and 1152 electrons. The density varied from 0.2 to 2.33 g/cm^3 and temperature values were set at 4000, 4500, 5000, 5500, 6000 and 7000 K (Figure 2.5). Thermodynamic properties were calculated over time intervals of 1 fs and averaged over the complete time length, which varied from 10 to 70 ps depending on initial equilibration. Simulations on hydrated systems were performed on four different compositions, where the number of atoms and electrons of each individual system can be found on Table 2.2. Densities varied from 0.34 to 2.77 g/cm^3 and the temperature values were set to 2000, 3000, 4000 and 5000K, depending on the system (Figure 2.6). The time interval was set to 0.5 fs and the thermodynamic properties were averaged over 9 to 20 ps length, also depending on initial equilibration.

A total of 84 points were calculated for pure SiO_2 and 137 points for the hydrated systems dataset, summing a total of 221 computed systems. The results of the production runs were processed using the UMD package (Caracas et al., 2021), where initial equilibration steps were discarded.

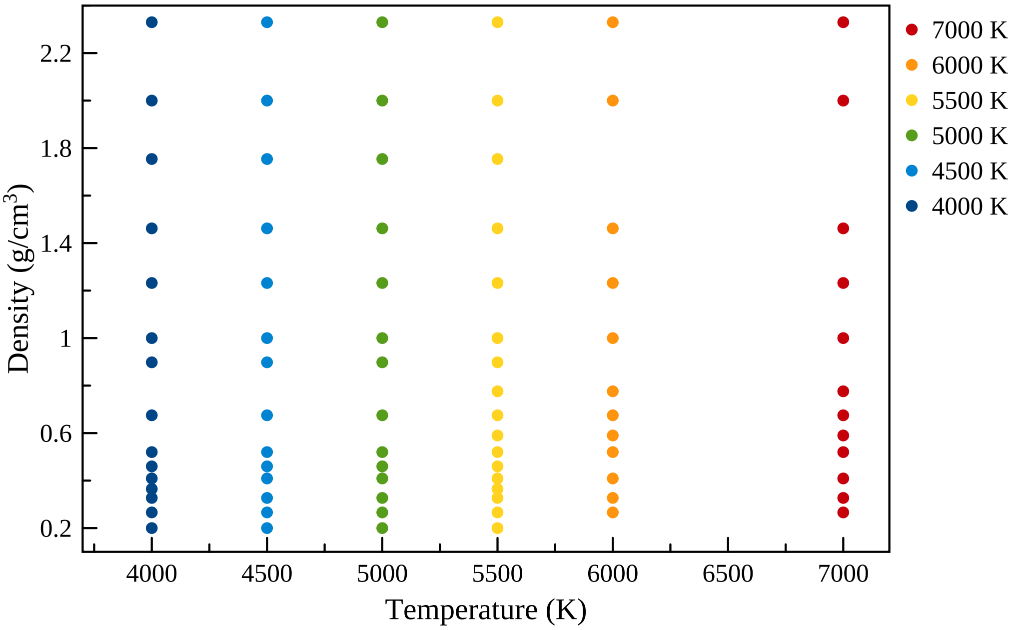

Figure 2.5: Overview of anydrous SiO_2 simulations. Each individual point represents one simulated system in its fixed density and temperature. Different colors represent different temperatures.

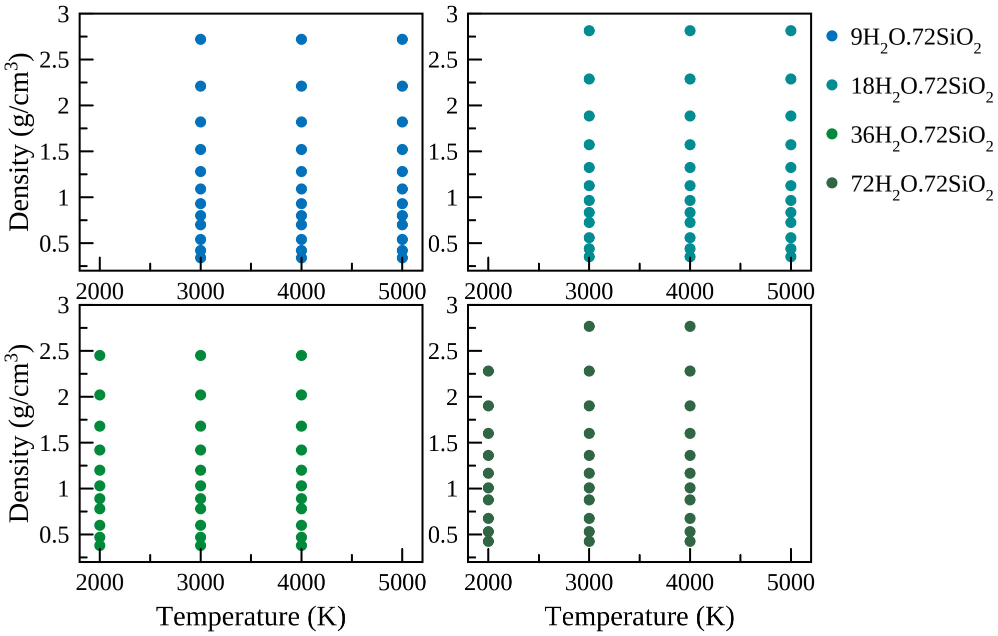

Figure 2.6: Scope of simulations on hydrated systems. Each panel represents an individual water-silica mixture, indicating every density and temperature state on which they were calculated. Upper panels show $9H_2O.72SiO_2$ on the left and $18H_2O.72SiO_2$ on the right side; lower panels show $36H_2O.72SiO_2$on the left side and $72H_2O.72SiO_2$ on the right side.

2.5 Equations of state and phase diagrams

The construction of the thermal equations of state P(ρ,T) is done by the compilation of the DFT-MD simulations dataset. Total pressure and internal energy are given by the sum of three quantities related to the ionic, electronic and interacting term contributions. The pressure at each density point is averaged from the loop of iterations and then computed to construct the isotherms. The ensemble of P(ρ,T) conditions defines the equations of state of the studied systems, on which we fit a third-order polynomial equation in order to approximate the behavior of phases that serve as basis for the construction of phase diagrams.

The first-derivative of the cubic polynomial fit gives the local minima and maxima of the respective isotherms. These local values aforementioned are defined as spinodal points, meaning that they delimit the thermodynamic stability of a phase-homogeneous fluid. The curve delimited by those points comprises the liquid-vapor coexistence dome and the metastability domain. To the left of the local maxima is the gas domain, whereas to the right of the local minima is the liquid domain. In the supercritical regime, liquid and gas behave as a continuous phase and, therefore, spinodals become undefined. The schematic phase-diagram as described above is illustrated in Figure 2.7

In the van der Waals equation of state, the critical constants relate to the van der Waals coefficients and the critical point is established at a flat inflection where the first and second-order derivatives are zero (Atkins et al., 2018). In order to estimate the critical constants of our systems, we use the linear regression of the second-order derivatives bracketed by the spinodal points to constraint the critical point pressure-density-temperature setting.

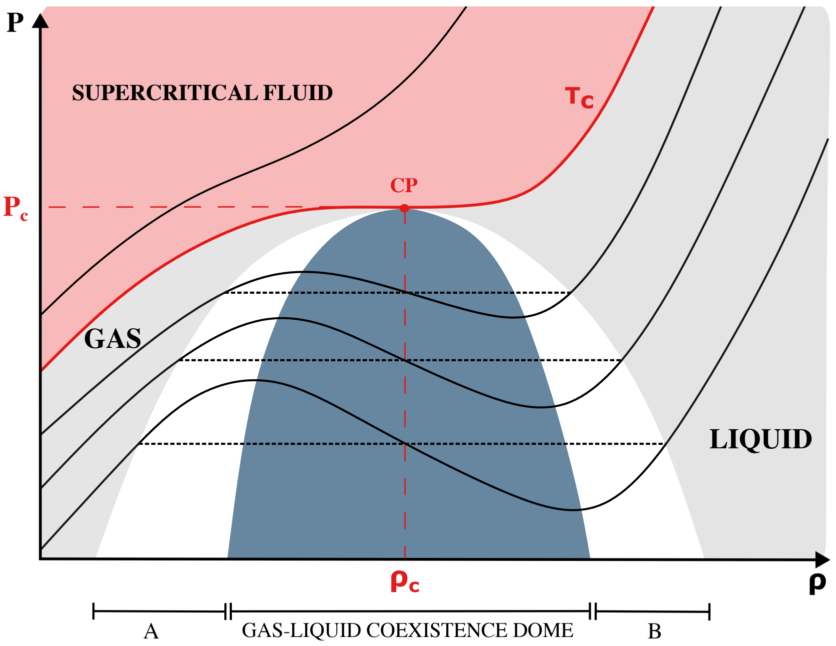

Figure 2.7: Phase diagram schematics in pressure-density-temperature space. Isotherms are indicated as solid lines varying with pressure (vertical axis) and density (horizontal axis). Local minima and maxima values of isotherms are spinodal points and define the limit of the gas-liquid coexistence dome (dark-blue area). Dashed lines represent the Maxwell construction of equal areas where the pressure is the equilibrium pressure and sets the metastability limit of homogeneity of the gas (A) and the liquid (B). Strictly gas or liquid regions are indicated as gray areas. Critical point (CP) conditions of pressure (P_c), density (ρ_c) and temperature (T_c) are indicated in red. The supercritical fluid regime is represented as the red area and is bounded by T_c.

2.6 Structural properties

2.6.1 Atomic pair distribution function and coordination numbers

Fluid structure is derived from the atomic ordering analysis given by pair distribution functions (PDF). They describe quantitatively the interatomic distances for a given atomic pair from a central atom at a given radial distance to its neighbors, as shown in Figure E.1a and expressed by the equation below:

$$g_{ij}(r) = \frac{V}{N(N-1)} \langle \sum_i \sum_{j \neq i} \delta(r - r_{ij}) \rangle \tag{2.12}$$

where r is the radial distance between particles i and j in a system with N atoms with volume V, δ is the Dirac delta function and $\langle\rangle$ is the ensemble average. The first coordination sphere of a given particle is defined by the nearest neighboring atoms placed in a shell at distance r0 (Figure E.1a). In the g(r) distribution (Figure E.1b), the nearest neighbors are delimited by the first minimum trough and represents the maximum possible bond length expected for the atomic

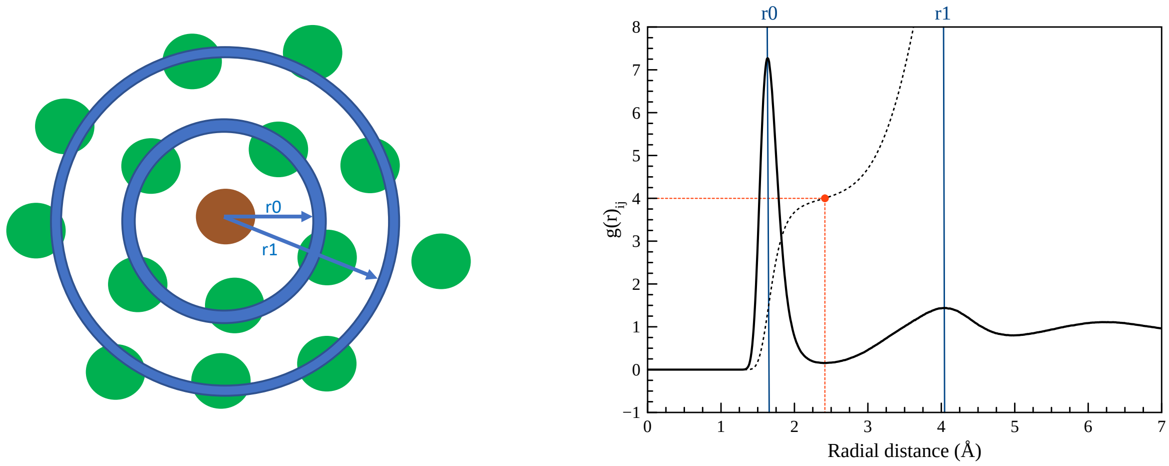

(a)

(b)

Figure 2.8: Representation of the pair distribution function analysis. a) Central atom in brown and neighboring atoms in green. The first coordination sphere is at radial distance r0 and the second coordination sphere is at radial distance r1. b) Schematic diagram showing the pair distribution function of an atomic pair. Dashed line shows the integral of the function and the red point represents the derivative of the curve located over the first minimum through, indicating the coordination number of the system.

pair (Figure E.1b), where the first maximum peak contains the average interatomic distance and indicates the average bond length of the same pair. Because of the repulsive forces that prevent two atoms from overlapping, the pair distribution function approaches zero at small distances. The second coordination sphere is defined by the second nearest neighboring particles and accounts for the polymerization of the fluid (Figure E.1a). Its average radial distance is given by the second peak in the g(r) distribution (Figure E.1b).

The structure of the atomic pair reflects directly the general structure of the fluid. The sharpness or broadness of the peaks indicate the positioning of the atoms in space and, therefore, it becomes possible to estimate the phase state of the system. PDF also provide information regarding the different molecular species present in the fluid, where the integral of the pair distribution function up to the first minimum yields the coordination number of the atomic pair (Figure E.1b), as in:

$$C_{(r_m)} = \int_0^{r_m} g(r) 4\pi N r^2 dr \tag{2.13}$$

where C is the coordination number and r_m is the radial distance at the first minimum trough of the PDF.

2.6.2 Polymerization analysis

Silicate systems are known for forming polymers of variable length depending on thermodynamic conditions. The degree of connectivity of the chain on such systems is associated with fluid properties, such as viscosity, self-diffusion coefficients and more (de Clermont Gallerande et al., 2020), which are key to understand the behavior of silicate systems at larger scales. The analysis of the variation on coordination numbers proportions can indicate the extent of molecular dissociation in the fluid. Considering this, we propose a new measurement for estimating the degree of polymerization based on the evaluation of the relation between coordinations of silicon and oxygen atoms with respect to each other. The relation is given by the weighted sum of the coordination of silicon with respect to oxygen over the weighted sum of the coordination of oxygen with respect to silicon, expressed as:

$$V_{T,\rho} = \frac{\sum[SiO_x]x}{\sum[OSi_y]y} \tag{2.14}$$

where the sum of the fractions of all Si-O coordination numbers x weighted by their index x over the fractions of all O-Si coordination numbers y weighted by their index y yields the polymerization degree V at a given temperature T and density ρ. The general evaluation of this relation allows the assessment of the Si-O-Si bridging and describes the structure of the fluid by providing the amount of overall bonding between the two atoms.

2.7 Transport properties

The motion of particles is measured directly from the calculated trajectories in terms of the mean-square displacement (MSD) and self-diffusion coefficient (D). The MSD scales linearly with time in the fluid and is given by the deviation of a initial position in respect with time, as described in the equation:

$$MSD = \langle [r_i(t_0 + t) - r_i t_0]^2 \rangle \tag{2.15}$$

where r is the position of the particle i from a initial time t_0 to time t, over the ensemble average $\langle\rangle$. The slope of the MSD yields the self-diffusion coefficient according to the relation below:

$$D = \frac{1}{6} \lim_{t \to \infty} \frac{MSD_t}{t} \tag{2.16}$$

The diffusion coefficient is calculated for every simulated point and fitted with a linear function in order to describe the dynamic behavior of the atoms at fixed temperature or fixed density.

Chapter 3

Pure SiO_2 system

Contents

3.1 Phase diagram and the critical point

From our ab initio molecular dynamics calculations performed on anhydrous SiO_2 systems, we build our equations of state and present the results in the pressure-density phase diagram shown in Figure 3.1. A total of six temperatures were simulated, on a range varying from 4000 to 7000 K. For each temperature-density condition, the value of the pressure was computed and is represented by an individual point in the aforementioned diagram. A table with all discrete values of pressure is given in Appendix B.1. We started from the normal density of cristobalite (2.33 g/cm^3) at all isotherms and we sample the phase space by gradually increasing the cell volume in order to reach lower densities, down to 0.20 g/cm^3. Reported data on SiO_2 (Green et al., 2018; Melosh, 2007) showed that previous predictions of the critical point for this material should be generally between 5000 and 6000 K, with a most likely value approaching 5400 K. Considering this, we space isotherms every 500 K up to 6000 K and we increase the number of simulation points in order to obtain a better resolution in these conditions.

The dataset is fitted with a cubic function up to 2 g/cm^3 for each isotherm in order to represent the mean behavior of the system. The minima and maxima values are extracted by calculating the first derivatives of the fitted curve and represent the spinodal points, as explained in detail in section 2.5. The region bracketed by the spinodal point along with the linear regression of the second order derivatives indicates the most likely region for the critical point. We place the critical point of SiO_2 between 0.6 and 0.85 g/cm^3, 5000 to 5500 K and 0.15 to 0.25 GPa. Above 5500 K, the spinodal points are indistinct and, therefore, we define SiO_2

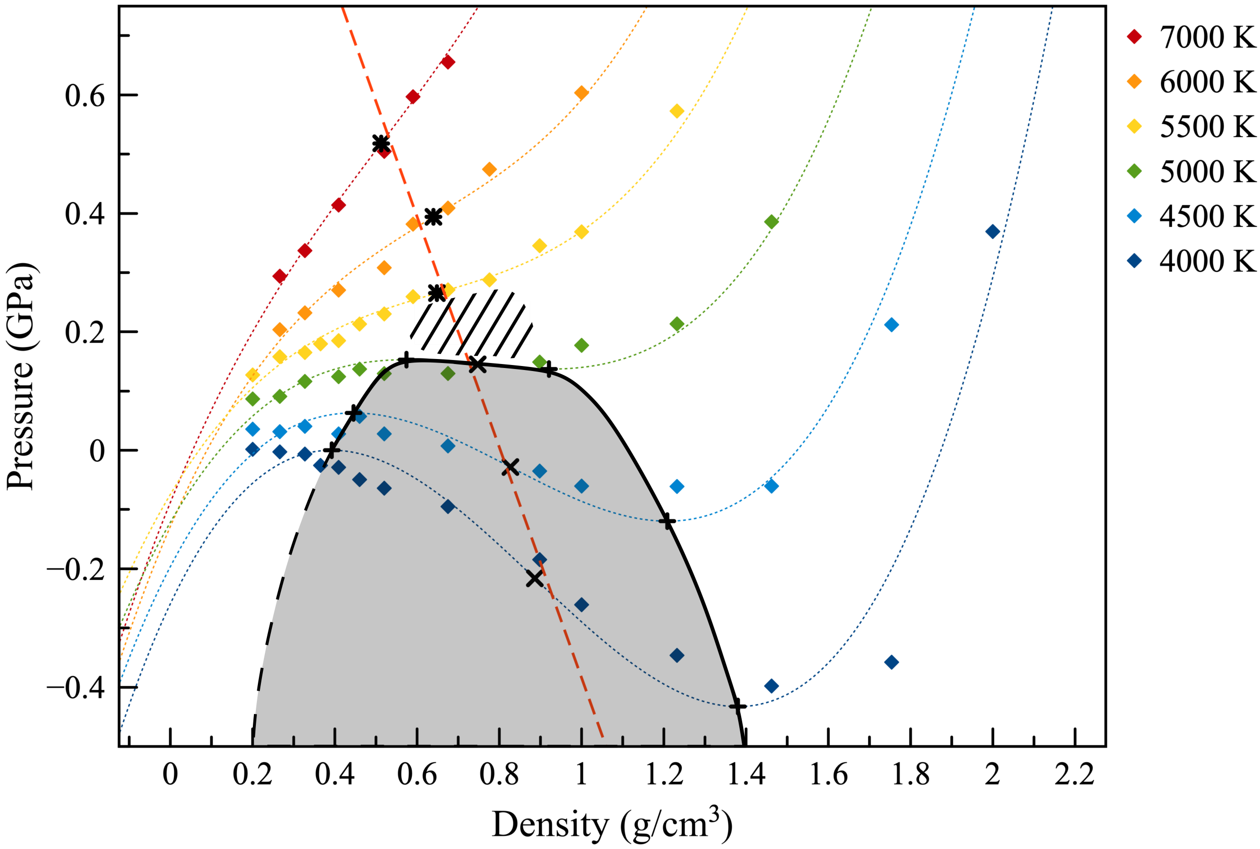

Figure 3.1: Equations of state of pure SiO_2 and phase diagram. The diagram shows the variation of pressure as a function of density along different isotherms. Diamond symbols represent simulation points, where the different colors represent different temperatures. Dashed colored lines along the isotherms are third-order polynomials fitted for each individual temperature. Crosses mark liquid and gas spinodal given by local minima and maxima points. The points indicated with (x) are second-order derivatives of the given isotherms and the light-red dashed line is a linear fit of such derivatives. The spinodal points along with the linear fit, bracket the critical point region, indicated as the hatched area in the diagram. Gray filled area indicates the liquid-vapor coexistence dome.

in supercritical state. We define the liquid-vapor coexistence dome between the liquid and gas spinodals, defined by the gray area in Figure 3.1. The binodal curve defining the metastability region of the fluid is not represented in this phase diagram.

Critical points of rock-forming silicate minerals have been vastly documented (Kobsch, 2020; Kobsch and Caracas, 2020; Xiao and Stixrude, 2018; Townsend et al., 2020; Melosh, 2007; Green et al., 2018). We show in Figure 3.2 the temperature-density critical constraints reported in the literature on the different minerals, along with the critical point of SiO_2 as calculated in this study. Minerals containing refractory elements such as calcium, aluminum and magnesium, report critical points at higher temperatures, where anorthite ($CaAl_2Si_2O_8$) is considerably higher in comparison to the other minerals, placed in between 7000 and 7500 K (Kobsch, 2020), follow by forsterite between 6550 – 6750 K ($MgSiO_3$; Xiao and Stixrude, 2018) and enstatite 6040 – 6440 K (Mg_2SiO_4; Townsend et al., 2020). Alkali feldspars form a solid solution with interchangeable cations and behave similarly with respect to their near

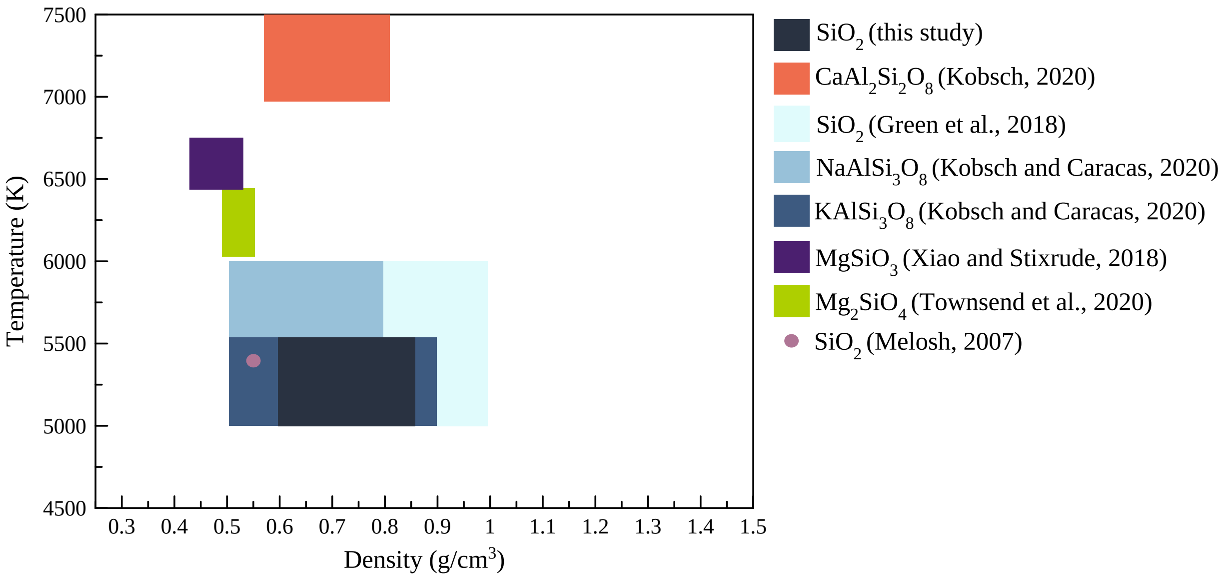

Figure 3.2: Critical points of major rock-forming silicates. Diagram of temperature as a function of density with the critical point of SiO_2 as calculated in this work. Silicates described in the literature are also shown for reference: anorthite, $CaAl_2Si_2O_8$ (Kobsch, 2020); orthoclase, $KAlSi_3O_8$, and albite, $NaAlSi_3O_8$ (Kobsch and Caracas, 2020); SiO_2 (Melosh, 2007; Green et al., 2018); forsterite, $MgSiO_3$ (Xiao and Stixrude, 2018); and enstatite, Mg_2SiO_4 (Townsend et al., 2020).

critical characteristics, where their critical temperature approach that of SiO_2. The critical point of SiO_2 as calculated in this work shows a good agreement with previous reported values that placed it at 5400 K, 0.55 g/cm^3 and 0.19 GPa (Melosh, 2007) and, more recently, between 5000-6000 K, 0.5 – 1.00 g/cm^3 and 0.2 – 0.5 GPa (Green et al., 2018).

The vast majority of works presented in Figure 3.2 estimate critical points by applying ab initio molecular dynamic techniques (Kobsch, 2020; Kobsch and Caracas, 2020; Xiao and Stixrude, 2018; Townsend et al., 2020; Green et al., 2018), with differences in the use of such techniques by varying parameters and statistical ensembles. For instance, the energy cutoff was set at 500 eV by Xiao and Stixrude (2018) and 800 eV by Townsend et al. (2020). Higher accuracy is generally expected when using higher values for energy cutoff, however, simulations take oftentimes longer to calculate. Observing that the system has properly converged at a lower cutoff, results will be precise and calculated in a shorter period of time. The critical point of silica published by Melosh (2007) is estimated from an analytical equation of state, where its construction is discussed in Chapter 1. The use of fundamentally different techniques towards the same goal is mutually beneficial, since they can complement and corroborate each other. Recent work has also shown benefits in adding an experimental bias onto numerical simulations (White et al., 2017).

3.2 Structure of the fluid

3.2.1 Pair distribution functions

We describe the structure of the fluid starting from a pair distribution function analysis. We compute the PDF for Si-O and O-O pairs at all densities (Figure 3.3) and temperatures (Figure 3.4). We present a detailed table containing positions of maxima and minima on the complete span of pair distribution functions curves in the appendix C. The nearest neighbors are represented in the first coordination sphere, where the first peak represents the average bond length of the represented pair. The second coordination sphere accounts for the general polymerization of the fluid. As mentioned in section 2.6, the structure of the PDF reflects directly the structure of the fluid. The beginning of the PDF reflects the repulsive forces acting between the atoms that prevent them to overlap, which can differ up to 15% as a function of variations in temperature-density of the specified pair.

Figure 3.3 shows a comparison of pair distribution functions in the fluid below (4000 K) and above (7000 K) critical conditions for Si-O and O-O pairs spanning all calculated densities. Panels on the left represent the function at 4000 K and panels on the right the function at 7000 K. The upper part stands for Si-O, whereas the lower part stands for O-O. At all conditions, we observe a general broadening of the peaks as the density decreases. This width increase suggests a looser packing of the structure, which is also consistent with dissociation of molecules related with increasing vaporization of the fluid. With the decrease in density, we also generally observe the placement of the first minimum well above zero, indicating an increasing dynamic behavior of the particles (Green et al., 2018). Such behavior becomes remarkably significant for O-O pairs at 4000 K in densities equal and below 0.27 g/cm^3, where the fluid would be well inside the gas phase region.

At 4000 K, the fluid is below critical and mostly inside the liquid-vapor coexistence dome depending on the density (see Figure 3.1). The position of the first peak of the Si-O pair varies from 1.64 Å at 2.33 g/cm^3 to 1.63 Å at 0.20 g/cm^3, with a mean value of 1.63 Å. First minima values vary from 2.41 Å at 2.33 g/cm^3 to 2.51 Å at 0.20 g/cm^3, with a mean value of 2.49 Å. However, at 7000 K where the fluid is at supercritical conditions, we observe the position of the first peak varying from 1.64 Å at 2.33 g/cm^3 to 1.57 Å at 0.27 g/cm^3, with a mean value of 1.61 Å, and first minima values varying from 2.56 Å at 2.33 g/cm^3 to 2.84 Å at 0.27 g/cm^3, with an average of 2.69 Å. We observe that the second coordination sphere is more prominent at 4000 K, suggesting a higher level of organization and degree of polymerization of the fluid in comparison with 7000 K.

Considering the O-O pair, at 4000 K the main peak is located between 2 and 3 Å and is related to the positioning of oxygens within the tetrahedron. It varies from 2.68 Å at 2.33 g/cm^3 to 2.72 Å at 0.20 g/cm^3, averaging over 2.72 Å. We observe an incipient peak between 1 a 2 Å at densities equal to 2.00 g/cm^3 or lower. It becomes more significant at lower densities and it represents the formation of diatomic oxygen molecules. At 7000 K, tetrahedra oxygen peak shifts slightly to the right, varying from 2.67 Å at 2.33 g/cm^3 to 2.86 Å at 0.27 g/cm^3, with an average of 2.80 Å. The molecular oxygen peak is present at all densities and becomes dominant at densities equal to 0.78 g/cm^3 or lower.

By fixing the value of the density, we are able to compare and evaluate the effects of

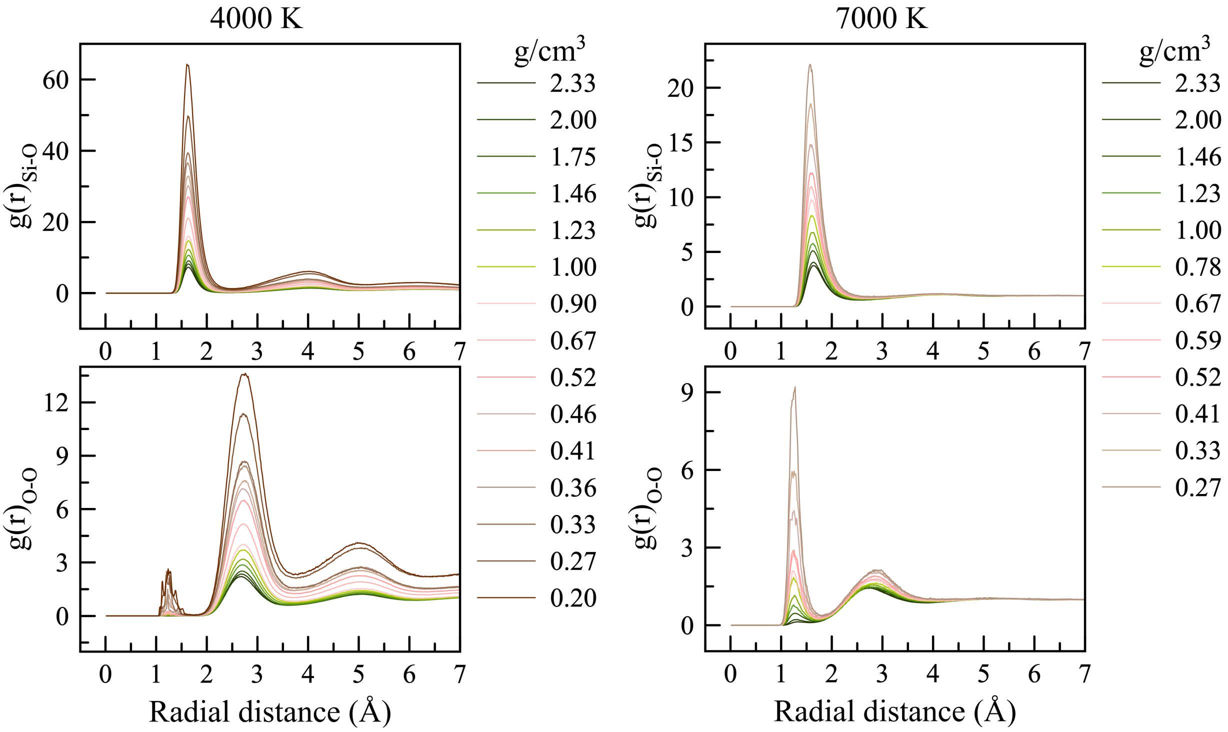

Figure 3.3: Pair distribution function analysis for the full interval of simulated densities at selected temperatures. Left side panels show the distribution at 4000 K and panels on the right side shows distributions at 7000 K. Upper panels show Si-O pairing and lower panels shows O-O pairing. The span of densities at 4000 K goes from 2.33 to 0.20 g/cm^3. The span of densities at 7000 K goes from 2.33 to 0.27 g/cm^3.

temperature onto the organization of the structure. We study the structural behavior variation at 2.33 g/cm^3 and 0.27 g/cm^3 for every isotherm, as shows in Figure 3.4. With increasing temperature, the peaks also become wider and the second coordination sphere decreases. Our mean values of bond length of the Si-O pair vary from 1.63 Å at 4000 K to 1.62 Å at 4500 and 5000 K to 1.61 Å at 5500 K and above temperatures. We observe a dependency of molecular oxygen formation with the temperature, represented by the emerging of the characteristic peak that increases in height with increasing temperature in both compared densities. This peak becomes prevalent at temperatures equal or superior to 5500 K, meaning that they become dominant when the fluid is in the supercritical domain.

For both densities, the first trough is placed above zero and the second coordination sphere decreases with increasing temperature. At 2.33 g/cm^3, the mean distance of the Si-O has a small variation with temperature, approximated at 1.64 Å at all temperatures. For the O-O tetrahedron pair, the distance varies between 2.67 and 2.68 Å with an unspecific relation with temperature. We also observe the effect of thermal expansion in pair distribution functions at 2.33 g/cm^3, marked by the widening of the peaks. However, this effect is less evident at low density, where we mostly observe a general asymmetry and shift of the main peaks. At 0.27 g/cm^3, Si-O bonds vary from 1.63 Å at 4000 K to 1.57 Å at 7000 K, with an average value of 1.59 Å.

Our results are consistent with reported data in the literature. Typical values of Si-O bond

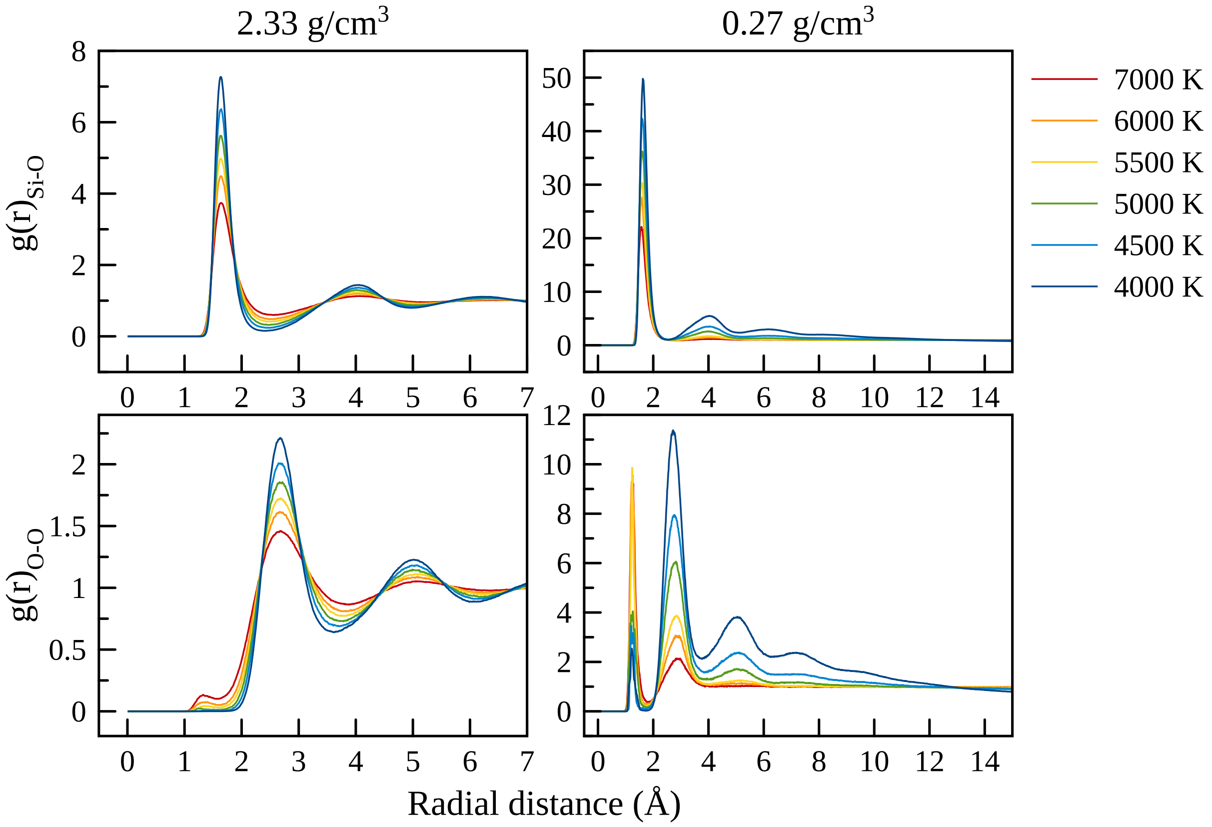

Figure 3.4: Pair distribution function of the Si-O and O-O pair at different temperatures and fixed densities. Upper panels show Si-O pairing and lower panels show O-O pairing for all temperatures in both cases. Left panels show the variation of the distribution at 2.33 g/cm^3, whereas right panels show the variation of the distribution at 0.27 g/cm^3. The total radial distance is giving in half of the size of the simulation box. Therefore, the horizontal axis for the 0.27 g/cm^3 diagrams go up to 15 Å given that the lattice for SiO_2 at such conditions is 30 Å, whereas for the diagram with density of 2.33 g/cm^3 the radial distance goes up to 7 since the lattice for those simulations were of 14.554 Å.

length can vary from 1.564 up to 1.720 Å depending on materials, thermodynamic conditions and methods applied, as reported by numerous researchers (Baur, 1971; Gibbs et al., 1972; Baur, 1977; Dove et al., 1997; Green et al., 2018) and by the Computational Chemistry Comparison and Benchmark Database of the National Institute of Standards and Technology of the United States. The average value, however, is placed around 1.62 Å. The tetrahedral oxygen distancing is typically close to 2.63 Å (Dove et al., 1997), whereas diatomic oxygen bond length is reported varying from 1.21 to 1.36 Å (Zaichenko et al., 2020). Peak shift and asymmetry have been reported in pair distribution functions and could be related to an increase in anharmonicity of the potential with increasing temperatures and the shape of typical inter-atomic interaction potentials (Ding et al., 2014).

The decrease in the average expected bond length of the Si-O pair with respect to the decrease in density is evidenced by the shift to left of the main peaks. This behavior can be explained by the increasing dissociation of the fluid at lower densities, meaning that not all of the Si-O pair is inside the tetrahedron and is increasingly in the molecular form. The same mechanism can explain the variation in bond values observed as a function of temperature at

0.27 g/cm^3. The density-temperature Si-O bond length variation is shown as a function of energy in Figure 3.5.

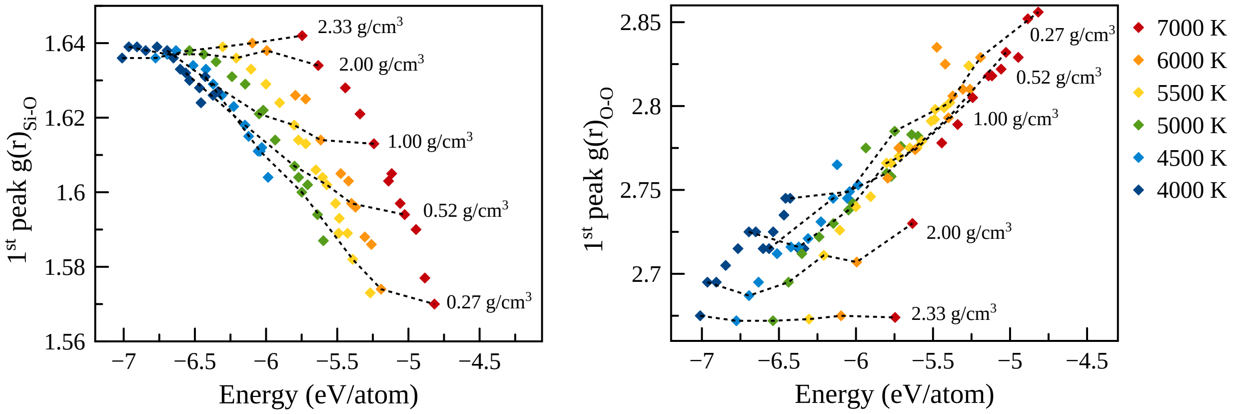

Figure 3.5: Position of the first peak of the Si-O pair distribution function of the full extent of simulated temperatures as a function of energy. Dashed lines represent isochoric variation of the position-energy relation.

The shift to the right observed in the oxygen tetrahedral distancing peaks can be related to the thermal expansion (Ding et al., 2014). Moreover, molecular oxygen bond length was reported to decrease in a nearly direct relation with the increasing of stretching frequency in some compounds (Cramer et al., 2003), however it can also be related to the formation of differently charged diatomic oxygen species.

3.2.2 Coordination numbers

Crystallographic principles can be applied to melts (Mysen, 1983). It is known that the coordination of silica in solids can vary directly with pressure, notably from 4-folded at ambient pressures to 6-folded Si-O at high pressures. In the fluid domain, the organization of SiO_2 can also adapt to the conditions presented. We calculate the fraction of all Si-O species in the fluid starting from the pair distribution function and present it for each density throughout the simulated time, as shown in Figure 3.6. We once more compare the results at conditions below and above critical, at 4000 and 7000 K, respectively.

At 4000 K, there is a major dominance of 4-folded silica at all densities and the fluid is still well polymerized. Nevertheless, as we move towards the gas domain at lower densities, coordination numbers gradually decrease with the formation of smaller Si-O clusters. As mentioned previously, at 4000 K the fluid is inside the liquid-vapor coexistence dome. At 0.20 g/cm^3, the proportion of 3-folded silica becomes important with a significant increase in coordinations 1 and 2 as well. This behavior is consistent with previous observation on the shift of the Si-O peak in the pair distribution functions described above.

At 7000 K, the dominance of 4-folded silica disappears and the coordination number becomes highly dependent on the density. Lower densities have an increase in lower coordinations and decrease in proportions of coordinations 5 and 6. The average CN transitions from 4 at 2.33 g/cm^3, to 3 at 0.78 g/cm^3 and, finally to 2-1 at 0.27 g/cm^3. The 3-folded silica gradually increases at densities from 2.33 to 1.23 g/cm^3 and starts to decrease from 1.00 to 0.27 g/cm^3, when the abundance of CN 1 and CN 2 is more significant. This behavior suggests that the degree of dissociation in the supercritical regime relies on the density of the fluid.

We further analyze behavioral variations of the system with respect to temperature at fixed densities (Figure 3.7). On the left panel, we describe CN proportions at 2.33 g/cm^3 and on the right panel, we describe those at 0.27 g/cm^3. At normal density (2.33 g/cm^3), silica is primarily in tetrahedral configuration, evidenced by the dominance of peaks at CN 4. There is a direct relation between temperature and the proportion of species in the fluid. The dissociation is favored with the increase in temperature, where 2 and 3-folded silica is formed. However, the mean pressure varies from 2.71 GPa at 4000 K to 8.47 GPa at 7000 K, which also account for the formation of 5 and 6-folded silica. Conversely, CN 4 decreases in proportion with the escalation of temperature, but remains significant.

At 0.27 g/cm^3, the main coordination number varies directly with temperature. It shifts from CN 4 at 4000 K to CN 1 at 7000 K in a much more even distribution. Higher packing of silica gradually decreases in favor of the lesser packed. The silica is no longer dominantly in tetrahedra and is much more depolymerized.

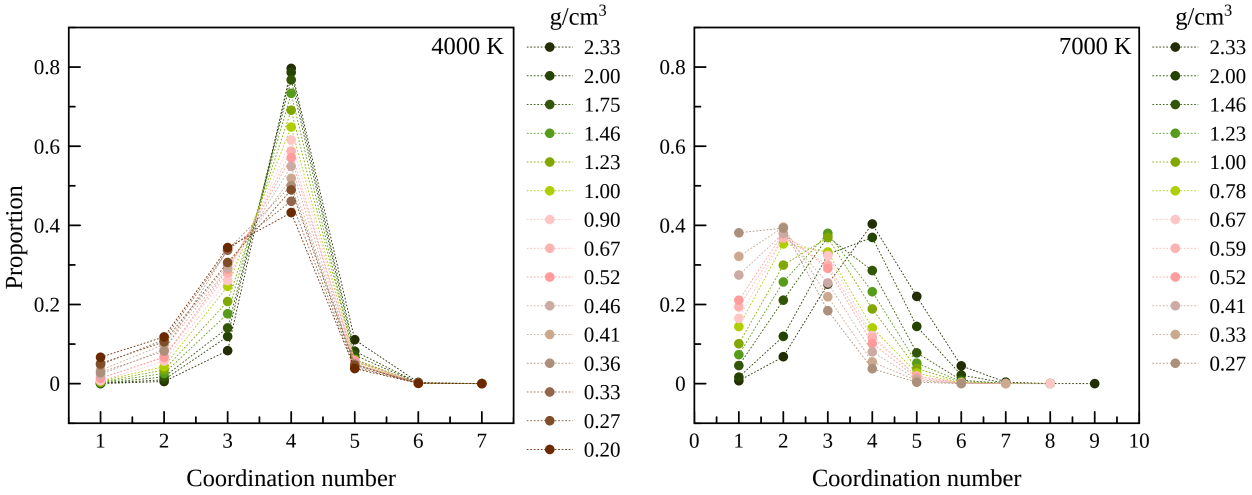

Figure 3.6: Proportion of coordination numbers per density at fixed temperature. On the left, the panel shows proportions from 0.20 to 2.33 g/cm^3 at 4000 K. On the right, the panel shows proportions from 0.27 g/cm^3 to 2.33 g/cm^3 at 7000 K.

3.2.3 Polymerization

Silicate materials are known for the long polymerization chains. The extent of the polymerization alters the viscosity, which ultimately can affect the distribution of volatiles in the protolunar disk (Charnoz and Michaut, 2015). We establish the polymerization degree as a relation of the total weighted sum ratio (V_{total}) of the coordination of silicon with respect to oxygen (represented as Si-O_x) and that of oxygen with respect to silicon (represented as O-Si_y), as shown in Figure 3.8 and better detailed in section 2.6.2. Pair distribution functions are restricted to the positioning of atoms in space rather than an analysis of bonding electrons between atoms. Therefore, we have to interpret carefully the results given by such method.

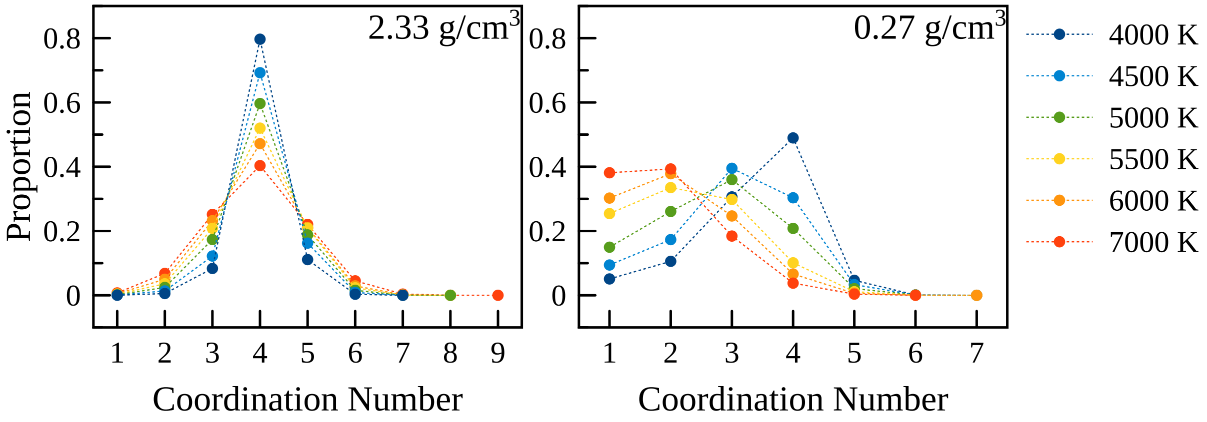

Figure 3.7: Proportion of coordination numbers per temperature at fixed density. Left panel shows the variation in proportion of coordination numbers at a density of 2.33 g/cm^3 from 4000 to 7000 K, whereas the right panel show the variation at a density of 0.27 g/cm^3 at the equal temperatures.

However, we observe a strong correlation between thermodynamic properties and the structure of the fluid. As we decrease density, we exit the liquid domain and enter the domain of the gas phase. It becomes increasingly dominated by smaller molecular clusters, which in comparison would have expectedly a lower viscosity and diffuse more rapidly.

In Figure 3.8, we present the polymerization ratio as a function of density for every isotherm. The dashed line sets the critical limit, where isotherms below are in supercritical state. Above this line, we explicitly separate the domains of the main phases where the points are located with respect to the positioning inside the phase diagram built and described in section 3.1.

The V_{total} ratio overall varies from 1.498 (Figure 3.9b) to 2.000 (Figure 3.9a). A table containing the weighted sum of x values in Si-Ox, of y values in O-Si$_y$ and the final total ratio V_{total} per temperature and density is given in Appendix D. At 2.33 g/cm^3 the fluid is well polymerized at 4000 K, where V is equal to 2.000. With the increase in the temperature, the network gradually starts to break and the value of V decreases to 1.965. This deviation pattern between isotherms concerning V values is repeated throughout the full extent of simulated densities, due to the steeper variation observed at higher temperatures. The deviation is significantly large at 0.27 g/cm^3, where the gap between polymerization degrees at 4000 and 7000 K is of more than 25%. This behavior indicates that the temperature has a stronger effect at low densities and the break of the network happens more rapidly at such conditions.

Inside the liquid domain, we observe a steady linear behavior directly related to the density-temperature variations. In the gas domain, the behavior is more erratic and less predictable in the sense that no linearity is observed. However, the general descending trend of polymerization is maintained. It is worth to note that metastable phases are not defined in this diagram, but they should be considered inside the individual gas and liquid domains. In supercritical state, the structure of the fluid also depends on the thermodynamic properties and dissociation rate continues to vary accordingly.

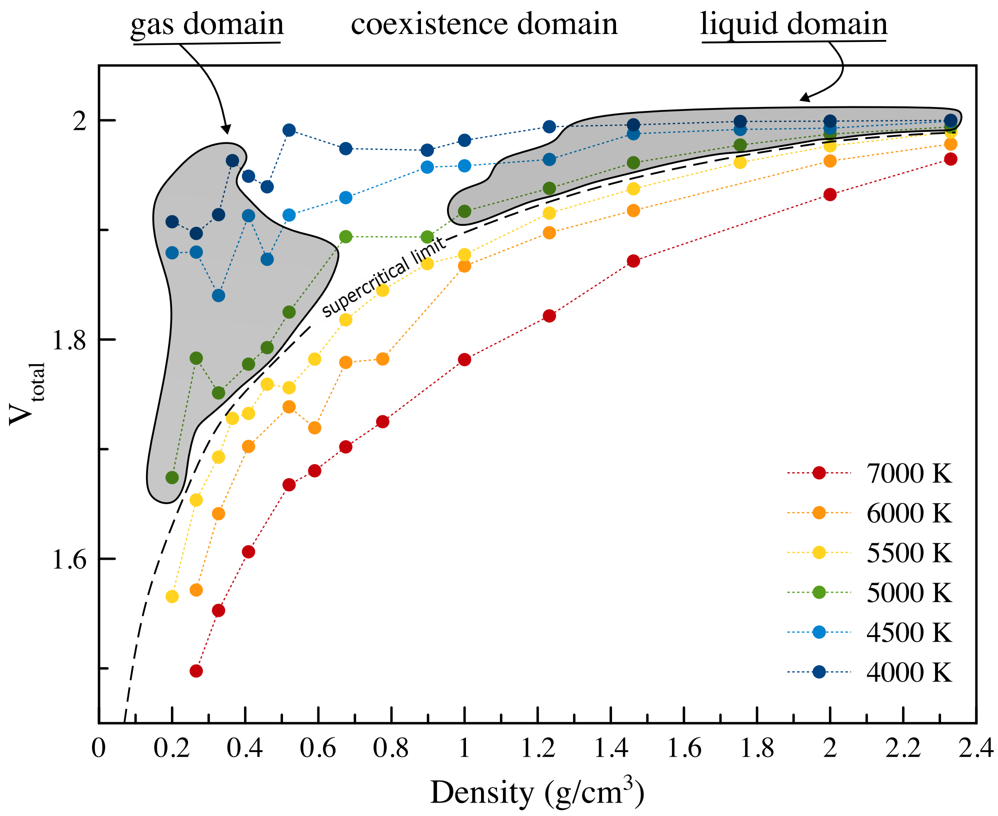

Figure 3.8: Polymerization of the silicate fluid in different domains. The total ratio of Si-O$_x$ over O-Si$_y$ is represented as a function of density. Gray areas show the gas domain region at low densities and the liquid domain region at higher densities. In the middle of these two regions is the coexistence area. The dashed line marks the limit of the supercritical regime, where all points below this line are above critical conditions.

In a different analysis, we compare the V_{total} ratio as a function of pressure (Figure 3.10). Here, black lines are showed for reference. They mark the maximum value of V_{total} at 2.000 and the minimum value of pressure at zero. It becomes evident the relation of the network stability with pressure, specially at temperatures above critical (i.e. 5500, 6000 and 7000 K). Isotherms below critical conditions show steady V values until they reach zero pressure, when they vertically drop in a stronger dependency with density. Nevertheless, supercritical systems show a smoother variation of the polymerization degree as a function of pressure, indicating a stronger effect of pressure in the structure of the fluid at the specified temperatures.

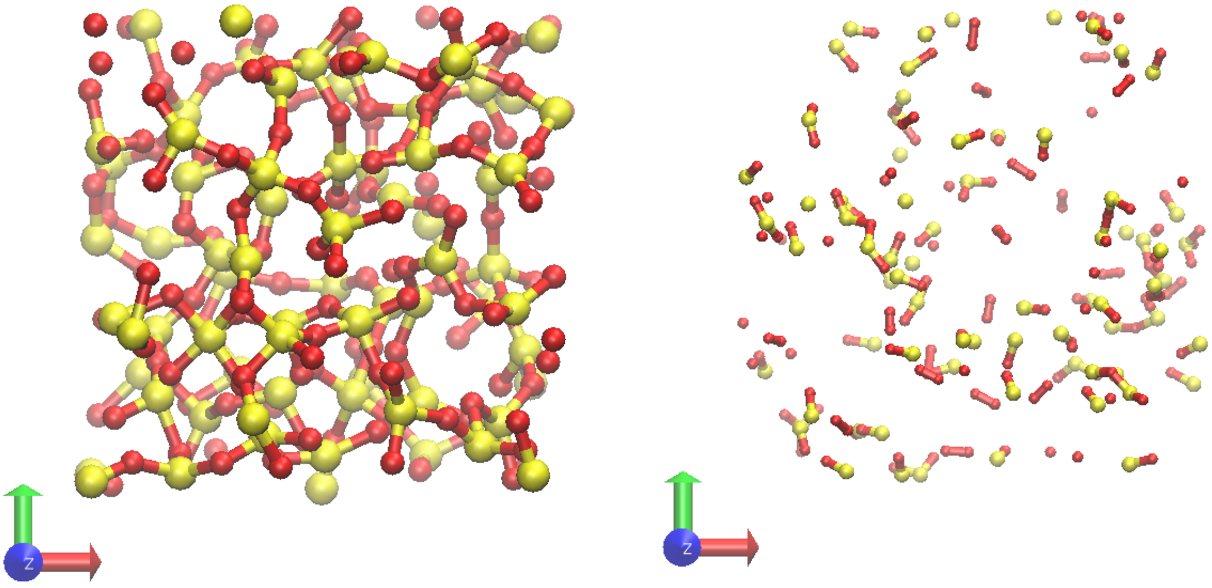

(a) (b)

Figure 3.9: Visualization of different degrees of polymerization. (a) Pure SiO$_2$ at 4000 K and 2.33 g/cm^3, where $V_{total} = 2$. (b) Pure SiO$_2$ at 7000 K and 0.27 g/cm^3, where $V_{total} = 1.498$.

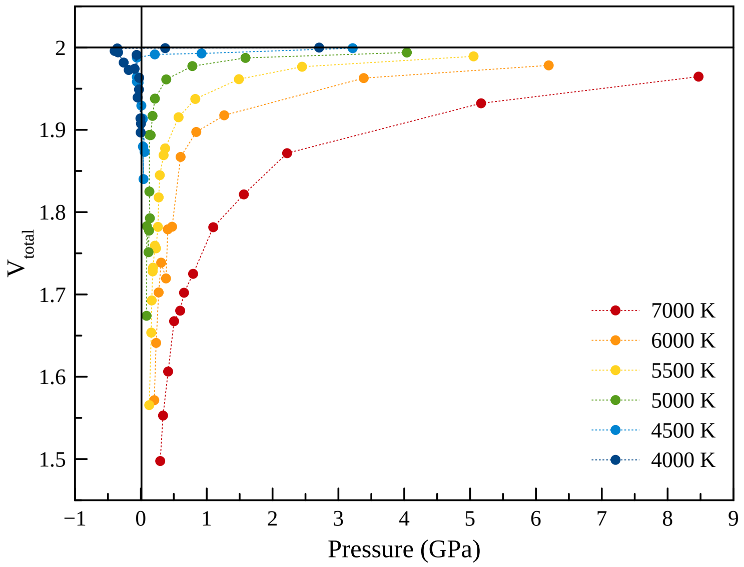

Figure 3.10: Polymerization as a function of pressure at different temperatures. Horizontal and vertical black lines are shown for reference for the maximum value of the V at 2 and for the pressure at 0 GPa.

3.3 Dynamic behavior of atoms

Diffusion is a key property and highly dependent on the degree of polymerization of the fluid and viscosity. The self-diffusion coefficients of silicon and oxygen are calculated based on the transport rate obtained from their mean square displacement slope. The mean square displacements are given in Appendix E. We compare self-diffusion coefficients at different temperatures and densities, on the full scope of simulated conditions of the pure SiO$_2$ system. Displacements of oxygen are generally slightly larger than that of silicon at similar conditions due to their difference in atomic mass.

Figure 3.11 shows the self-diffusion coefficients as a function of density of Si and O. At fixed temperature, we observe a decrease in the diffusion with increasing density. Generally, the decrease is steeper at lower densities and less expressive at higher densities. The rate of displacement in a direct relation with the temperature, incrementally escalating as temperature increases.

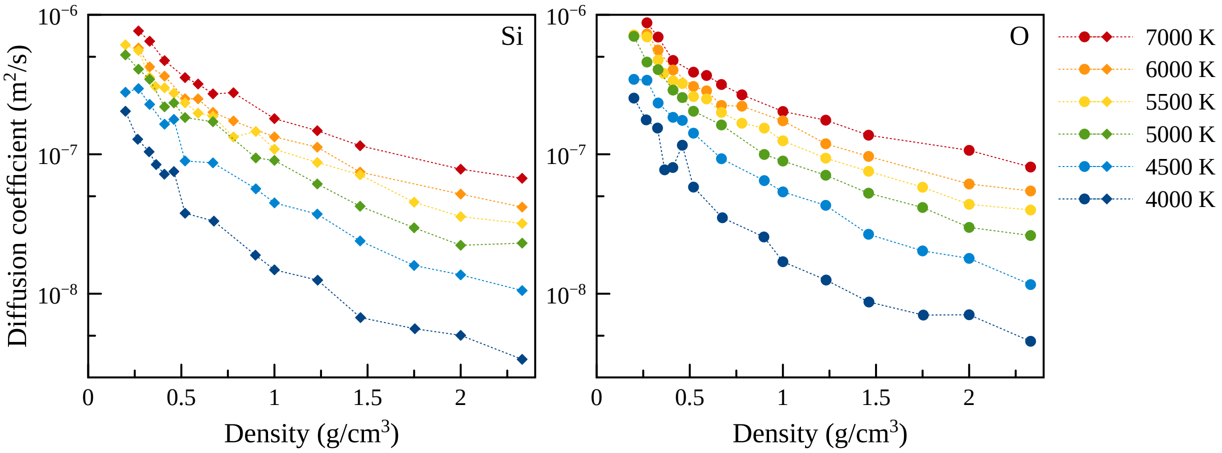

Figure 3.11: Diffusion coefficients of Si and O. Diagrams are presented as a function of density for all temperatures. Left side panel: silicon; right side panel: oxygen.

In another perspective, we evaluate the variation of the self-diffusion coefficients as a function of temperature at fixed densities (Figure 3.12). We do linear regression of the distribution of simulated points to describe the behavior of the fluid with respect to the thermal variations. Silicon and oxygen atoms diffuse more rapidly at lower densities in a direct linear relation with temperature.

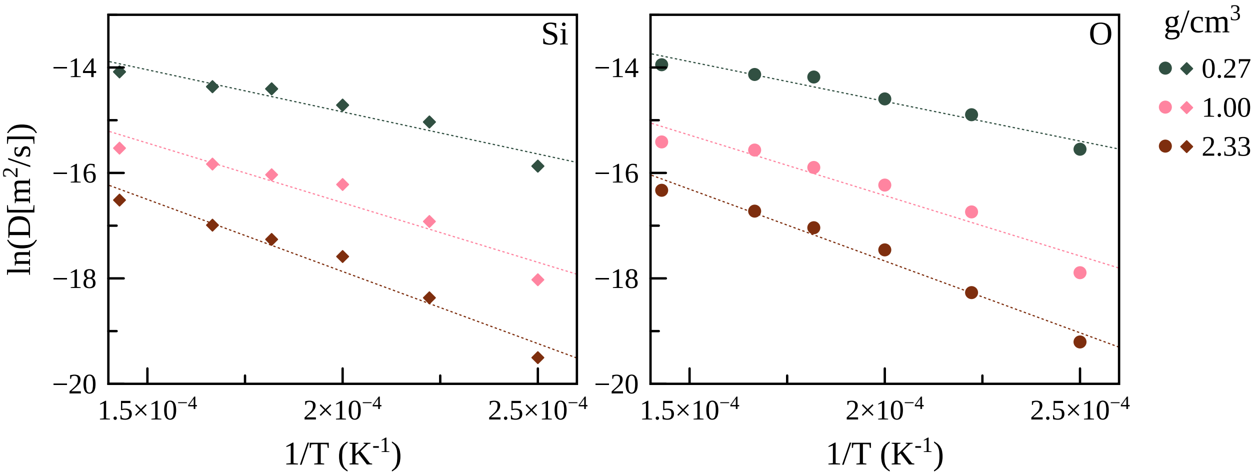

Figure 3.12: Diffusion coefficients of Si and O as a function of temperature at fixed densities. Left side panel shows coefficients for silicon at 2.33 g/cm^3 (brown), 1.00 g/cm^3 (pink) and 0.27 g/cm^3 (green). Right side panel shows coefficients for oxygens at same densities.

We describe the characteristic diffusion distance of silicon and oxygen atoms from the respective self-diffusion coefficients at each pressure-density-temperature condition by applying the equation below:

$$x = \sqrt{2D * t} \tag{3.1}$$

where x is the distance given in meters, D is the self-diffusion coefficient and t is time. We evaluate transport of atoms through time at four different frames: 100yrs, 100 kyr, 100 Myr and 1Gyr. We present results obtained from solving the characteristic diffusion distance equation as a function of self-diffusion coefficient, as shown in Figure 3.13. The comparison of four time-intervals concerns the potential magnitude of time scales implicated in the formation of the Moon and further rocky bodies of the Solar System for comparison purposes. Different lunar formation models consider different duration of accretion, retraction of the disk and posterior equilibration, where these periods could vary from a day (Canup, 2012), tens of years (Lock et al., 2018) to thousands of years (Pahlevan and Stevenson, 2007). Charnoz and Michaut (2015) proposed that the complete accretion of the Moon happened in a period between 10 to 10^4 years, where the temperatures varied between 5000 and 10000 K in the first 10 years. Duration of lunar magma ocean (LMO) with the persistence of elevated temperatures could also vary from 1 to several millions of years (Lock et al., 2020) and magma oceans throughout the Solar System are reported to persist up to 100 Myr (Elkins-Tanton, 2012). Accretion of planets, core formation of planetary bodies and formation of primary crusts in the Solar system also would follow the latter timescale (Chambers, 2001; Solomatov, 2007; Taylor and McLennan, 2009). However, the condensation of first solids would be in the order of a few million years and posterior processes involved in the geological evolution of the Earth could reach up to 1 Gyr.

The distance travelled by atoms depend on their self-diffusion coefficient, which is directly associated with the density of the system, where particles within a denser state tend to travel slower than particles on a more decompress system. As a matter of comparison, we point out the variation of distances with densities of 2.33 g/cm^3 and 0.27 g/cm^3 and we present summarized results in Table 3.1. In a 100 yr interval, when accretion and retraction of the disk in most lunar forming scenarios would be completed, silicon particles could reach between 4.62 and 35.8 m at 4000 K and between 20.6 and 69.5 m at 7000 K. However, transport of oxygen atoms is faster than silicon, and these particles could travel distances from 5.36 to 39.9 m at 4000 K and from 22.6 to 74.3 m at 7000 K.

Table 3.1: Characteristic diffusion distances travelled of silicon and oxygen atoms in different time intervals at 4000 and 7000 K. Values referring to 2.33 g/cm^3 simulations are indicated by x_{min} and values referring to 0.27 g/cm^3 simulations are given as x_{max}. Distances are given in meters.

Time (years)	4000 K				7000 K			
	Silicon		Oxygen		Silicon		Oxygen	
	x_{min}	x_{max}	x_{min}	x_{max}	x_{min}	x_{max}	x_{min}	x_{max}
100	4.62E+00	3.58E+01	5.36E+00	3.99E+01	2.06E+01	6.95E+01	2.26E+01	7.43E+01
100k	1.46E+02	1.13E+03	1.70E+02	1.26E+03	6.51E+02	2.20E+03	7.15E+02	2.35E+03
100M	4.62E+03	3.58E+04	5.36E+03	3.99E+04	2.06E+04	6.95E+04	2.26E+04	7.43E+04
1G	1.46E+04	1.13E+05	1.70E+04	1.26E+05	6.51E+04	2.20E+05	7.15E+04	2.35E+05

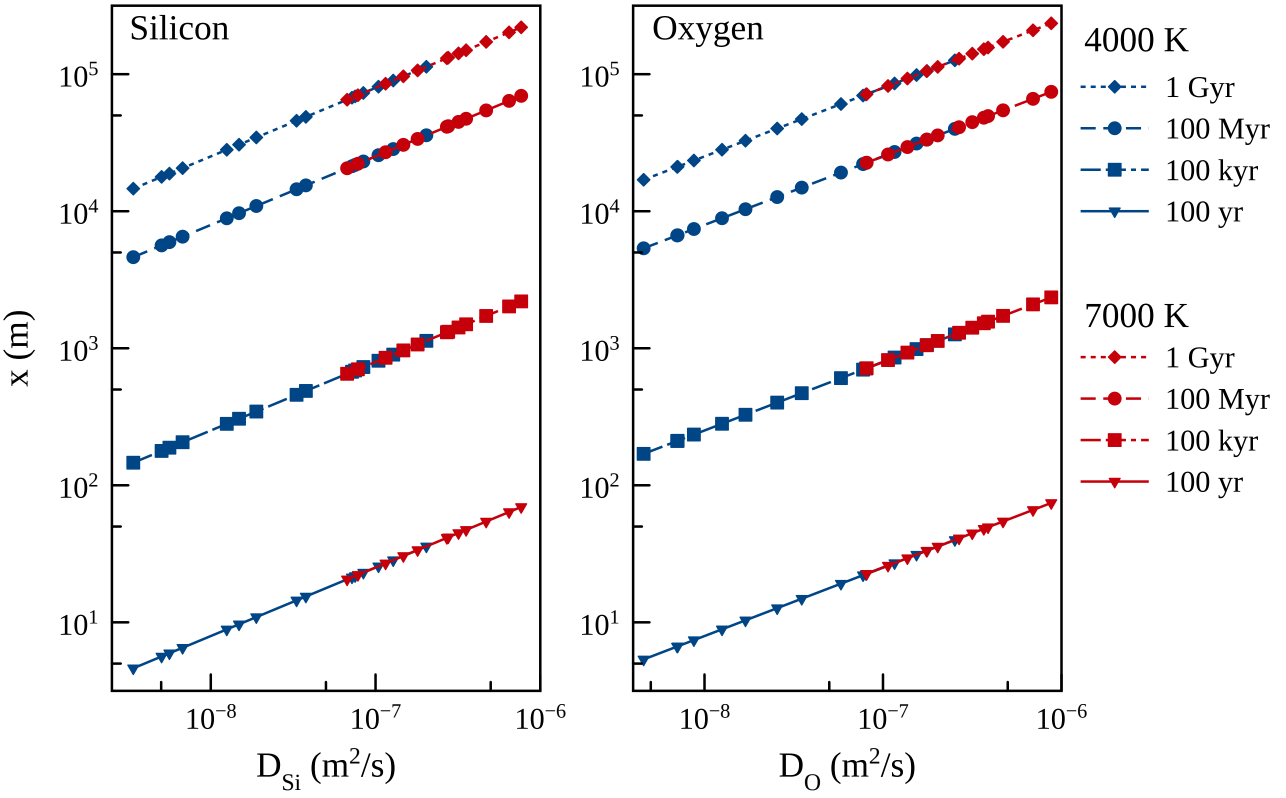

Figure 3.13: Displacement of atoms over time. Characteristic diffusion distance as a function of self-diffusion coefficients. Silicon distances are shown on the left-side and oxygen distances are shown on the right-side. Comparison between displacements at 4000 (blue) and 7000 K (red) in different time intervals.

Chapter 4

Hydrate silicate systems

Contents

4.1 Introduction

We studied four hydrated systems where the concentration of water increases from 3.61 to 23.07 wt%. The general chemical formulation of each of these systems can be written as: $9H_2O.72SiO_2$, $18H_2O.72SiO_2$, $36H_2O.72SiO_2$ and $72H_2O.72SiO_2$. The supercells are built from an initial pure SiO_2 supercell, where H_2O molecules were incrementally added, as detailed on Chapter 2. Following the same method applied for silica simulations, we varied temperature and cell volume in order to construct the respective equations of state of each of the aforementioned systems. The choice of the temperature for each composition was based on assumptions made with respect to the effects of the water concentration onto the general thermodynamic behavior. Therefore, we privileged higher temperatures for $9H_2O.72SiO_2$ and $18H_2O.72SiO_2$, and lower temperatures for $36H_2O.72SiO_2$ and $72H_2O.72SiO_2$. Each individual composition was simulated at three different nominal values of temperature and at ten or more density points. With respect to the density, we started with an intermediate value and then explored further lower and higher density states in order to sample liquid and gas domains.

The construction of the equation of state and location of the critical point follow the same principles applied for pure silica calculations. However, due to a limited number of simulation points on the gas phase region, the location of the gas spinodal is undefined. The low constraint of the third-order polynomial fit in such region does not allow a reliable equivalence between first-order derivative and the spinodal point, which prevents us from establishing accurate critical points for hydrated system. Nevertheless, the presence of liquid spinodals and the general assessment of fluid behavior allowed us to estimate a critical boundary based on temperature where, below such boundary, the system is in liquid-gas phase and, above this boundary, it is in supercritical state.

Structural properties were studied following the same methodology described on Chapter 2. We present results on pair distribution functions and coordination number analysis. The study on the polymerization of hydrated system is also presented, but demonstrated values are normalized due to the addition of oxygen atoms present in water molecules. Transport properties are calculated from mean square displacements and shown as diffusion coefficient values. Results of static and dynamic properties are frequently compared with pure SiO_2 data and the values of thermodynamic variables, polymerization, mean square displacement and diffusion coefficients can be found on Appendix B, D, E and F.2, respectively.

4.2 Equations of state

With the average pressure obtained from our calculations, we construct equations of state of four individual hydrated systems: $9H_2O.72SiO_2$, $18H_2O.72SiO_2$, $36H_2O.72SiO_2$ and $72H_2O.72SiO_2$. The results are presented in a pressure-density-temperature diagram where each composition comprises three different temperatures. Figure 4.1 shows the equations of state of each system, with individual panels representing results of a single composition at their varying temperatures and densities, as indicated on the top of each panel. Circles represent simulated conditions and dashed lines indicate third-order polynomial fits. As mentioned on the previous section, the positioning of gas spinodals is undefined, limiting the retrieval of information concerning the critical point location.

On the top left panel we show isotherms of $9H_2O.72SiO_2$ at 3000, 4000 and 5000 K, where densities varied from 0.34 up to 1.82 g/cm^3 and pressure varies from -0.58 to 1.74 GPa. Fitted curves at 3000 and 4000 K show a local minimum value of pressure around 1.2 to 1.3 g/cm^3, which indicates the preferential positioning for the liquid spinodal on both isotherms. However, at 5000 K, we observe a monotonical descent of the curve, suggesting that liquid and gas phases are undistinguishable. Such behavior indicates, therefore, that the system is in supercritical state. On the top right panel we can observe a similar behavior for $18H_2O.72SiO_2$ simulations. The polynomial fits of isotherms at 3000 and 4000 K show a local minimum value around 1.6 to 1.8 g/cm^3, which indicates the probable location of the liquid spinodal. At 5000 K, the fluid presents the same behavior as in the system previously described, where the absence of spinodals indicate the supercritical character of the system.

Bottom panels show the two compositions of hydrated silica with the largest concentrations of water. On the left side, we display results obtained from $36H_2O.72SiO_2$ calculations. Pressure-density values are indicated for temperatures at 2000, 3000 and 4000 K. Here, fitted curves at 2000 and 3000 K show a local minimum around 1.00 g/cm^3 and, therefore, liquid and gas are present at such temperatures. However, at 4000 K the continuous descent of the curve suggests that these phases cannot be separated anymore, meaning that the system is in supercritical state. The bottom right panel shows results calculated from $72H_2O.72SiO_2$ simulations.

On this system, we have the highest concentration of water of our dataset and it is where we can observe the largest variation in the thermodynamic behavior with respect to pure SiO_2 and to the previous hydrated systems. We simulated three different temperatures: 2000, 3000 and 4000 K. This composition shows separation of liquid and gas phases only at 2000 K, where it was possible to establish both spinodal points. In this scenario, the gas spinodal is placed at 0.65 g/cm^3 and the liquid spinodal is at 0.79 g/cm^3. Given that there is no temperature simulated below 2000 K that could assist on the construction of a reliable phase diagram for this system, the critical point was not placed. However, the system shows supercritical behavior at temperatures of 3000 and 4000 K.

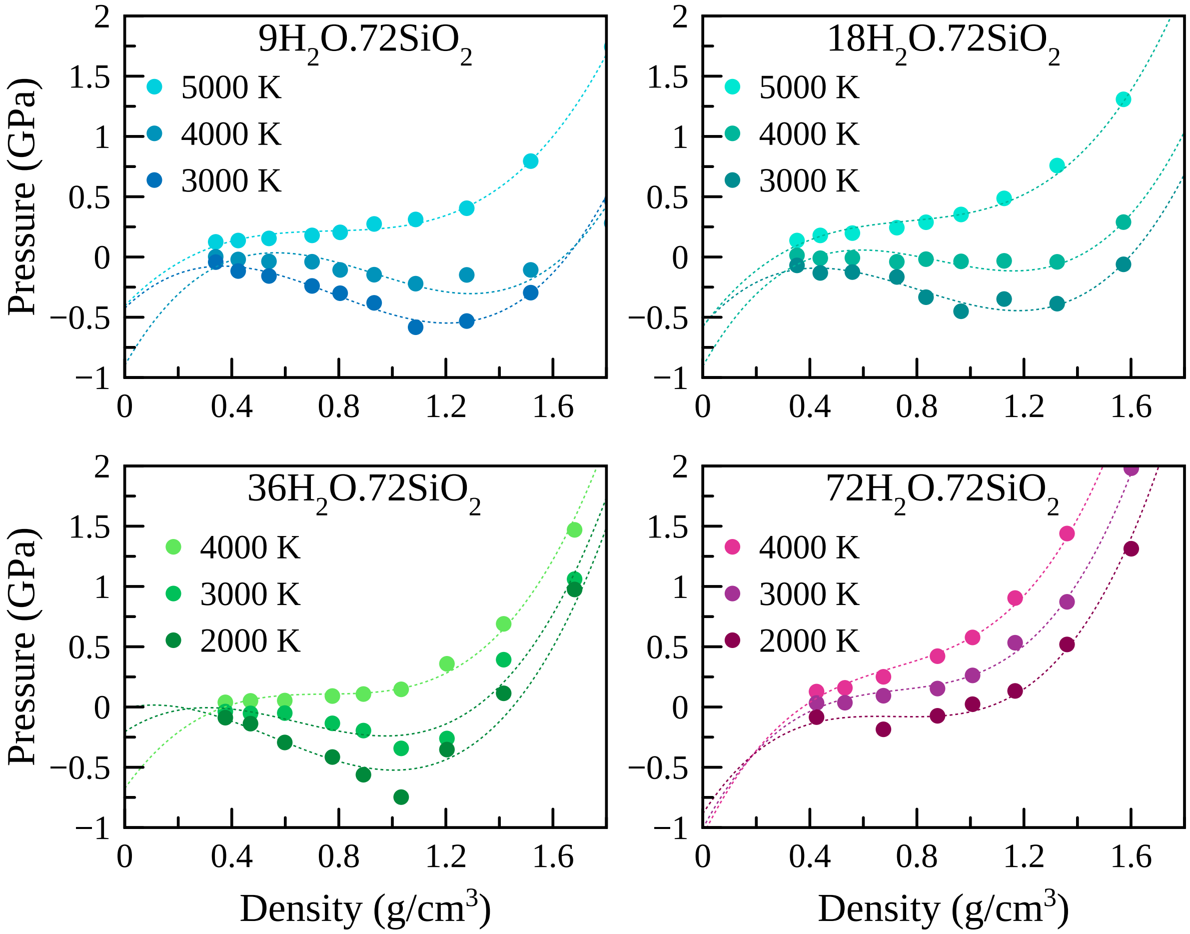

Figure 4.1: Equations of state of four hydrated silicate systems. Circles represent the pressure values computed from our simulations at fixed density and temperature. Dashed-lines represent the third-order polynomial fits that describe the behavior of each composition. Upper left panel: $9H_2O.72SiO_2$ at temperatures of 3000, 4000 and 5000 K. Upper right panel: $18H_2O.72SiO_2$ at temperatures of 3000, 4000 and 5000 K. Lower left panel: $36H_2O.72SiO_2$ at temperatures of 2000, 3000 and 4000 K. Lower right panel: $72H_2O.72SiO_2$ at temperatures of 2000, 3000 and 4000 K.

In order to assess the sole effect of the augmentation in water concentration onto thermodynamic properties of the different systems, we compare isotherms of different compositions at equal temperatures, as shown in Figure 4.2. We present the results in four panels with fixed temperatures: 2000, 3000, 4000 and 5000 K. The upper left panel shows the equation of state of $36H_2O.72SiO_2$ (green) and $72H_2O.72SiO_2$ (pink) at 2000 K. On the upper right panel, we show isotherms of every hydrated composition at 3000 K, where blue is $9H_2O.72SiO_2$ and dark green is $18H_2O.72SiO_2$. The lower left panel shows equations of state of anhydrous and hydrated systems at 4000 K, where dark blue represents pure SiO_2 simulation points. On the lower right panel we present isotherms at 5000 K of pure SiO_2 in green, $9H_2O.72SiO_2$ in blue and $18H_2O.72SiO_2$ in light blue.

It is possible to observe that systems with similar density at same temperature display an increase in pressure values with increasing water concentration. We highlight the diagram displaying 4000 K isotherms in the bottom left panel of Figure 4.2, where all five compositions simulated in this present study are compared. Here, it becomes evident the effect of water in the phase state of the various systems by the gradual displacement of spinodal points and increase in pressure. The change in the limit of stability of the phases suggests that systems are in different states at similar temperature-density conditions. For instance, if we consider densities around 1.5 g/cm^3 at 4000 K, pure SiO_2 is inside gas domain, whereas $18H_2O.72SiO_2$ is inside the liquid-gas coexistence dome. At this same conditions, an increase in water contents can drive the system to supercritical conditions, as demonstrate by the behavior of $36H_2O.72SiO_2$ and $72H_2O.72SiO_2$.

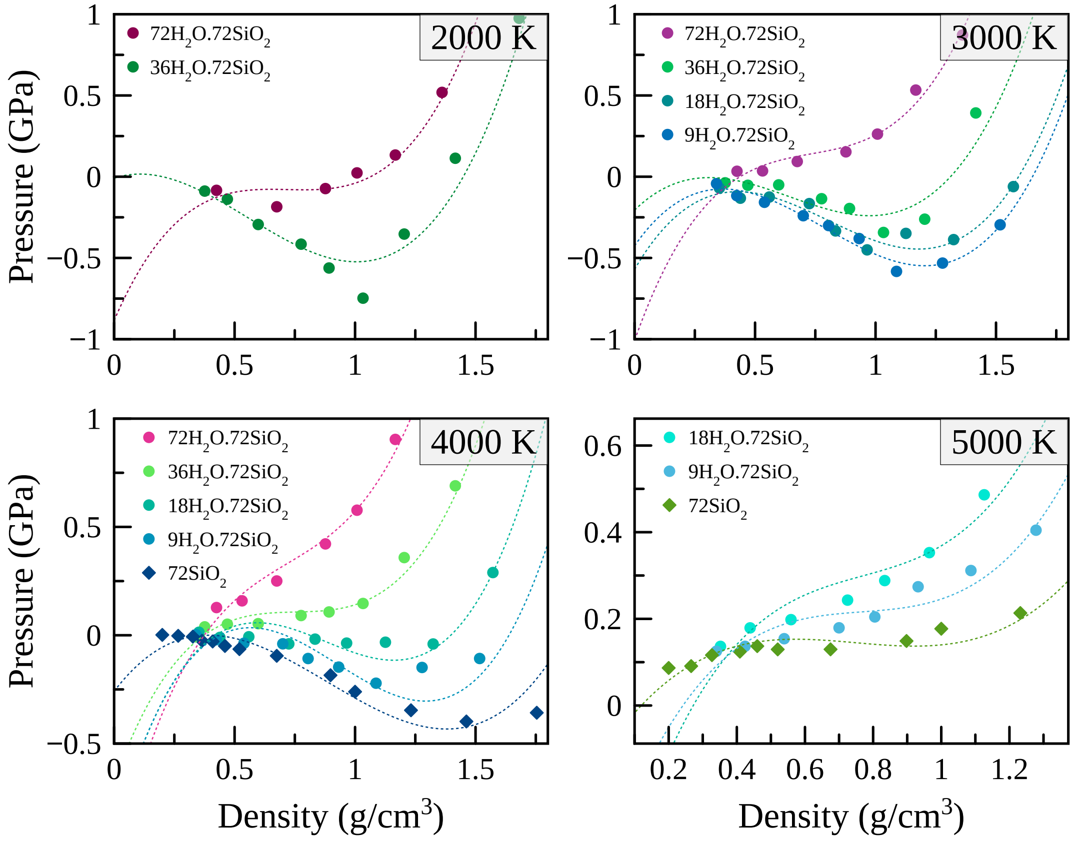

Figure 4.2: Comparison between pressure-density trends at same nominal temperatures with respect to the concentration of H_2O in the system. Circles represent simulation points and dashed-lines represent third-order polynomial fits.

4.3 Influence of water on the critical point of SiO_2

On the previous section we were able to observe the variation in the physicochemical behavior of the various systems by the change in the aspect of equations of state. Although we cannot establish a reliable phase diagram for hydrated compositions, we outline a critical boundary limit based on the thermodynamic data gathered in this work in a diagram relating temperature as a function of water concentration in wt%, as shown in Figure 4.3.

We start by placing the critical point of water, as reported in the literature (Wagner and Pruß, 2002), at 647 K and 100 wt% H_2O. We, then, place the critical point of pure SiO_2 at 5250 K and 0 wt% H_2O, as calculated in this work. The choice of the temperature was based on a mean value between upper (5500 K) and lower (5000 K) constraints. These two points mark the supercritical limit for pure H_2O and pure SiO_2 systems and are represented as purple diamonds on Figure 4.3. We continue by adding the information concerning silica simulations phases at 5000, 4500 and 4500 K. At such conditions, SiO_2 is in liquid-gas regime and is, therefore, represented by black crosses.

We proceed with the analysis of the phase state of each one of the SiO_2-H_2O intermediary compositions. From the analysis of the respective equations of state, we estimate the phase of each system at the calculated temperatures. As previously discussed, the presence of spinodal points in a equation of state indicates that the material is in the liquid-gas regime, whereas the absence of such points leads to the assumption that the same material is now in the supercritical regime. We observe that simulations on $9H_2O.72SiO_2$ at 3000 and 4000 K present the local minima and maxima indicative of the spinodal points. The same pattern is exhibit by $18H_2O.72SiO_2$ at 3000 and 4000K, $36H_2O.72SiO_2$ at 2000 and 3000 K, and $72H_2O.72SiO_2$ at 2000 K. At these conditions, the aforementioned setups are in the liquid-gas region and are, therefore, represented as black crosses on Figure 4.3. Simulations at 5000 K on $9H_2O.72SiO_2$ and $18H_2O.72SiO_2$, 4000 K on $36H_2O.72SiO_2$ and 3000 K on$72H_2O.72SiO_2$ showed a distinct behavior, where the monotonical descent of equations of state curves indicate that these materials are in the supercritical state at such conditions. We represent these fluids in supercritical regime as green squares.

By knowing the physical states of our systems, we are now able to estimate a boundary where we are likely to find the critical limit of all silicate systems containing from 0 to 100 wt% of H_2O. The purple dashed curve on Figure 4.3 connects the two known critical points and sets such limit of critical behavior. The gray area below this curve illustrates subcritical states, where systems are inside liquid-gas domain. Above the trendline, all fluids are in the supercritical state.

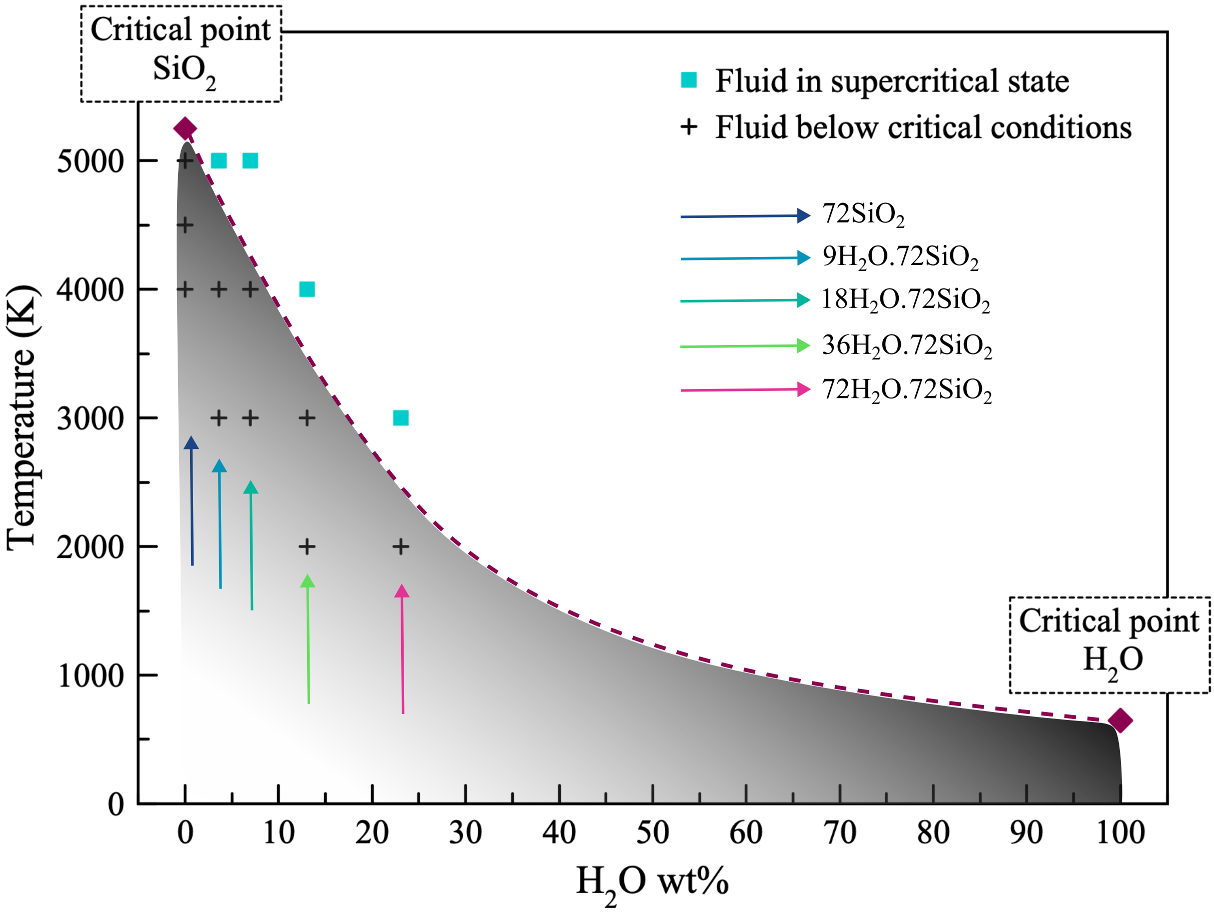

Figure 4.3: The critical point of SiO_2 and the critical point of H_2O (Wagner and Pruß, 2002): trend of supercritical state between pure SiO_2 and pure H_2O with respect to the concentration of H_2O in the silicatic system. The critical points are represented with purple diamond symbols; green squares represent simulations manifesting supercritical behavior; black crosses represent simulations where spinodals are present. The green filled squares indicates compositions where the fluid would be found below critical conditions. Colored arrows indicate points related to each individual composition.

4.4 Structural properties variations

From the same standpoint as applied for anhydrous simulations, we study the structural properties of the hydrated systems. We describe the behavior of each individual composition in terms of pair distribution functions, coordination numbers and polymerization analysis. Because we want to assess the influence of the presence of water into the system, we compare systems within similar quantities. For instance, in the following sections of this thesis, we are going to compare the different responses of each composition at the same simulated temperature (i.e. 4000 K) and/or at similar densities.

4.4.1 Pair distribution functions

The fluid structure of $9H_2O.72SiO_2$, $18H_2O.72SiO_2$, $36H_2O.72SiO_2$ and $72H_2O.72SiO_2$ is studied in terms of interatomic distances of oxygen-oxygen pairs at a nominal temperature of 4000 K. According to our calculations, at this temperature, systems containing 9 and 18 molecules of water are in the liquid-gas regime region, whereas systems with 36 and 72 water units are in the supercritical state. We individually represent and analyze pair distribution functions of each of the aforementioned compositions and then compare the observed behaviors in order to establish potential composition-property relational patterns. We compute PDF values at all densities and present the results as a function of radial distance in angstroms, as presented in Figure 4.4. Each panel illustrate a single composition, where upper left panel (a) shows $9H_2O.72SiO_2$, upper right panel (b) shows $18H_2O.72SiO_2$, lower left panel (c) shows $36H_2O.72SiO_2$ and lower right panel (d) shows $72H_2O.72SiO_2$.

In a global analysis of the four systems, the nearest neighbors represented in the first coordination sphere vary between 1.825 and 3.78 Å and indicate the distancing of oxygen atoms present in silica tetrahedra. Similar to the behavior observed in dry compositions, as the packing of the fluid structure becomes looser with the decrease in density, PDF peaks become wider, consistent with dissociation and vaporization of the fluid. Furthermore, distancing of atoms on tetrahedra can vary according to the density, where dense packing can force atoms to be closer and lead to a shift to the left of the peak, as clearly observed and exemplified on $72H_2O.72SiO_2$ 2.77 g/cm^3 (Figure 4.4d). We also observe the placement of the first minimum above zero, evidencing an increased dynamism of the particles (Green et al., 2018), reaching its maximum at lowest densities.

As mentioned on Section 3.2.1, the initial portion of the pair distribution function plot reflects the repulsive forces acting between atoms. As we reach radial distances of 1 Å, we start to observe the typical peaks of diatomic oxygen, shown in detail on inserted plots of Figure 4.4. Overall, the presence of O2 is stronger at low densities, when lower pressures favor dissociation, and less present at higher densities, where it tends to stay in tetrahedra. Diatomic oxygen peak on $9H_2O.72SiO_2$ vary from 1.085 to 1.475 Å at 0.34 g/cm^3, which represents the widest range of bond distance for the dioxygen pair in this system. Peaks present at 0.42 and 0.54 g/cm^3 are less wider and expressive. The $18H_2O.72SiO_2$ simulations follow the same trend as the aforementioned composition, where peaks can vary between 1.065 to 1.535 Å. Considering $36H_2O.72SiO_2$ and $72H_2O.72SiO_2$, variations on peak width is less significant, where they can vary from 1.075 to 1.475 at 0.78 g/cm^3 for a system with 36 water molecules and from 1.075 to 1.575 Å at 0.43 g/cm^3 on a system with 72 water molecules. With respect to the prominence of O_2 distributions studied in this analysis, we observe an inverse relation between the presence of molecular oxygen and the concentration of water in the system, meaning that dissociation of O_2 molecules into the vapor is less frequent when quantities of water are sufficiently high. Given that we observe a steady decrease of O_2 following the trend of water concentration, we cannot associate this variation to any phase transition (i.e. liquid-vapor-supercritical), but only to the effect of H_2O.

4.4.2 Coordination numbers

Here in the following section we assess the fluid organization by evaluating the structure of the atomic pair. We calculate the fraction of coordinated Si-O at each density on every system, dry and wet, at 4000 K and show the results on Figure 4.5. Different colors represent different compositions, where dark blue is SiO_2, light blue is $9H_2O.72SiO_2$, dark green is $18H_2O.72SiO_2$, light green is $36H_2O.72SiO_2$ and pink is $72H_2O.72SiO_2$. Given that densities among compo-

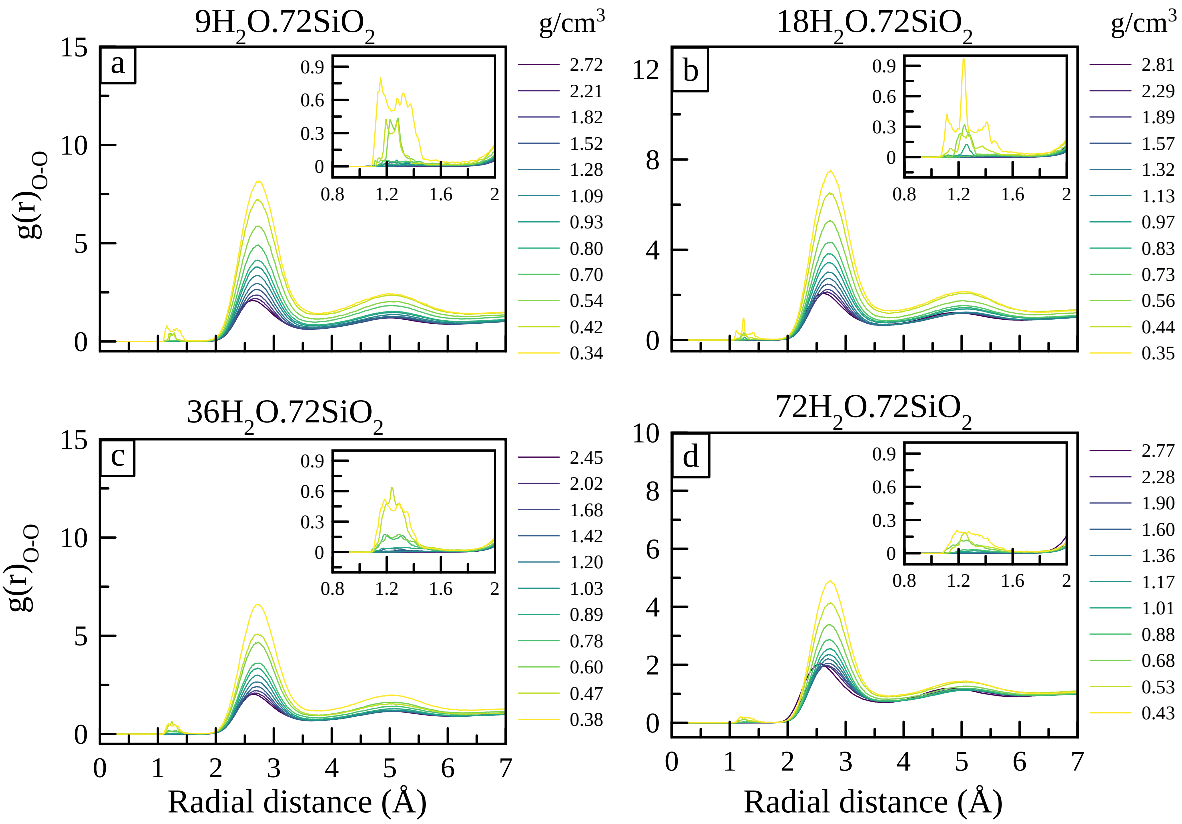

Figure 4.4: Pair distribution functions of oxygen-oxygen pairs at 4000 K for all hydrated systems. a) $9H_2O.72SiO_2$; b) $18H_2O.72SiO_2$; c) $36H_2O.72SiO_2$; d) $72H_2O.72SiO_2$. Inserted panels show in detail the distribution between 0.8 and 2 Å indicating the presence of O_2 molecules.

sitions hardly overlap, we chose to compare results within two distinct sets of values: a lower density that varies between 0.35 to 0.43 g/cm^3 and represented by squared symbols, and a higher density varying from 0.93 to 1.03 g/cm^3, represented by circles.

The comparison of coordination number showed little to no deviations as a direct response to variations in composition. It is important to remark that SiO_2, $9H_2O.72SiO_2$ and $18H_2O.72SiO_2$ are in liquid-vapor domain, whereas $36H_2O.72SiO_2$ and $72H_2O.72SiO_2$ are in supercritical regime at 4000 K. The previous analysis of anhydrous silica discussed on Section 3.2.2 showed a correlation between thermodynamic properties and the structure of the fluid. However, within the conditions presented on Figure 4.5, it is not possible to observe such correlation, where the increase in dissociation is marked by an augmentation of lower coordination numbers towards vapor and supercritical states.

Nevertheless, hydrogen atoms can react with silica to form orthosilicic acid molecules, where the general formula is $Si(OH)_4$. The presence of such molecule was observed in a $36H_2O.72SiO_2$ simulation at 4000 K and 1.03 g/cm^3, as shown in Figure 4.6. Its presence in other systems as well as its quantification need to be further investigated. Considering the structure of the Si-O pair in a system rich in $Si(OH)_4$, the prevailing coordination number is still 4, given that four oxygen atoms are coordinated around one silicon. However, the Si-O-H organization has an impact over the polymerization of the fluid due to a network break of silica.

This fact is corroborated by the behavior observed regarding O-Si coordinations. On Figure 4.7 we show five panels with the calculated fraction of O-Si coordination number distributions at every density of anhydrous and hydrated simulations at 4000 K. Here we can observe a gradual increase in the dissociation of the fluid, marked by an increase in coordination 1 in a direct relation with the decrease in density and the increase in water concentration.

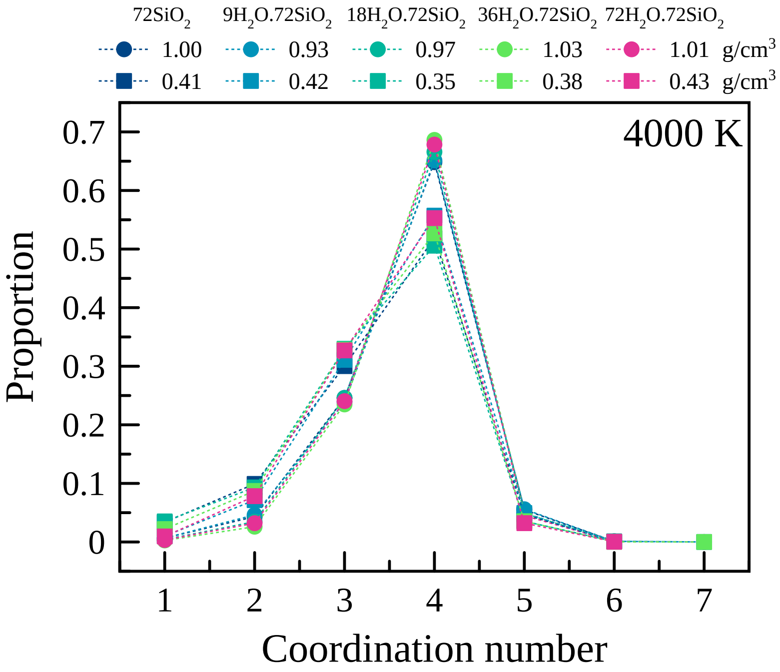

Figure 4.5: Comparison of coordination number proportions of Si-O in anhydrous and hydrated systems at 4000 K at similar densities. Circles represent values for densities between 0.93 and 1.03 g/cm^3 and squares represent values for densities between 0.35 and 0.43 g/cm^3. Each color indicates one individual system, where dark blue is pure SiO_2, light blue is $9H_2O.72SiO_2$, dark green is $18H_2O.72SiO_2$, light green is $36H_2O.72SiO_2$ and pink is $72H_2O.72SiO_2$.

4.4.3 Polymerization

The presence of water can affect polymerization structure by liberation of orthosilicic acid, as demonstrated on the previous section. The mechanisms involved in this process are not going to be detailed in this work, instead our focus is in quantifying the extent of depolymerization on various hydrated fluids.

As detailed on Section 3.8, we calculate the degree of polymerization by estimation of the variable V_{total}. It gives the relation between coordination fractions of silicon with respect to oxygen atoms ($Si\text{-}O_x$) over coordination fractions of oxygen with respect to silicon ($O\text{-}Si_y$). However, in the case of hydrated compositions, the additional oxygen atoms introduced in different proportions into the systems require that a factor of correction is added into the equation. Thus, we normalize V_{total} for the number of oxygens contained in each individual system, defining Vn_{total}. Here, polymerization values vary between 0.011 and 0.014, where 0.011 indicates a depolymerized system and 0.014 indicates a fully polymerized one. A table with discrete values of Si-Ox, O-Siy and Vn_{total} is given on Appendix D.2.

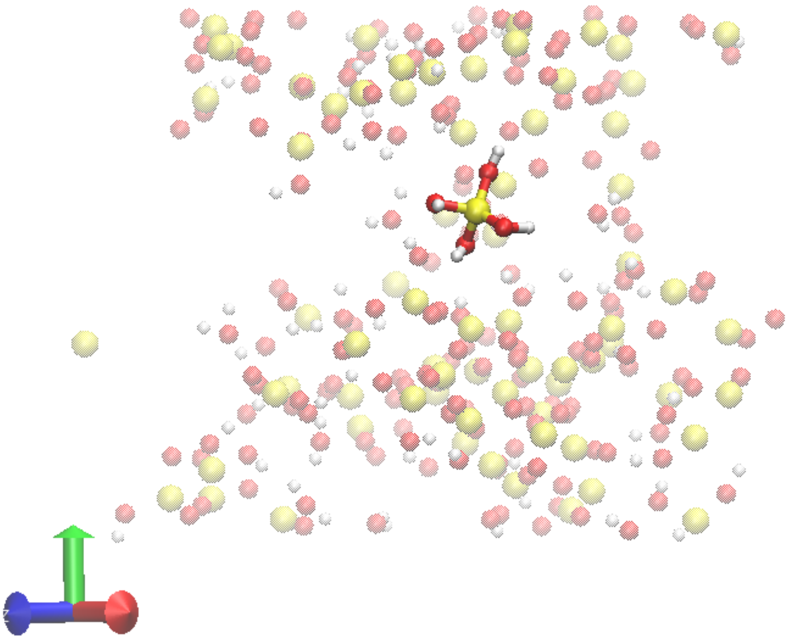

Figure 4.6: Orthosilicic acid molecule spotted in a simulation of $36H_2O.72SiO_2$ at 1.03 g/cm^3 and 4000 K. Spheres represent individual atoms, where yellow is silicon, red is oxygen and white is hydrogen.

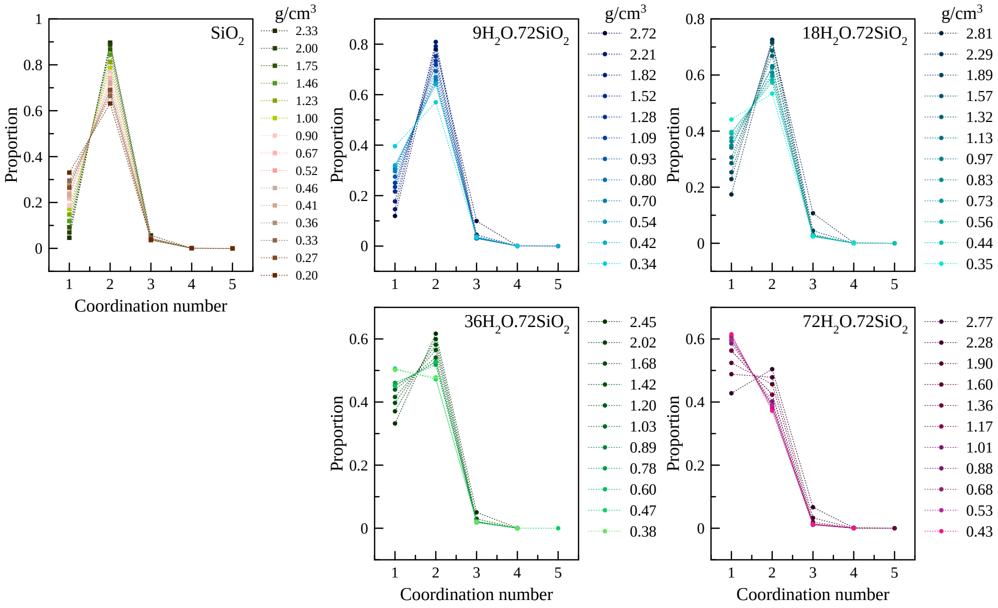

Figure 4.7: Distribution of O-Si coordinations in anhydrous and hydrated systems at 4000 K at all simulated densities. Each panel shows an individual composition: SiO_2 on the top left, $9H_2O.72SiO_2$ on the top middle, $18H_2O.72SiO_2$ on the top right, $36H_2O.72SiO_2$ on the bottom middle and $72H_2O.72SiO_2$ on the bottom right of the figure.

We compare deviations on polymerization behaviors of SiO_2, $9H_2O.72SiO_2$, $18H_2O.72SiO_2$, $36H_2O.72SiO_2$ and $72H_2O.72SiO_2$ at 4000 K and present it as a function of density, as shown in Figure 4.8. Individual compositions are represented in different colors, where hydrated fluids are indicated as circles and pure SiO_2 is indicated as squares. The dashed-line marks the estimation of the critical limit, where compositions above are in liquid-vapor phases and compositions below are in the supercritical regime. Phase domains are separated based on equations of state presented on Section 3.2.3 and are shown as gray filled areas.

Similar to the patterns observed in pure silica simulations, hydrated compositions show a decrease in calculated polymerization values with density decrease. In comparison, the variations observed here are less homogeneous than those observed in anhydrous systems. Such behavior cannot be linked to any of the studied properties so far and needs further investigation.

We also observe that Vn_{total} values are overall smaller as water concentration increases. Furthermore, high density states containing water already show a considerable degree of depolymerization. Such fact is presumably due to the formation of orthosilicic acid by hydrolysis of Si-O-Si network bonds. Considering only values for densities above 2 g/cm^3, it is possible to observe a dramatic decrease in polymerization from SiO_2 to $72H_2O.72SiO_2$ values.

Above the supercritical line three systems are present: SiO_2, $9H_2O.72SiO_2$ and $18H_2O.72SiO_2$. Inside the liquid domain, these systems present an almost linear behavior. Towards the coexistence and the gas domain, such behavior becomes more erratic, where the dissociation of $9H_2O.72SiO_2$ can be found to be locally more intense than SiO_2. Below the supercritical boundary line, we observe an important gap between $36H_2O.72SiO_2$ and $72H_2O.72SiO_2$, meaning that the system is highly dissociated in the latter.

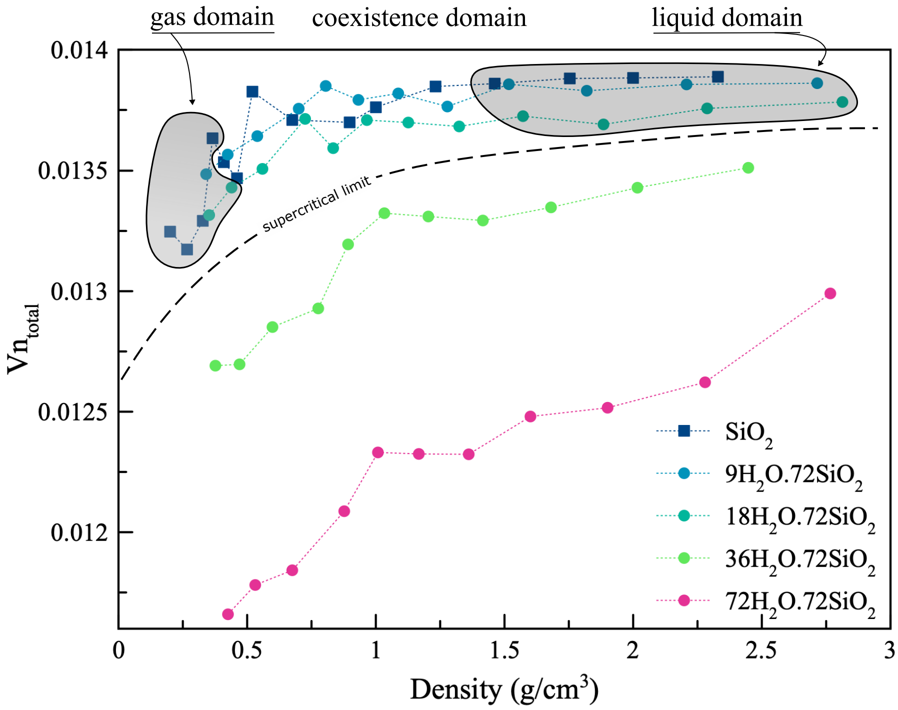

Figure 4.8: Polymerization analysis of pure SiO_2 and hydrated systems at 4000 K. The Vn_{total} value is the V_{total} value normalized by the number of oxygens in each system.

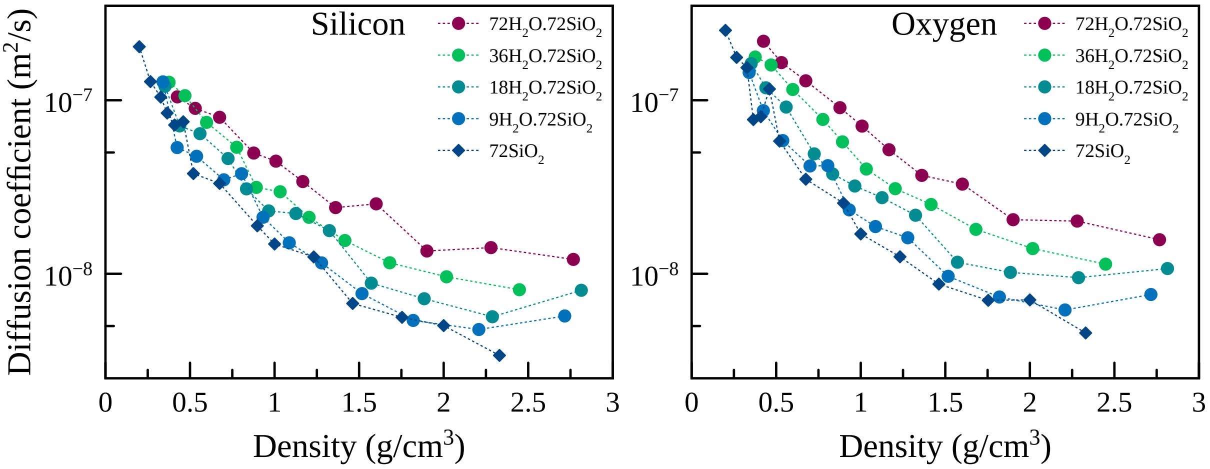

Figure 4.9: Comparison of diffusion coefficients of all simulated systems at 4000 K. Circles represent hydrated system and diamond symbols represent anhydrous silica.

4.5 Transport properties variations

The presence of water influences not only the thermodynamics, but also transport properties. Diffusion coefficients were calculated for hydrated compositions following the same principles applied for anhydrous systems. Discrete values of the bulk hydrated dataset at all temperatures are presented in Appendix F.2 and F.3. We compare self-diffusion coefficients of silicon and oxygen at 4000 K for hydrated and anhydrous compositions. The mobility of the referred atoms increase together with the concentration of H_2O, as shown in Figure 4.9. This effect becomes more prominent at higher densities, where a vertical spread of the coefficients is observed, indicating a stronger influence of water at such conditions. At lower densities, this different becomes less significant and coefficients can overlap.

Analyzing the displacement of particles over time, we can also establish a correlation between the maximum distance travelled and the presence of water. In the presence of water, silicon and oxygen particles tend to travel longer distances with respect to dry environments. We see in Figure 4.10 the variation in the position of atoms as a function of the self-diffusion coefficient for silicon and oxygen at 4000 K of the dry silica system (blue) and $72H_2O.72SiO_2$ (pink) at different scales of time. We mark specific densities as a matter of comparison between systems in order to establish reference points which explicitly evidence the leap in travelled distances.

The lower limit of density simulated in this study for $72H_2O.72SiO_2$ is 0.43 g/cm^3, whereas for pure SiO_2 this limit would be 0.20 g/cm^3. Considering that low density states would implicate particles diffusing at a higher rate, we observe still a longer distance travelled by silicon in a dry system with respect to a wet system due to this density difference. Notwithstanding, the effects of water with respect to oxygen atoms at lower densities are more significant, evidenced by a larger gap between 1.00 g/cm^3 SiO_2 and 1.01 g/cm^3 $72H_2O.72SiO_2$, but also causing atoms at 0.43 g/cm^3 to travel similar distances as 0.20 g/cm^3 SiO_2.

Up to 100 years, silicon particles in a pure SiO_2 environment would be able to travel between 4.62 and 35.8 meters, whereas in a wet environment the distances could reach between 8.74 and 25.7 meters, depending on density conditions. Considering oxygen atoms, those distances would vary from 5.36 and 39.9 meters, and from 9.96 to 37.1 meters in a dry and wet system,

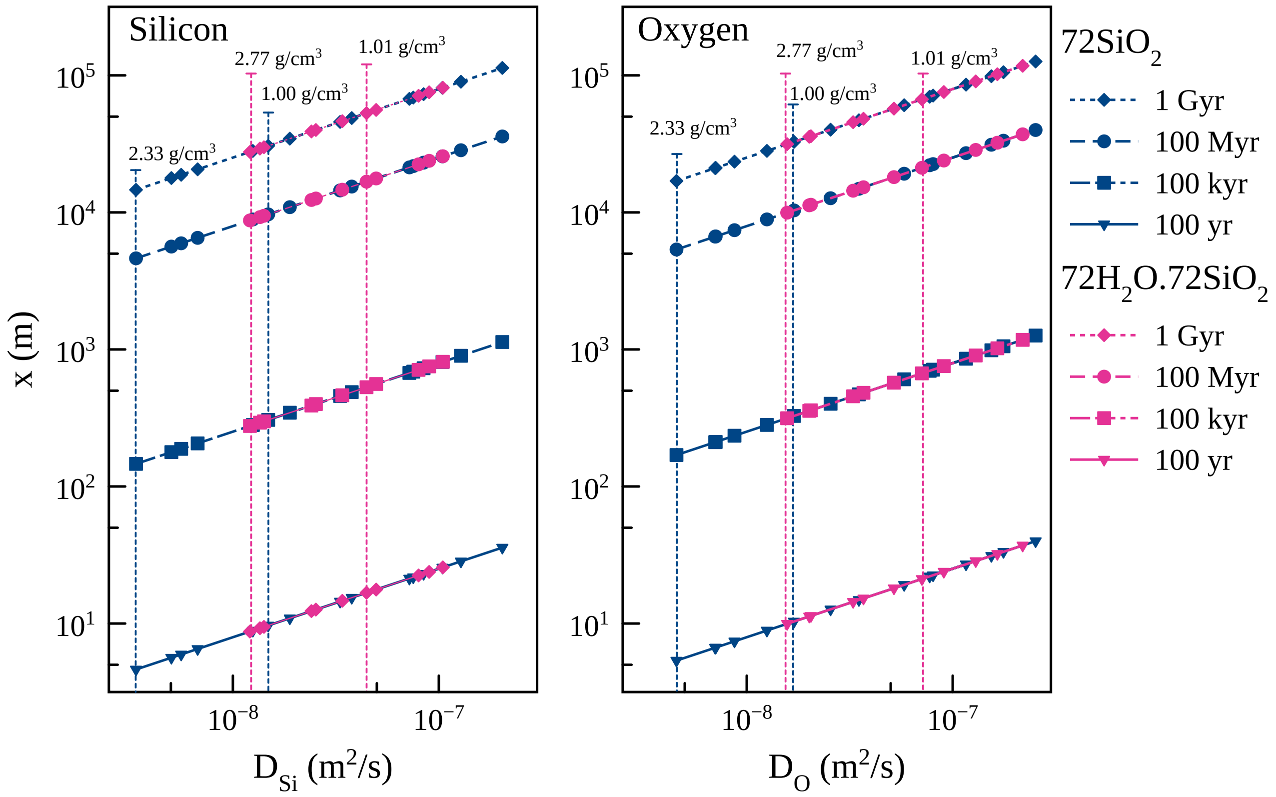

Figure 4.10: Displacement of silicon and oxygen in dry and wet systems atoms in four different intervals of time. The distance is presented as a function of the self-diffusion coefficients of each atom at given pressure-density conditions. Pure SiO_2 results are presented in blue and $72H_2O.72SiO_2$ results are presented in pink. Dashed lines mark the characteristic diffusion distance of specified densities within the same color code. Considered time scales are 100 yr, 100 kyr, 100 Myr and 1 Gyr.

respectively.

If we scale up to 100 Myr, silicon in pure SiO_2 could achieve distances between 4621.4 and 35823.7 meters, whereas oxygen could travel from 5363.2 to 39926.9 meters, also depending on the density of the system. Now regarding larger time scales, in 1 Gyr silicon particles could travel up to 30597.6 meters at 1.00 g/cm^3 in pure SiO_2 system and 53016.1 meters at 1.008 g/cm^3 in a $72H_2O.72SiO_2$ system, as for oxygen it could reach 32712.9 to 66896.1 meters, with respect to the same conditions. Discrete values of characteristic diffusion distances are presented in Table 4.1.

Table 4.1: Characteristic diffusion distances of silicon and oxygen of $72H_2O.72SiO_2$ at 4000 K. Values from simulations at 0.43 g/cm^3 are represented as x_{min}, whereas values from simulations at 2.77 g/cm^3 are indicated as x_{max}. Values are given in meters.

Time (years)	Silicon		Oxygen	
	x_{min}	x_{max}	x_{min}	x_{max}
100	8.74E+00	2.57E+01	9.96E+00	3.71E+01
100k	2.76E+02	8.12E+02	3.15E+02	1.17E+03
100M	8.74E+03	2.57E+04	9.96E+03	3.71E+04
1G	2.76E+04	8.12E+04	3.15E+04	1.17E+05

Chapter 5

Implications on lunar formation

5.1 Oxygen contents

Contents of oxygen in a particular environment are usually given in terms of its fugacity, which represents the effective pressure of the gas (Atkins et al., 2018). It has been reported that variation in oxygen fugacity can affect rock melting, speciation of volatile species during outgassing, composition of planetary atmosphere, valence ratio of transition metals in minerals and more (Lin et al., 2021). On terrestrial rocks, a variation between a Bowen trend and a Fenner trend can be observed as a result of oxygen abundance variation, where tholeiitic series are favored in reducing conditions and calc-alkaline series are a result of more oxidizing environments (France et al., 2010). Experiments reproducing solar system redox conditions revealed a changing in the positioning of the liquidus curve of basalt depending on oxygen abundance (Lin et al., 2021), suggesting that an increase in oxygen contents can decrease the temperature of rock melting.

Measurements of paleo redox environmental conditions can be assessed by the mineralogical assembly, stablished in a series of mineral buffers described in the literature (Lindsley, 1991). The oxygen fugacity of each buffer trend is given in a gradual variation as a function of temperature, where the magnetite-heamatite (MH) assembly indicates settings with the highest oxygen partial pressures and the quartz-iron-fayalite (QIF) assembly represents the lowest value, which is associated to reducing conditions. Although calculations aiming to study the chemistry of the protolunar disk showed more oxidizing conditions during lunar formation (Visscher and Fegley, 2013), mineral buffers and recent ab initio simulations favor a reducing environment for the Moon. Lunar mineral controls have been studied in terms of basalt and mantle compositions that bracket the redox state between IW (iron-wüstite) and IW-1 (Stolper, 1977; Shearer et al., 2004; Palme and O'Neill, 2014; Deng et al., 2020).

The concentration of molecular O_2 can be a proxy for temperature-pressure-density conditions under which the Moon condensed. In a reduced environment, the gas phase is dominated by species oxygen-poor and it is mostly formed by H_2 and CO molecules. Considering pair distribution function analysis on dry fluids presented on Section 3.2.1 of this work, such conditions could not be in place if the fluid is in supercritical state at temperatures above 5500 K, given the abundance of dioxygen in the system. The same principle can be used to assess possible density states, where the threshold is at 0.78 g/cm^3. Therefore, the lunar condensation must have happened in a disk region where temperatures were lower than 5500 K and densities were higher than 0.78 g/cm^3.

Assessment of the partial pressure of oxygen remain important to understand the composition and equilibration of phases in the protolunar disk, since it can alter the fractionation of species into the gas and ultimately impact mixing processes. Furthermore, assuming that concentration of molecular oxygen increases, so does the redox potential. In these conditions, O_2 will eventually be converted to H_2O through a couple of reactions and the energy release can raise disk entropy and favor mixing.

5.2 Equilibration in the protolunar disk

Equilibration is a key aspect on lunar forming scenarios. The impact between two objects with distinct compositions calls for a postimpact process responsible for mixing components and resulting in two isotopically homogeneous bodies. Mechanisms involved in this process can dictate the degree of mixing among phases and ultimately affect possible outcomes.

The amount of mass ejected into the disk after the impact is an important factor for disk equilibration and lunar accretion. It relates to the amount of energy transferred on impact and the thermodynamic properties of materials involved. Models applied for lunar forming scenarios simulations rely on equations of state to describe the behavior of such materials under varying conditions, where M-ANEOS is the most commonly used (Melosh, 2000). This equation of state improved the previous monoatomic representation of the gas phase into as gas composed of diatomic molecules. We demonstrate by our structural analysis that such assumption leads to a misrepresentation of the gas, since the dissociation of the fluid often happens in clusters containing more than two atoms. Because of that, the polyatomic character of the gas requires less energy for vaporization and affects its energetic barrier of formation, which can potentially increase the amount of gas in the disk (Canup, 2004) and relax constraints on size of impactor and energy involved.

Furthermore, silicate materials modeled in lunar forming scenarios often are described in terms of the equation of state of forsterite, which has a critical point estimated above 6000 K (Townsend et al., 2020). However, if we consider the nature of rock forming silicates with their respective critical points, as presented in Figure 3.2, together with the estimations of redox states during lunar formation and the O_2 availability at different temperatures, we limit temperatures protolunar disk temperatures in a dry scenario up to 5000 K. Considering hydrated scenarios, the lowering of critical temperatures allows systems to remain inside the supercritical regime, where mixing happens more easily, delaying the liquid-vapor fractionation and ultimately boosting chemical equilibration.

Chemical equilibration is also strongly impacted by the transfer of species among phases. Diffusion is the main mechanism involved in the transport away from the vapor-liquid boundary. Variation in the coefficients of diffusion can affect the rate on which particles move in their respective environments and, hence, favor or not equilibration. From our simulations, we were able to demonstrate how the increase in the temperature can improve diffusion on pure silicate systems. The decrease in density has a significant effect as well, where lesser dense states tend to diffuse faster. Such behavior is boosted by the presence of water. In a hydrated post-impact lunar debris disk, particles travel more rapidly with respect to anhydrous systems and, therefore, mixing and equilibration are again favored. It is worth to note that the duration of the protolunar disk can be critical for elemental distribution and equilibration, where the timescale on which diffusion happens will directly affect the atomic travelled length, both on anhydrous or hydrated phases.

Timescales of the protolunar disk have been associated with the viscosity of the fluid (Charnoz and Michaut, 2015). Abnormal viscous vapor can escape outwards or efficiently flow towards the surface of the Earth, leading to a significant disk mass loss. Because of that, cooling timescales at these conditions can be ten times shorter than those of non-viscous disks. Variations in the polymerization are known to affect the viscosity of fluids, where highly polymerized systems tend to present higher viscosity and will, therefore, contribute to a faster cooling. In opposition, depolymerized compositions show lower viscosity and will favor long lasting disks. The hydrolysis of silica with the formation of silicic acid break polymer networks and leads towards less viscous states.

Chapter 6

Conclusions

We simulated SiO_2 applying ab initio molecular dynamics methods over six different temperatures, from 4000 to 7000 K, in a density range from 0.2 g/cm^3 up to 2.33 g/cm^3, corresponding to pressures up to 8.5 GPa. This region corresponds to the liquid-vapor transition and critical point region. From our simulations, we successfully built a SiO_2 phase diagram delimitating the coexistence dome within the modeled conditions. We predicted the critical point at temperatures between 5000 and 5500 K, in a density range from 0.6 to 0.85 g/cm^3 and at a pressure interval of 0.15 to 0.25 GPa. We demonstrated that above 5500 K, SiO_2 is in supercritical state where no liquid-vapor separation is possible for this material. Given the protolunar disk temperature conditions, silica condense close to the photosphere of the disk and can rapidly re-vaporize as it descends to towards the midplane, depending on disk temperature profiles.

We also demonstrated that the dissociation of SiO_2 is more complex than established previously in current equations of state (Melosh, 2007). Molecular clusters from SiO_2 dissociation form different species with varying number of atoms, where O_2 is also present. The number of atoms in the molecules present in the gas depends largely on the temperature and it is dominantly diatomic only in the supercritical regime at 7000 K. The gas phase shows clusters with coordination numbers varying from 2 to 5, depending on pressure-temperature-density conditions, which suggests that the mass of the protolunar disk could be underestimate in current lunar forming scenarios simulated that employ smoothed-particles hydrodynamics methods.

In order to characterize the polymerization of the fluid, we developed and applied a new metric that allows us to assess the degree of dissociation in terms of the relation between Si-O and O-Si coordination numbers, which indicates the potential amount of overall bonding in the fluid. This method needs to be applied carefully and is still in need of further analysis. From the analysis of the diffusion coefficients of particles in the pure SiO_2 system, we established characteristic diffusion distances for silicon and oxygen between 4000 and 7000 K for both particle types. In the estimate timeframe of complete lunar accretion (100yr), we demonstrate that silicon particles can reach a maximum distance of 0.0051 m at 4000 K and 0.0124 m at 7000 K, and oxygen particles can travel distances up to 0.0071 m at 4000K and 0.0132 m at 7000 K.

We introduced water molecules in the SiO_2 system creating four hydrated systems, in a silica-water proportion of 8:1, 4:1, 2:1 and 1:1. We simulate each system at three different temperatures, varying between 2000 and 5000 K and construct phase diagrams of each individual hydrated system. We demonstrated a variation of the distribution of phases with respect to the content of water, ultimately decreasing the critical point temperature with increasing water concentration. Due to a limited number of simulation points in the gas region, the precise location of the respective critical points was not possible of being established for these systems. However, we have estimated a limit of stability of the supercritical fluid in relation to the temperature as a function of the concentration of water. Water affects the distribution of phases and can delay the vapor-liquid separation and, consequently, the partitioning of chemical species. The presence of water also influences the characteristic diffusion distances of elements and, together with variations in phase behaviors, it can increase the mobilization of materials.

Models of lunar formation consider a giant impact as the main genetic mechanism, where two main theories prevail: the canonical model and the fast-spinning Earth model. In both cases, the elemental distribution is not completely resolved since current methods cannot precisely describe the behavior of volatiles after impact, which leads to speculation concerning their final distribution. The volatile budget is not only a matter of partitioning into liquid and vapor phases, but also of how volatiles affect disk properties as liquid fractionation occurs. Furthermore, the development of more accurate equations of state is necessary to properly describe the dissociation of molecules that can alter the total final mass. Ultimately, the understanding of the behavior of the materials in post-impact conditions play a necessary role giving clues that lead to more accurate models. Our results show that current techniques employed in the search of an accurate model for lunar formation do not satisfy the complexity of the disk dynamics and still need improvements. Nevertheless, it is clear that the complexification of models with accurate variables seem to favor the canonical impact model proposed by Canup (2012).

Bibliography

Anders, E. and Grevesse, N. (1989). Abundances of the elements: Meteoritic and solar, *Geochimica et Cosmochimica Acta* **53**(1): 197–214. *https://www.sciencedirect.com/science/article/pii/001670378990286X*.

Andrew J. Whittle's Research Group at MIT, Multiscale modeling of clay-water systems (accessed: June 16th 2022, *https://ajw-group.mit.edu/multiscale-modeling-clays*). *https://ajw-group.mit.edu/multiscale-modeling-clays*.

Armytage, R., Georg, R., Williams, H. and Halliday, A. (2012). Silicon isotopes in lunar rocks: Implications for the moon's formation and the early history of the Earth, *Geochimica et Cosmochimica Acta* **77**: 504–514. *https://doi.org/10.1016/j.gca.2011.10.032*.

Asphaug, E. (2014). Impact origin of the moon?, *Annual Review of Earth and Planetary Sciences* **42**(1): 551–578. *https://doi.org/10.1146/annurev-earth-050212-124057*.

Atkins, P., De Paula, J. and Keeler, J. (2018). *Atkins' Physical Chemistry*, 11 edn, Oxford University Press, London, England.

Barr, A. C. (2016). On the origin of Earth's moon, *Journal of Geophysical Research: Planets* **121**(9): 1573–1601. *https://doi.org/10.1002/2016je005098*.

Baur, W. H. (1971). The prediction of bond length variations in Silicon-Oxygen bonds, *American Mineralogist* **56**(9-10): 1573–1599. *https://pubs.geoscienceworld.org/msa/ammin/article-pdf/56/9-10/1573/4250728/am-1971-1573.pdf*.

Baur, W. H. (1977). Silicon-Oxygen bond lengths, bridging angles Si-O-Si and synthetic low tridymite, *Acta Crystallographica Section B Structural Crystallography and Crystal Chemistry* **33**(8): 2615–2619. *https://doi.org/10.1107/s0567740877009029*.

Benz, W., Cameron, A. G. W. and Melosh, H. J. (1989). The origin of the moon and the single-impact hypothesis III, *Icarus* **81**(1): 113–131. *https://doi.org/10.1016/0019-1035(89)90129-2*.

Blöchl, P. E. (1994). Projector augmented-wave method, *Physical Review B* **50**(24): 17953–17979. *https://doi.org/10.1103/physrevb.50.17953*.

Boero, M. and Oshiyama, A. (2015). Car-parrinello molecular dynamics, *Encyclopedia of Nanotechnology*, Springer, pp. 1–10. *https://doi.org/10.1007/978-94-007-6178-0_100946-1*.

Born, M. and Oppenheimer, R. (1927). Zur quantentheorie der molekeln, *Annalen der Physik* **389**(20): 457–484. *https://doi.org/10.1002/andp.19273892002*.

Boss, A. P. (1998). Temperatures in protoplanetary disks, *Annual Review of Earth and Planetary Sciences* **26**(1): 53–80. *https://doi.org/10.1146/annurev.earth.26.1.53*.

Cameron, A. G. W. and Ward, W. R. (1976). The origin of the Moon, *Lunar and Planetary Science Conference*, Vol. 7, p. 120. *https://ui.adsabs.harvard.edu/abs/1976LPI.....7..120C*.

Cano, E. J., Sharp, Z. D. and Shearer, C. K. (2020). Distinct oxygen isotope compositions of the Earth and Moon, *Nature Geoscience* **13**(4): 270–274. *https://doi.org/10.1038/s41561-020-0550-0*.

Canup, R. M. (2004). Dynamics of lunar formation, *Annual Review of Astronomy and Astrophysics* **42**(1): 441–475. *https://doi.org/10.1146/annurev.astro.41.082201.113457*.

Canup, R. M. (2012). Forming a Moon with an Earth-like composition via a giant impact, *Science* **338**(6110): 1052–1055. *https://doi.org/10.1126/science.1226073*.

Canup, R. M. (2014). Lunar-forming impacts: processes and alternatives, *Philosophical Transactions of the Royal Society A: Mathematical, Physical and Engineering Sciences* **372**(2024): 20130175. *https://doi.org/10.1098/rsta.2013.0175*.

Canup, R. M. and Asphaug, E. (2001). Origin of the moon in a giant impact near the end of the Earth's formation, *Nature* **412**(6848): 708–712. *https://doi.org/10.1038/35089010*.

Canup, R. M., Righter, K., Dauphas, N., Pahlevan, K., Ćuk, M., Lock, S. J., Stewart, S. T., Salmon, J., Rufu, R., Nakajima, M. and Magna, T. (2021). Origin of the Moon. *https://arxiv.org/abs/2103.02045*.

Car, R. and Parrinello, M. (1985). Unified approach for molecular dynamics and density-functional theory, *Physical Review Letters* **55**(22): 2471–2474. *https://doi.org/10.1103/physrevlett.55.2471*.

Caracas, R., Kobsch, A., Solomatova, N. V., Li, Z., Soubiran, F. and Hernandez, J.-A. (2021). Analyzing melts and fluids from ab initio molecular dynamics simulations with the UMD package, *Journal of Visualized Experiments* (175): e61534. *https://doi.org/10.3791/61534*.

Chambers, J. (2001). Making more terrestrial planets, *Icarus* **152**(2): 205–224. *https://doi.org/10.1006/icar.2001.6639*.

Chambers, J. E. (2003). Planet Formation, *Treatise on Geochemistry*, Vol. 1, p. 711.

Chambers, J. E. (2013). Late-stage planetary accretion including hit-and-run collisions and fragmentation, *Icarus* **224**(1): 43–56. *https://doi.org/10.1016/j.icarus.2013.02.015*.

Charnoz, S. and Michaut, C. (2015). Evolution of the protolunar disk: Dynamics, cooling timescale and implantation of volatiles onto the earth, *Icarus* **260**: 440–463. *https://doi.org/10.1016/j.icarus.2015.07.018*.

Clayton, R. N., Hurd, J. M. and Mayeda, T. K. (1973). Oxygen isotopic compositions of Apollo 15, 16, and 17 samples, and their bearing on lunar origin and petrogenesis, *Lunar and Planetary Science Conference Proceedings* **4**: 1535. *https://ui.adsabs.harvard.edu/abs/1973LPSC....4.1535C*.

Clayton, R. N. and Mayeda, T. K. (1975). Genetic relations between the Moon and meteorites, *Lunar and Planetary Science Conference Proceedings*, Vol. 6, pp. 1761–1769.

Cramer, C. J., Tolman, W. B., Theopold, K. H. and Rheingold, A. L. (2003). Variable character of O-O and M-O bonding in side-on (η^2) 1:1 metal complexes of O_2, *Proceedings of the National Academy of Sciences* **100**(7): 3635–3640. *https://doi.org/10.1073/pnas.0535926100*.

Cuk, M. and Stewart, S. T. (2012). Making the Moon from a fast-spinning Earth: A giant impact followed by resonant despinning, *Science* **338**(6110): 1047–1052. *https://doi.org/10.1126/science.1225542*.

Darwin, G. H. (1879). XIII. on the precession of a viscous spheroid, and on the remote history of the Earth, *Philosophical Transactions of the Royal Society of London* **170**: 447–538. *https://doi.org/10.1098/rstl.1879.0073*.

Day, J. M. D. and Moynier, F. (2014). Evaporative fractionation of volatile stable isotopes and their bearing on the origin of the Moon, *Philosophical Transactions of the Royal Society A: Mathematical, Physical and Engineering Sciences* **372**(2024): 20130259. *https://doi.org/10.1098/rsta.2013.0259*.

de Clermont Gallerande, E., Cabaret, D., Radtke, G., Sahle, C., Ablett, J., Rueff, J.-P. and Lelong, G. (2020). Quantification of non-bridging oxygens in silicates using x-ray raman scattering, *Journal of Non-Crystalline Solids* **528**: 119715. *https://doi.org/10.1016/j.jnoncrysol.2019.119715*.

Deng, J., Du, Z., Karki, B. B., Ghosh, D. B. and Lee, K. K. M. (2020). A magma ocean origin to divergent redox evolutions of rocky planetary bodies and early atmospheres, *Nature Communications* **11**(1). *https://doi.org/10.1038/s41467-020-15757-0*.

Ding, J., Xu, M., Guan, P. F., Deng, S. W., Cheng, Y. Q. and Ma, E. (2014). Temperature effects on atomic pair distribution functions of melts, *The Journal of Chemical Physics* **140**(6): 064501. *https://doi.org/10.1063/1.4864106*.

Dove, M. T., Keen, D. A., Hannon, A. C. and Swainson, I. P. (1997). Direct measurement of the si-o bond length and orientational disorder in the high-temperature phase of cristobalite, *Physics and Chemistry of Minerals* **24**(4): 311–317. *https://doi.org/10.1007/s002690050043*.

Downs, R. and Palmer, D. (1994). The pressure behavior of α cristobalite, *American Mineralogist* **79**(1-2): 9–14.

Elkins-Tanton, L. T. (2011). Formation of early water oceans on rocky planets, *Astrophysics and Space Science* **332**(2): 359–364. *https://doi.org/10.1007/s10509-010-0535-3*.

Elkins-Tanton, L. T. (2012). Magma oceans in the inner Solar System, *Annual Review of Earth and Planetary Sciences* **40**(1): 113–139. *https://doi.org/10.1146/annurev-earth-042711-105503*.

Fermi, E. (1927). Un metodo statistico per la determinazione di alcune priopriètà dell'atomo, pp. 602–607.

Fischer, R. A., Zube, N. G. and Nimmo, F. (2021). The origin of the moon's earth-like tungsten isotopic composition from dynamical and geochemical modeling, *Nature Communications* **12**(1). *https://doi.org/10.1038/s41467-020-20266-1*.

Fish, J. (2014). *Practical Multiscaling*, John Wiley & Sons, Ltd.

Fish, J., Wagner, G. J. and Keten, S. (2021). Mesoscopic and multiscale modelling in materials, *Nature Materials* **20**(6): 774–786. *https://doi.org/10.1038/s41563-020-00913-0*.

France, L., Ildefonse, B., Koepke, J. and Bech, F. (2010). A new method to estimate the oxidation state of basaltic series from microprobe analyses, *Journal of Volcanology and Geothermal Research* **189**(3-4): 340–346. *https://doi.org/10.1016/j.jvolgeores.2009.11.023*.

Frenkel, D. and Smit, B. (2002). *Understanding Molecular Simulation: From Algorithms to Applications*, Elsevier. *https://doi.org/10.1016/b978-0-12-267351-1.x5000-7*.

Fritsch, D. and Schorr, S. (2020). Climbing Jacob's ladder: A density functional theory case study for $Ag_2ZnSnSe_4$ and $Cu_2ZnSnSe_4$, *Journal of Physics: Energy* **3**(1): 015002. *https://doi.org/10.1088/2515-7655/abc07b*.

Gibbs, G. V., Hamil, M. M., Louisnathan, S. J., Bartell, L. S. and Yow, H. (1972). Correlations between Si-O bond length, Si-O-Si angle and bond overlap populations calculated using extended Hükel molecular orbital theory, *American Mineralogist* **57**(11-12): 1578–1613. *https://pubs.geoscienceworld.org/msa/ammin/article-pdf/57/11-12/1578/4256719/am-1972-1578.pdf*.

Grady, M. M. and Wright, I. (2006). Types of extraterrestrial material available for study, *in* D. S. Lauretta and H. Y. McSween (eds), *Meteorites and the Early Solar System II*, p. 3. *https://ui.adsabs.harvard.edu/abs/2006mess.book....3G*.

Green, E. C., Artacho, E. and Connolly, J. A. (2018). Bulk properties and near-critical behaviour of SiO_2 fluid, *Earth and Planetary Science Letters* **491**: 11–20. *https://doi.org/10.1016/j.epsl.2018.03.015*.

Greenwood, R. C., Barrat, J.-A., Miller, M. F., Anand, M., Dauphas, N., Franchi, I. A., Sillard, P. and Starkey, N. A. (2018). Oxygen isotopic evidence for accretion of Earth's water before a high-energy Moon-forming giant impact, *Science Advances* **4**(3). *https://doi.org/10.1126/sciadv.aao5928*.

Halliday, A. (2014). The origin and earliest history of the Earth, *Treatise on Geochemistry*, Elsevier, pp. 149–211. *https://doi.org/10.1016/b978-0-08-095975-7.00123-6*.

Hallis, L., Anand, M., Greenwood, R., Miller, M., Franchi, I. and Russell, S. (2010). The oxygen isotope composition, petrology and geochemistry of mare basalts: Evidence for large-scale compositional variation in the lunar mantle, *Geochimica et Cosmochimica Acta* **74**(23): 6885–6899. *https://doi.org/10.1016/j.gca.2010.09.023*.

Hartmann, W. K. and Davis, D. R. (1975). Satellite-sized planetesimals and lunar origin, *Icarus* **24**(4): 504–515. *https://doi.org/10.1016/0019-1035(75)90070-6*.

Hauri, E. H., Saal, A. E., Rutherford, M. J. and Orman, J. A. V. (2015). Water in the Moon's interior: Truth and consequences, *Earth and Planetary Science Letters* **409**: 252–264. *https://doi.org/10.1016/j.epsl.2014.10.053*.

Henning, T. and Semenov, D. (2013). Chemistry in protoplanetary disks, *Chemical Reviews* **113**(12): 9016–9042. *https://doi.org/10.1021/cr400128p*.

Hohenberg, P. and Kohn, W. (1964). Inhomogeneous electron gas, *Physical Review* **136**(3B): B864–B871. *https://doi.org/10.1103/physrev.136.b864*.

Hoover, W. G. (1985). Canonical dynamics: Equilibrium phase-space distributions, *Physical Review A* **31**(3): 1695–1697. *https://doi.org/10.1103/physreva.31.1695*.

Iftimie, R., Minary, P. and Tuckerman, M. E. (2005). Ab initio molecular dynamics: Concepts, recent developments, and future trends, *Proceedings of the National Academy of Sciences* **102**(19): 6654–6659. *https://doi.org/10.1073/pnas.0500193102*.

Ireland, T. R., Avila, J., Greenwood, R. C., Hicks, L. J. and Bridges, J. C. (2020). Oxygen isotopes and sampling of the Solar System, *Space Science Reviews* **216**(2). *https://doi.org/10.1007/s11214-020-0645-3*.

Jacobsen, S. B. (2005). The Hf-W isotopic system and the origin of the Earth and Moon, *Annual Review of Earth and Planetary Sciences* **33**(1): 531–570. *https://doi.org/10.1146/annurev.earth.33.092203.122614*.

Jacobsen, S. B. and Harper Jr., C. L. (1996). *Accretion and Early Differentiation History of the Earth Based on Extinct Radionuclides*, American Geophysical Union (AGU), pp. 47–74. *https://agupubs.onlinelibrary.wiley.com/doi/abs/10.1029/GM095p0047*.

Kobsch, A. (2020). *Behavior of feldspars during the Giant Impact*, PhD thesis, École Normale Supérieure de Lyon.

Kobsch, A. and Caracas, R. (2020). The critical point and the supercritical state of alkali feldspars: Implications for the behavior of the crust during impacts, *Journal of Geophysical Research: Planets* **125**(9). *https://doi.org/10.1029/2020je006412*.

Kohn, W. (1999). Nobel lecture: Electronic structure of matter—wave functions and density functionals, *Reviews of Modern Physics* **71**(5): 1253–1266. *https://doi.org/10.1103/revmodphys.71.1253*.

Kohn, W. and Sham, L. J. (1965). Self-consistent equations including exchange and correlation effects, *Physical Review* **140**(4A): A1133–A1138. *https://doi.org/10.1103/physrev.140.a1133*.

Kresse, G. and Furthmüller, J. (1996). Efficiency of ab-initio total energy calculations for metals and semiconductors using a plane-wave basis set, *Computational Materials Science* **6**(1): 15–50. *https://doi.org/10.1016/0927-0256(96)00008-0*.

Kruijer, T. S. and Kleine, T. (2017). Tungsten isotopes and the origin of the moon, *Earth and Planetary Science Letters* **475**: 15–24. *https://doi.org/10.1016/j.epsl.2017.07.021*.

Kühne, T. D. (2014). Second generation Car-Parrinello molecular dynamics, *Wiley Interdisciplinary Reviews: Computational Molecular Science* **4**(4): 391–406. *https://doi.org/10.1002/wcms.1176*.

Lee, J. G. (2017). *Computational materials science: an introduction*, second edition edn, CRC Press, Taylor & Francis Group.

Li, J. and Fei, Y. (2014). Experimental constraints on core composition, *Treatise on Geochemistry*, Elsevier, pp. 527–557. *https://doi.org/10.1016/b978-0-08-095975-7.00214-x*.

Lin, Y., van Westrenen, W. and Mao, H.-K. (2021). Oxygen controls on magmatism in rocky exoplanets, *Proceedings of the National Academy of Sciences* **118**(45). *https://doi.org/10.1073/pnas.2110427118*.

Lindsley, D. H. (ed.) (1991). *Oxide minerals: petrologic and magnetic significance*, Reviews in Mineralogy, Mineralogical Society of America.

Lock, S. J., Bermingham, K. R., Parai, R. and Boyet, M. (2020). Geochemical constraints on the origin of the moon and preservation of ancient terrestrial heterogeneities, *Space Science Reviews* **216**(6). *https://doi.org/10.1007/s11214-020-00729-z*.

Lock, S. J. and Stewart, S. T. (2017). The structure of terrestrial bodies: Impact heating, corotation limits and synestias, *Journal of Geophysical Research: Planets* **122**(5): 950–982. *https://doi.org/10.1002/2016je005239*.

Lock, S. J., Stewart, S. T., Petaev, M. I., Leinhardt, Z., Mace, M. T., Jacobsen, S. B. and Cuk, M. (2018). The origin of the Moon within a terrestrial synestia, *Journal of Geophysical Research: Planets* **123**(4): 910–951. *https://doi.org/10.1002/2017je005333*.

Lodders, K. (2020). Solar elemental abundances. *https://doi.org/10.1093/acrefore/9780190647926.013.145*.

Lorenzen, W. (2012). *Phase transitions in Hydrogen-Helium mixtures*, PhD thesis, Universität Rostock.

Martin, R. M., Reining, L. and Ceperley, D. M. (2016). *Interacting Electrons*, Cambridge University Press. *https://doi.org/10.1017/cbo9781139050807*.

Marx, D. (2006). An introduction to ab initio molecular dynamics simulations, *in* D. M. J. Grotendorst, S. Blügel (ed.), *Computational Nanoscience: Do It Yourself!*, John von Neumann Institute for Computing, pp. 195–244.

Mazurek, A. H., Szeleszczuk, Ł. and Pisklak, D. M. (2021). A review on combination of ab initio molecular dynamics and NMR parameters calculations, *International Journal of Molecular Sciences* **22**(9): 4378. *https://doi.org/10.3390/ijms22094378*.

McDonough, W. F. and Sun, S. S. (1995). The composition of the Earth, *Chemical Geology* **120**(3-4): 223–253.

Melosh, H. J. (2000). A New and Improved Equation of State for Impact Computations, *Lunar and Planetary Science Conference*, p. 1903. *https://ui.adsabs.harvard.edu/abs/2000LPI...31.1903M*.

Melosh, H. J. (2007). A hydrocode equation of state for SiO_2, *Meteoritics & Planetary Science* **42**(12): 2079–2098. *https://doi.org/10.1111/j.1945-5100.2007.tb01009.x*.

Melosh, H. J. (2014). New approaches to the Moon's isotopic crisis, *Philosophical Transactions of the Royal Society A: Mathematical, Physical and Engineering Sciences* **372**(2024): 20130168. *https://doi.org/10.1098/rsta.2013.0168*.

Messenger, S., Sandford, S. and Brownlee, D. (2006). The population of starting materials available for Solar System construction, *in* D. S. Lauretta and H. Y. McSween (eds), *Meteorites and the Early Solar System II*, p. 187.

Mougel, B., Moynier, F. and Göpel, C. (2018). Chromium isotopic homogeneity between the Moon, the Earth and enstatite chondrites, *Earth and Planetary Science Letters* **481**: 1–8. *https://doi.org/10.1016/j.epsl.2017.10.018*.

Mysen, B. O. (1983). The structure of silicate melts, *Annual Review of Earth and Planetary Sciences* **11**(1): 75–97. *https://doi.org/10.1146/annurev.ea.11.050183.000451*.

Nielsen, S. G., Bekaert, D. V. and Auro, M. (2021). Isotopic evidence for the formation of the Moon in a canonical giant impact, *Nature Communications* **12**(1). *https://doi.org/10.1038/s41467-021-22155-7*.

Nosé, S. (1984). A unified formulation of the constant temperature molecular dynamics methods, *The Journal of Chemical Physics* **81**(1): 511–519. *https://doi.org/10.1063/1.447334*.

O'Neil, J. R. and Adami, L. H. (1970). Oxygen isotope analyses of selected Apollo 11 materials, *Geochimica et Cosmochimica Acta Supplement* **1**: 1425. *https://ui.adsabs.harvard.edu/abs/1970GeCAS...1.1425O*.

Pahlevan, K. and Stevenson, D. J. (2007). Equilibration in the aftermath of the lunar-forming giant impact, *Earth and Planetary Science Letters* **262**(3-4): 438–449. *https://doi.org/10.1016/j.epsl.2007.07.055*.

Palme, H. and O'Neill, H. S. C. (2014). Cosmochemical estimates of mantle composition, *Treatise on Geochemistry*, Elsevier, pp. 1–39. *https://doi.org/10.1016/b978-0-08-095975-7.00201-1*.

Perdew, J. P., Burke, K. and Ernzerhof, M. (1996). Generalized gradient approximation made simple, *Physical Review Letters* **77**(18): 3865–3868. *https://doi.org/10.1103/physrevlett.77.3865*.

Rapaport, D. C. (2004). *The Art of Molecular Dynamics Simulation*, Cambridge University Press. *https://doi.org/10.1017/cbo9780511816581*.

Reufer, A., Meier, M. M. M., Benz, W. and Wieler, R. (2012). A hit-and-run giant impact scenario, *Icarus* **221**(1): 296–299. *https://doi.org/10.1016/j.icarus.2012.07.021*.

Rufu, R., Aharonson, O. and Perets, H. B. (2017). A multiple-impact origin for the Moon, *Nature Geoscience* **10**(2): 89–94. *https://doi.org/10.1038/ngeo2866*.

Russell, S. S., Hartmann, L., Cuzzi, J., Krot, A. N., Gounelle, M. and Weidenschilling, S. (2006). Timescales of the solar protoplanetary disk, *in* D. S. Lauretta and H. Y. McSween (eds), *Meteorites and the Early Solar System II*, p. 233.

Saal, A. E., Hauri, E. H., Cascio, M. L., Orman, J. A. V., Rutherford, M. C. and Cooper, R. F. (2008). Volatile content of lunar volcanic glasses and the presence of water in the Moon's interior, *Nature* **454**(7201): 192–195. *https://doi.org/10.1038/nature07047*.

Salmon, J. and Canup, R. M. (2012). Lunar accretion from a roche-interior fluid disk, *The Astrophysical Journal* **760**(1): 83. *https://doi.org/10.1088/0004-637x/760/1/83*.

Schmidt, O. (1959). *A Theory of Earth's Origin*, London: Lawrence and Wishart.

Shearer, C. K., Karner, J., Papike, J. J., Sutton, S. R. and of New Mexico), U. (2004). Oxygen fugacity of mare basalts and the lunar mantle application of a new microscale oxybarometer based on the valence state of vanadium. *https://www.osti.gov/biblio/1008909*.

Söderlind, P. and Young, D. (2018). Assessing density-functional theory for equation-of-state, *Computation* **6**(1): 13. *https://doi.org/10.3390/computation6010013*.

Solomatov, V. (2007). Magma oceans and primordial mantle differentiation, *Treatise on Geophysics*, Elsevier, pp. 91–119. *https://doi.org/10.1016/b978-044452748-6.00141-3*.

Stolper, E. (1977). Experimental petrology of eucritic meteorites, *Geochimica et Cosmochimica Acta* **41**(5): 587–611. *https://doi.org/10.1016/0016-7037(77)90300-3*.

Taylor, L. A., Rossman, G. R. and Qi, Q. (1995). Where has all the lunar water gone?, *Lunar and Planetary Science Conference*, Vol. 26, p. 1399. *https://ui.adsabs.harvard.edu/abs/1995LPI....26.1399T*.

Taylor, S. R. and McLennan, S. M. (2009). *Planetary crusts: their composition, origin and evolution*, Cambridge planetary science, Cambridge University Press, Cambridge, UK ; New York.

Thomas, L. H. (1927). The calculation of atomic fields, *Mathematical Proceedings of the Cambridge Philosophical Society* **23**(5): 542–548. *https://doi.org/10.1017/s0305004100011683*.

Thompson, S. L. and Lauson, H. S. (1974). Improvements in the CHART D radiation-hydrodynamic code III: revised analytic equations of state, (SC-RR-71-0714). *https://www.osti.gov/biblio/4208328*.

Tillotson, J. H. (1962). Metallic equations of state for hypervelocity impact, General Atomic Report GA-3216. Technical Report. *https://ui.adsabs.harvard.edu/abs/1962geat.rept.3216T*.

Touboul, M., Puchtel, I. S. and Walker, R. J. (2012). ^{182}W Evidence for long-term preservation of early mantle differentiation products, *Science* **335**(6072): 1065–1069. *https://doi.org/10.1126/science.1216351*.

Townsend, J. P., Shohet, G. and Cochrane, K. R. (2020). Liquid-vapor coexistence and critical point of Mg_2SiO_4 from ab initio simulations, *Geophysical Research Letters* **47**(17). *https://doi.org/10.1029/2020gl089599*.

Trinquier, A., Elliott, T., Ulfbeck, D., Coath, C., Krot, A. N. and Bizzarro, M. (2009). Origin of nucleosynthetic isotope heterogeneity in the solar protoplanetary disk, *Science* **324**(5925): 374–376. https://doi.org/10.1126/science.1168221.

Urey, H. C. (1966). The capture hypothesis of the origin of the Moon, *The Earth-Moon System*, Springer, pp. 210–212. *https://doi.org/10.1007/978-1-4684-8401-4_13*.

Valley, J. W., Peck, W. H., King, E. M. and Wilde, S. A. (2002). A cool early Earth, *Geology* **30**(4): 351. *https://doi.org/10.1130/0091-7613(2002)030⟨0351:acee⟩2.0.co;2*.

van Mourik, T., Bühl, M. and Gaigeot, M.-P. (2014). Density functional theory across chemistry, physics and biology, *Philosophical Transactions of the Royal Society A: Mathematical, Physical and Engineering Sciences* **372**(2011): 20120488. *https://doi.org/10.1098/rsta.2012.0488*.

Visscher, C. and Fegley, B. (2013). Chemistry of the Protolunar Disk, *44th Annual Lunar and Planetary Science Conference*, Lunar and Planetary Science Conference, p. 1546. *https://ui.adsabs.harvard.edu/abs/2013LPI....44.1546V*.

Wagner, W. and Pruß, A. (2002). The IAPWS formulation 1995 for the thermodynamic properties of ordinary water substance for general and scientific use, *Journal of Physical and Chemical Reference Data* **31**(2): 387–535. *https://doi.org/10.1063/1.1461829*.

Weber, R. C., Lin, P.-Y., Garnero, E. J., Williams, Q. and Lognonné, P. (2011). Seismic detection of the lunar core, *Science* **331**(6015): 309–312. *https://doi.org/10.1126/science.1199375*.

Weinan, E. (2011). *Principles of multiscale modeling*, Cambridge University Press, Cambridge, England.

White, A. D., Knight, C., Hocky, G. M. and Voth, G. A. (2017). Communication: Improved ab initio molecular dynamics by minimally biasing with experimental data, *The Journal of Chemical Physics* **146**(4): 041102. *https://doi.org/10.1063/1.4974837*.

Wiechert, U., Halliday, A. N., Lee, D. C., Snyder, G. A., Taylor, L. A. and Rumble, D. (2001). Oxygen isotopes and the Moon-forming giant impact, *Science* **294**(5541): 345–348. *https://doi.org/10.1126/science.1063037*.

Wilde, S. A., Valley, J. W., Peck, W. H. and Graham, C. M. (2001). Evidence from detrital zircons for the existence of continental crust and oceans on the Earth 4.4 Gyr ago, *Nature* **409**(6817): 175–178. *https://doi.org/10.1038/35051550*.

Wood, J. A. (1986). Moon over Mauna Loa: a review of hypotheses of formation of Earth's Moon., *in* W. K. Hartmann, R. J. Phillips and G. J. Taylor (eds), *Origin of the Moon*, pp. 17–55. *https://ui.adsabs.harvard.edu/abs/1986ormo.conf...17W*.

Woods, N. D., Payne, M. C. and Hasnip, P. J. (2019). Computing the self-consistent field in Kohn-Sham density functional theory, *Journal of Physics: Condensed Matter* **31**(45): 453001. *https://doi.org/10.1088/1361-648x/ab31c0*.

Xiao, B. and Stixrude, L. (2018). Critical vaporization of $MgSiO_3$, *Proceedings of the National Academy of Sciences* **115**(21): 5371–5376. *https://doi.org/10.1073/pnas.1719134115*.

Zaichenko, A., Schröder, D., Janek, J. and Mollenhauer, D. (2020). Pathways to triplet or singlet oxygen during the dissociation of alkali metal superoxides: Insights by multireference calculations of molecular model systems, *Chemistry - A European Journal* **26**(11): 2395–2404. *https://doi.org/10.1002/chem.201904110*.

Zhang, J., Dauphas, N., Davis, A. M., Leya, I. and Fedkin, A. (2012). The proto-Earth as a significant source of lunar material, *Nature Geoscience* **5**(4): 251–255. *https://doi.org/10.1038/ngeo1429*.

List of Figures

List of Tables

Appendix A

Convergence tests

A.1 ENCUT

The cutoff energy was tested at the lowest and highest temperature of interest, meaning at 4000 K and 7000 K. The choice of the density was made based on the same assumption, where the conditions tested were the highest and lowest density value at their specific temperature, meaning (2.33, 0.27 and 0.20 g/cm^3). The energy value was normalized by the number of atoms (216) and by the energy of the highest cutoff energy value. The variation observed in the energy is of less than 1 meV/atom, which lead to the choice of a small cutoff energy (550 eV) in order to increase the speed of the calculations.

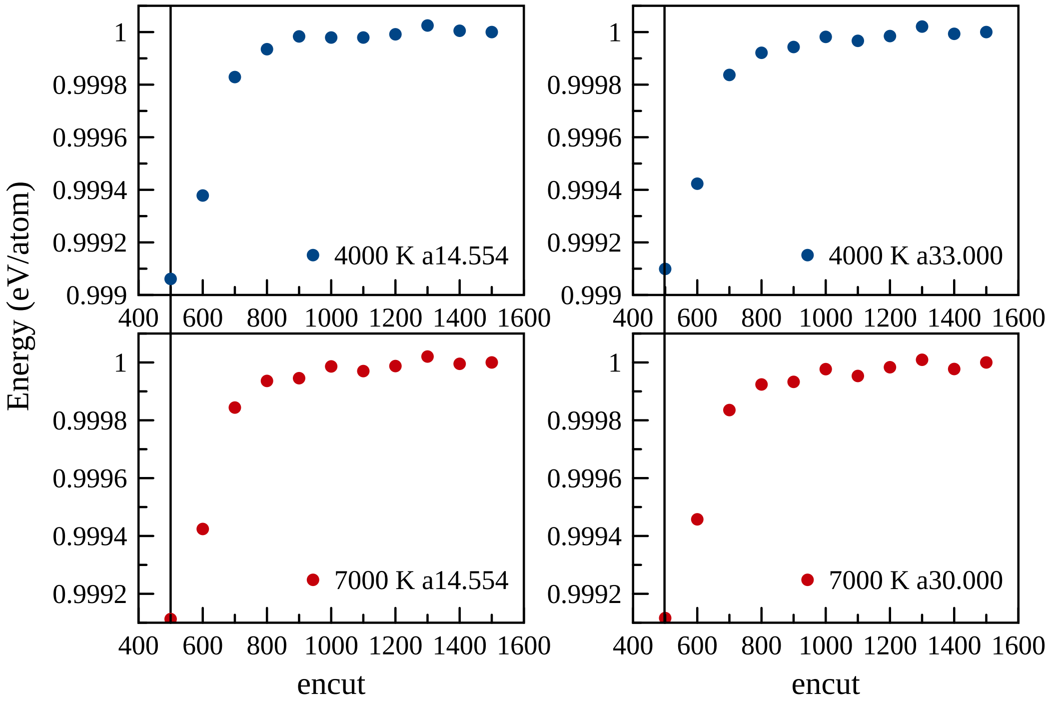

Figure A.1: Convergence test for the cutoff energy (ENCUT). Circles represent the simulation at the chosen cutoff energy. Lattice parameters correspond to 2.33 g/cm^3 (14.554 Å), 0.20 g/cm^3 (a33.000 Å) and 0.27 g/cm^3 (a30.000 Å). The solid line represents the approximate ENCUT value chosen as a parameter in the scope of simulations.

A.2 Number of atoms

The convergence of the energy with respect to the number of atoms was tested with four different configurations: 48, 96, 144 and 216 atoms. The energy was normalized by the number of atoms and compared with respect with the energy value of the system with the highest number of atoms. Here, we obtained a difference of more than 0.02 eV/atom. Considering this, we chose to proceed with simulations containing 216 atoms. The simulation of larger systems is unfeasible in terms of time constraints.

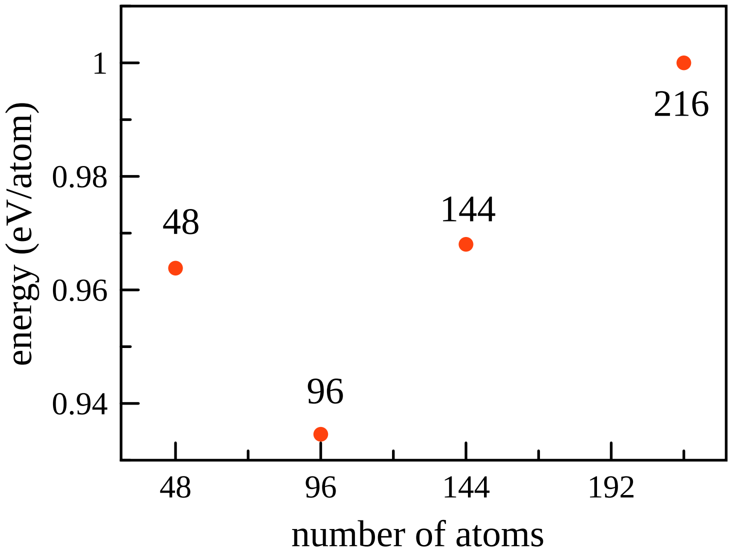

Figure A.2: Convergence test of energy with respect to the number of atoms. The energy is given per atom for a given simulated system. We test systems containing 48, 96, 144 and 216 atoms.

Appendix B

Thermodynamic summary

Thermodynamic variables calculated by applying the methods described in Section 2. Values are given for the bulk dataset of pure SiO_2 setups (Table B.1) and hydrated systems (Table B.2 and B.3).

B.1 Pure SiO_2

Table B.1: Summary of thermodynamic variables at all densities of pure SiO_2 simulations.

Temperature (K)	Density (g/cm^3)	Pressure (GPa)	Internal Energy (eV/atom)	Temperature (K)	Density (g/cm^3)	Pressure (GPa)	Internal Energy (eV/atom)
4000	2.33	2.7077	-7.0110	5000	0.20	0.0866	-5.5974
4000	2.00	0.3693	-6.9642	5500	2.33	5.0527	-6.3046
4000	1.75	-0.3578	-6.9067	5500	2.00	2.4481	-6.2090
4000	1.46	-0.3980	-6.8459	5500	1.75	1.4891	-6.1054
4000	1.23	-0.3462	-6.7659	5500	1.46	0.8267	-6.0008
4000	1.00	-0.2608	-6.6950	5500	1.23	0.5727	-5.9049
4000	0.90	-0.1846	-6.6506	5500	1.00	0.3688	-5.8022
4000	0.68	-0.0950	-6.6027	5500	0.90	0.3453	-5.7727
4000	0.52	-0.0640	-6.5642	5500	0.78	0.2877	-5.7213
4000	0.46	-0.0495	-6.5373	5500	0.68	0.2708	-5.6503
4000	0.41	-0.0288	-6.4677	5500	0.59	0.2594	-5.6031
4000	0.37	-0.0255	-6.4570	5500	0.52	0.2301	-5.5733
4000	0.33	-0.0064	-6.3724	5500	0.46	0.2131	-5.5119
4000	0.27	-0.0027	-6.4273	5500	0.41	0.1851	-5.4856
4000	0.20	0.0016	-6.3376	5500	0.37	0.1797	-5.4898
4500	2.33	3.2169	-6.7764	5500	0.33	0.1650	-5.4278
4500	2.00	0.9215	-6.6943	5500	0.27	0.1579	-5.3912
4500	1.75	0.2119	-6.6326	5500	0.20	0.1272	-5.2682
4500	1.46	-0.0605	-6.5122	6000	2.33	6.1940	-6.0965
4500	1.23	-0.0611	-6.4224	6000	2.00	3.3847	-5.9952

Table B.1 continued from previous page

Temperature (K)	Density (g/cm^3)	Pressure (GPa)	Internal Energy (eV/atom)	Temperature (K)	Density (g/cm^3)	Pressure (GPa)	Internal Energy (eV/atom)
4500	1.00	-0.0605	-6.3715	6000	1.46	1.2663	-5.7939
4500	0.90	-0.0351	-6.3110	6000	1.23	0.8416	-5.7219
4500	0.68	0.0073	-6.2273	6000	1.00	0.6035	-5.6162
4500	0.52	0.0277	-6.1482	6000	0.78	0.4744	-5.4752
4500	0.46	0.0572	-6.0556	6000	0.68	0.4089	-5.4208
4500	0.41	0.0276	-6.1224	6000	0.59	0.3818	-5.3719
4500	0.33	0.0404	-6.0298	6000	0.52	0.3082	-5.4002
4500	0.27	0.0314	-6.0412	6000	0.41	0.2704	-5.3064
4500	0.20	0.0357	-5.9858	6000	0.33	0.2320	-5.2599
5000	2.33	4.0394	-6.5386	6000	0.27	0.2036	-5.1920
5000	2.00	1.5888	-6.4377	7000	2.33	8.4697	-5.7463
5000	1.75	0.7823	-6.3510	7000	2.00	5.1673	-5.6333
5000	1.46	0.3857	-6.2393	7000	1.46	2.2210	-5.4431
5000	1.23	0.2134	-6.1467	7000	1.23	1.5643	-5.3401
5000	1.00	0.1772	-6.0483	7000	1.00	1.0994	-5.2424
5000	0.90	0.1489	-6.0195	7000	0.78	0.7933	-5.1398
5000	0.68	0.1296	-5.9359	7000	0.68	0.6554	-5.1175
5000	0.52	0.1295	-5.7999	7000	0.59	0.5969	-5.0580
5000	0.46	0.1370	-5.7715	7000	0.52	0.5046	-5.0265
5000	0.41	0.1243	-5.7081	7000	0.41	0.4140	-4.9467
5000	0.33	0.1163	-5.6388	7000	0.33	0.3371	-4.8846
5000	0.27	0.0909	-5.7488	7000	0.27	0.2939	-4.8171

B.2 Hydrated systems

Table B.2: Summary of thermodynamic variables at all densities of $9H_2O.72SiO_2$ and $18H_2O.72SiO_2$ simulations.

$9H_2O.72SiO_2$				$18H_2O.72SiO_2$			
Temperature (K)	Density (g/cm^3)	Pressure (GPa)	Internal Energy (eV/atom)	Temperature (K)	Density (g/cm^3)	Pressure (GPa)	Internal Energy (eV/atom)
3000	2.72	9.2315	-6.9996	3000	2.81	12.6817	-6.6934
3000	2.21	2.1894	-7.0510	3000	2.29	4.1784	-6.7701
3000	1.82	0.4683	-7.0617	3000	1.89	1.0657	-6.8031
3000	1.52	-0.2960	-7.0167	3000	1.57	-0.0608	-6.8113
3000	1.28	-0.5316	-7.0109	3000	1.32	-0.3871	-6.7583

3000	1.09	-0.5828	-6.9721	3000	1.13	-0.3488	-6.7505
3000	0.93	-0.3806	-6.9975	3000	0.97	-0.4503	-6.7447
3000	0.81	-0.3005	-6.9210	3000	0.83	-0.3336	-6.7096
3000	0.70	-0.2401	-6.9197	3000	0.73	-0.1655	-6.7202
3000	0.54	-0.1574	-6.9209	3000	0.56	-0.1251	-6.7130
3000	0.42	-0.1165	-6.8771	3000	0.44	-0.1322	-6.6926
3000	0.34	-0.0426	-6.9219	3000	0.35	-0.0697	-6.6084
4000	2.72	9.5219	-6.6679	4000	2.81	13.2465	-6.4068
4000	2.21	2.7279	-6.7208	4000	2.29	4.6785	-6.4576
4000	1.82	0.2806	-6.6789	4000	1.89	1.3782	-6.4479
4000	1.52	-0.1073	-6.5984	4000	1.57	0.2894	-6.4083
4000	1.28	-0.1487	-6.5377	4000	1.32	-0.0404	-6.3550
4000	1.09	-0.2214	-6.5138	4000	1.13	-0.0322	-6.2966
4000	0.93	-0.1470	-6.4722	4000	0.97	-0.0363	-6.2807
4000	0.81	-0.1074	-6.4121	4000	0.83	-0.0179	-6.2414
4000	0.70	-0.0395	-6.4370	4000	0.73	-0.0398	-6.2396
4000	0.54	-0.0367	-6.3524	4000	0.56	-0.0070	-6.1778
4000	0.42	-0.0204	-6.3196	4000	0.44	-0.0100	-6.1470
4000	0.34	0.0022	-6.2126	4000	0.35	0.0138	-6.0733
5000	2.72	11.2396	-6.3032	5000	2.81	15.4476	-6.0795
5000	2.21	4.1241	-6.2694	5000	2.29	6.1715	-6.0711
5000	1.82	1.7441	-6.1586	5000	1.89	2.6336	-6.0077
5000	1.52	0.7954	-6.0582	5000	1.57	1.3080	-5.9222
5000	1.28	0.4046	-5.9951	5000	1.32	0.7585	-5.8535
5000	1.09	0.3115	-5.9350	5000	1.13	0.4863	-5.8360
5000	0.93	0.2741	-5.8408	5000	0.97	0.3528	-5.7223
5000	0.81	0.2045	-5.8120	5000	0.83	0.2883	-5.6816
5000	0.70	0.1793	-5.7372	5000	0.73	0.2432	-5.6332
5000	0.54	0.1542	-5.7172	5000	0.56	0.1981	-5.5746
5000	0.42	0.1366	-5.5804	5000	0.44	0.1791	-5.4868
5000	0.34	0.1252	-5.5078	5000	0.35	0.1365	-5.4735

Table B.3: Summary of thermodynamic variables at all densities of $36H_2O.72SiO_2$ and $72H_2O.72SiO_2$ simulations.

$36H_2O.72SiO_2$				$72H_2O.72SiO_2$			
Temperature (K)	Density (g/cm^3)	Pressure (GPa)	Internal Energy (eV/atom)	Temperature (K)	Density (g/cm^3)	Pressure (GPa)	Internal Energy (eV/atom)
2000	2.45	8.1903	-6.5350	2000	2.28	8.4823	-6.0375
2000	2.02	2.8131	-6.5598	2000	1.90	3.5643	-6.0820
2000	1.68	0.9752	-6.5600	2000	1.60	1.3130	-6.0868

2000	1.42	0.1136	-6.5815	2000	1.36	0.5190	-6.0903
2000	1.20	-0.3530	-6.5687	2000	1.17	0.1334	-6.0749
2000	1.03	-0.7476	-6.5427	2000	1.01	0.0235	-6.0758
2000	0.89	-0.5618	-6.5391	2000	0.88	-0.0730	-6.0694
2000	0.78	-0.4151	-6.5335	2000	0.68	-0.1851	-6.0688
2000	0.60	-0.2942	-6.5286	2000	0.53	-0.0448	-6.0741
2000	0.47	-0.1380	-6.5231	2000	0.43	-0.0838	-6.0627
2000	0.38	-0.0884	-6.5186	3000	2.77	20.2077	-5.7673
3000	2.45	8.7030	-6.3476	3000	2.28	9.4887	-5.8795
3000	2.02	3.1716	-6.4179	3000	1.90	4.2268	-5.9192
3000	1.68	1.0607	-6.4399	3000	1.60	1.9811	-5.9495
3000	1.42	0.3925	-6.4180	3000	1.36	0.8725	-5.9541
3000	1.20	-0.2613	-6.4074	3000	1.17	0.5333	-5.9391
3000	1.03	-0.3431	-6.4063	3000	1.01	0.2623	-5.9338
3000	0.89	-0.1956	-6.3966	3000	0.88	0.1530	-5.9327
3000	0.78	-0.1355	-6.3846	3000	0.68	0.0936	-5.9422
3000	0.60	-0.0502	-6.3888	3000	0.53	0.0358	-5.9403
3000	0.47	-0.0528	-6.3289	3000	0.43	0.0336	-5.9015
3000	0.38	-0.0375	-6.3017	4000	2.77	22.7022	-5.5590
4000	2.45	9.3557	-6.0777	4000	2.28	10.7820	-5.6331
4000	2.02	3.7986	-6.1069	4000	1.90	5.1142	-5.6682
4000	1.68	1.4695	-6.0876	4000	1.60	2.6280	-5.6740
4000	1.42	0.6898	-6.0463	4000	1.36	1.4392	-5.6623
4000	1.20	0.3585	-6.0243	4000	1.17	0.9040	-5.6284
4000	1.03	0.1467	-5.9965	4000	1.01	0.5772	-5.6174
4000	0.89	0.1075	-5.9762	4000	0.88	0.4216	-5.6123
4000	0.78	0.0910	-5.9346	4000	0.68	0.2505	-5.5702
4000	0.60	0.0534	-5.9390	4000	0.53	0.1589	-5.5550
4000	0.47	0.0509	-5.8216	4000	0.43	0.1278	-5.5287
4000	0.38	0.0387	-5.8487	-	-	-	-

Appendix C

Pair distribution function analysis

From pair distribution function analysis of dry silica simulations, we extract mean values of first peaks and troughs for Si-O and O-O pairs, as detqiled in Table C below.

Table C.1: Summary of pair distribution functions peaks and troughs distances.

T (K)	Density (g/cm^3)	1st peak Si-O (Å)	1st min Si-O (Å)	1st peak O-O (Å)	1st min O-O (Å)
4000	2.33	1.636	2.412	2.675	3.615
4000	2.00	1.639	2.459	2.695	3.565
4000	1.75	1.639	2.475	2.695	3.605
4000	1.46	1.638	2.471	2.705	3.605
4000	1.23	1.639	2.500	2.715	3.635
4000	1.00	1.638	2.489	2.725	3.695
4000	0.90	1.636	2.501	2.725	3.695
4000	0.68	1.633	2.492	2.715	3.715
4000	0.52	1.632	2.517	2.715	3.735
4000	0.46	1.630	2.506	2.725	3.745
4000	0.41	1.628	2.501	2.735	3.715
4000	0.37	1.624	2.520	2.745	3.795
4000	0.33	1.626	2.527	2.715	3.775
4000	0.27	1.631	2.518	2.745	3.775
4000	0.20	1.627	2.509	2.715	3.755
4500	2.33	1.636	2.454	2.672	3.717
4500	2.00	1.637	2.479	2.687	3.725
4500	1.75	1.638	2.499	2.695	3.740
4500	1.46	1.634	2.522	2.712	3.778
4500	1.23	1.633	2.542	2.716	3.792
4500	1.00	1.629	2.546	2.716	3.812
4500	0.90	1.626	2.546	2.721	3.843
4500	0.68	1.623	2.578	2.731	3.859
4500	0.52	1.618	2.573	2.745	3.815
4500	0.46	1.611	2.578	2.745	3.896

4500	0.41	1.615	2.576	2.765	3.795
4500	0.33	1.612	2.562	2.743	3.884
4500	0.27	1.611	2.561	2.749	3.895
4500	0.20	1.604	2.573	2.753	3.931
5000	2.33	1.638	2.475	2.672	3.755
5000	2.00	1.637	2.515	2.695	3.769
5000	1.75	1.635	2.540	2.712	3.786
5000	1.46	1.631	2.542	2.722	3.826
5000	1.23	1.629	2.587	2.730	3.843
5000	1.00	1.621	2.583	2.738	3.877
5000	0.90	1.622	2.574	2.742	3.867
5000	0.68	1.614	2.618	2.775	3.985
5000	0.52	1.607	2.627	2.760	3.965
5000	0.46	1.604	2.636	2.758	3.950
5000	0.41	1.602	2.617	2.776	3.987
5000	0.33	1.594	2.640	2.783	3.998
5000	0.27	1.600	2.612	2.785	3.925
5000	0.20	1.587	2.676	2.782	4.024
5500	2.33	1.639	2.497	2.673	3.786
5500	2.00	1.636	2.535	2.711	3.817
5500	1.75	1.633	2.556	2.726	3.840
5500	1.46	1.629	2.580	2.740	3.871
5500	1.23	1.624	2.605	2.746	3.897
5500	1.00	1.618	2.621	2.766	3.924
5500	0.90	1.614	2.612	2.766	3.933
5500	0.78	1.613	2.642	2.770	3.962
5500	0.68	1.606	2.665	2.775	3.978
5500	0.59	1.604	2.658	2.775	3.895
5500	0.52	1.602	2.658	2.779	3.993
5500	0.46	1.597	2.685	2.791	4.029
5500	0.41	1.593	2.712	2.798	4.032
5500	0.37	1.589	2.702	2.792	4.022
5500	0.33	1.589	2.741	2.799	4.083
5500	0.27	1.582	2.705	2.802	4.008
5500	0.20	1.573	2.746	2.824	4.064
6000	2.33	1.640	2.511	2.675	3.813
6000	2.00	1.638	2.558	2.707	3.861
6000	1.46	1.626	2.600	2.757	3.902
6000	1.23	1.625	2.581	2.775	3.895
6000	1.00	1.614	2.637	2.774	3.971
6000	0.78	1.605	2.661	2.835	3.865
6000	0.68	1.603	2.681	2.825	3.885
6000	0.59	1.596	2.693	2.806	4.010
6000	0.52	1.597	2.672	2.793	4.073

6000	0.41	1.588	2.730	2.810	4.108
6000	0.33	1.586	2.686	2.810	4.075
6000	0.27	1.574	2.736	2.829	3.995
7000	2.33	1.642	2.556	2.674	3.851
7000	2.00	1.634	2.562	2.730	3.892
7000	1.46	1.628	2.609	2.778	3.955
7000	1.23	1.621	2.622	2.789	4.006
7000	1.00	1.613	2.655	2.805	4.035
7000	0.78	1.603	2.687	2.818	4.083
7000	0.68	1.605	2.681	2.818	4.112
7000	0.59	1.597	2.735	2.822	4.054
7000	0.52	1.594	2.740	2.832	4.218
7000	0.41	1.590	2.777	2.829	4.204
7000	0.33	1.577	2.828	2.852	4.108
7000	0.27	1.570	2.838	2.856	4.655

Appendix D

Polymerization data

Table D.1: Summary of the polymerization data for every SiO_2 system simulated.

T (K)	Density (g/cm^3)	V (SiO_x)	V (OSi_y)	V_{total}	T (K)	Density (g/cm^3)	V (SiO_x)	V (OSi_y)	V_{total}
4000	2.33	4.023	2.011	2.000	5000	0.20	2.448	1.463	1.674
4000	2.00	3.945	1.973	1.999	5500	2.33	3.969	1.995	1.989
4000	1.75	3.896	1.949	1.999	5500	2.00	3.768	1.906	1.977
4000	1.46	3.826	1.917	1.996	5500	1.75	3.619	1.845	1.962
4000	1.23	3.774	1.893	1.994	5500	1.46	3.448	1.779	1.938
4000	1.00	3.704	1.869	1.982	5500	1.23	3.316	1.732	1.915
4000	0.90	3.664	1.857	1.973	5500	1.00	3.129	1.667	1.877
4000	0.68	3.600	1.823	1.974	5500	0.90	3.052	1.633	1.869
4000	0.52	3.595	1.806	1.991	5500	0.78	2.981	1.616	1.845
4000	0.46	3.517	1.813	1.939	5500	0.68	2.870	1.579	1.818
4000	0.41	3.449	1.770	1.949	5500	0.59	2.754	1.545	1.782
4000	0.37	3.466	1.766	1.963	5500	0.52	2.684	1.529	1.756
4000	0.33	3.342	1.746	1.914	5500	0.46	2.609	1.483	1.759
4000	0.27	3.379	1.781	1.897	5500	0.41	2.546	1.469	1.733
4000	0.20	3.259	1.709	1.907	5500	0.37	2.519	1.458	1.728
4500	2.33	4.029	2.015	1.999	5500	0.33	2.449	1.447	1.693
4500	2.00	3.885	1.950	1.993	5500	0.27	2.281	1.380	1.654
4500	1.75	3.809	1.913	1.992	5500	0.20	2.028	1.295	1.566
4500	1.46	3.687	1.855	1.988	6000	2.33	3.927	1.985	1.978
4500	1.23	3.586	1.826	1.964	6000	2.00	3.737	1.904	1.963
4500	1.00	3.519	1.797	1.958	6000	1.46	3.346	1.745	1.918
4500	0.90	3.455	1.765	1.957	6000	1.23	3.166	1.669	1.897
4500	0.68	3.343	1.733	1.929	6000	1.00	3.024	1.620	1.867
4500	0.52	3.240	1.693	1.914	6000	0.78	2.764	1.551	1.782
4500	0.46	3.074	1.641	1.873	6000	0.68	2.690	1.512	1.779
4500	0.41	3.194	1.670	1.913	6000	0.59	2.561	1.489	1.719
4500	0.33	2.997	1.629	1.840	6000	0.52	2.567	1.476	1.739

Table D.1 continued from previous page

T (K)	Density (g/cm^3)	V (SiO_x)	V (OSi_y)	V_{total}	T (K)	Density (g/cm^3)	V (SiO_x)	V (OSi_y)	V_{total}
4500	0.27	3.011	1.602	1.880	6000	0.41	2.405	1.413	1.702
4500	0.20	2.935	1.562	1.879	6000	0.33	2.226	1.356	1.641
5000	2.33	3.993	2.002	1.994	6000	0.27	2.096	1.334	1.571
5000	2.00	3.831	1.928	1.987	7000	2.33	3.912	1.991	1.965
5000	1.75	3.714	1.878	1.977	7000	2.00	3.578	1.852	1.932
5000	1.46	3.548	1.809	1.961	7000	1.46	3.167	1.692	1.872
5000	1.23	3.452	1.781	1.938	7000	1.23	2.949	1.619	1.822
5000	1.00	3.294	1.719	1.917	7000	1.00	2.775	1.557	1.782
5000	0.90	3.216	1.699	1.894	7000	0.78	2.559	1.484	1.725
5000	0.68	3.120	1.647	1.894	7000	0.68	2.467	1.450	1.702
5000	0.52	2.902	1.590	1.825	7000	0.59	2.403	1.430	1.680
5000	0.46	2.818	1.572	1.793	7000	0.52	2.333	1.399	1.668
5000	0.41	2.724	1.533	1.778	7000	0.41	2.175	1.354	1.606
5000	0.33	2.574	1.470	1.751	7000	0.33	2.033	1.309	1.553
5000	0.27	2.693	1.510	1.783	7000	0.27	1.890	1.262	1.498

ummary of values used in the calculation of the Vn_{total} variable and estimation of ation of hydrated fluids.

Density (g/cm^3)	V (SiO_x)	V (OSi_y)	V_{total}	Density (g/cm^3)	V (SiO_x)	V (OSi_y)	V_{total}
$9H_2O.72SiO_2$				$18H_2O.72SiO_2$			
2.72	4.204	1.982	2.121	2.81	4.324	1.937	2.233
2.21	4.027	1.899	2.120	2.29	4.049	1.817	2.229
1.82	3.923	1.854	2.116	1.89	3.945	1.778	2.218
1.52	3.849	1.815	2.120	1.57	3.872	1.741	2.223
1.28	3.788	1.798	2.106	1.32	3.811	1.719	2.217
1.09	3.764	1.780	2.114	1.13	3.742	1.686	2.219
0.93	3.707	1.757	2.110	0.97	3.723	1.677	2.221
0.81	3.662	1.728	2.119	0.83	3.666	1.665	2.202
0.70	3.656	1.737	2.105	0.73	3.669	1.651	2.222
0.54	3.598	1.724	2.087	0.56	3.575	1.634	2.188
0.42	3.568	1.719	2.076	0.44	3.553	1.633	2.175
0.34	3.382	1.639	2.063	0.35	3.416	1.584	2.157
$36H_2O.72SiO_2$				$72H_2O.72SiO_2$			
2.45	4.182	1.720	2.432	2.77	4.607	1.642	2.806
2.02	4.011	1.659	2.417	2.28	4.213	1.545	2.726
1.68	3.901	1.624	2.402	1.90	4.044	1.496	2.703
1.42	3.835	1.603	2.393	1.60	3.911	1.451	2.696

1.20	3.785	1.580	2.396	1.36	3.860	1.450	2.662
1.03	3.757	1.566	2.398	1.17	3.774	1.418	2.662
0.89	3.725	1.568	2.375	1.01	3.732	1.401	2.663
0.78	3.631	1.560	2.327	0.88	3.724	1.426	2.611
0.60	3.635	1.571	2.313	0.68	3.603	1.409	2.558
0.47	3.465	1.516	2.285	0.53	3.605	1.417	2.545
0.38	3.467	1.518	2.284	0.43	3.521	1.398	2.518

Appendix E

Mean square displacements

Plots of mean square displacements of all systems as calculated in this work.

E.1 Pure SiO_2

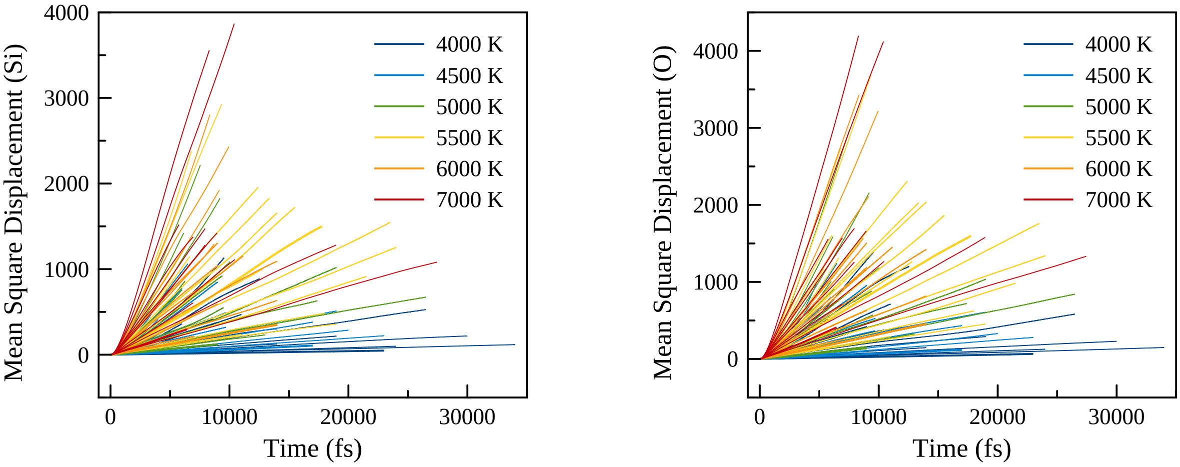

(a) Silicon

(b) Oxygen

Figure E.1: Mean square displacement of (a) silicon and (b) oxygen on pure silica simulations at all temperatures and all densities. Different colors represent simulations at different temperatures, where dark blue indicate calculations at 4000 K, light blue is 4500 K, green is 5000 K, yellow is 5500 K, orange is 6000 K and red is 7000 K results.

E.2 Hydrated systems

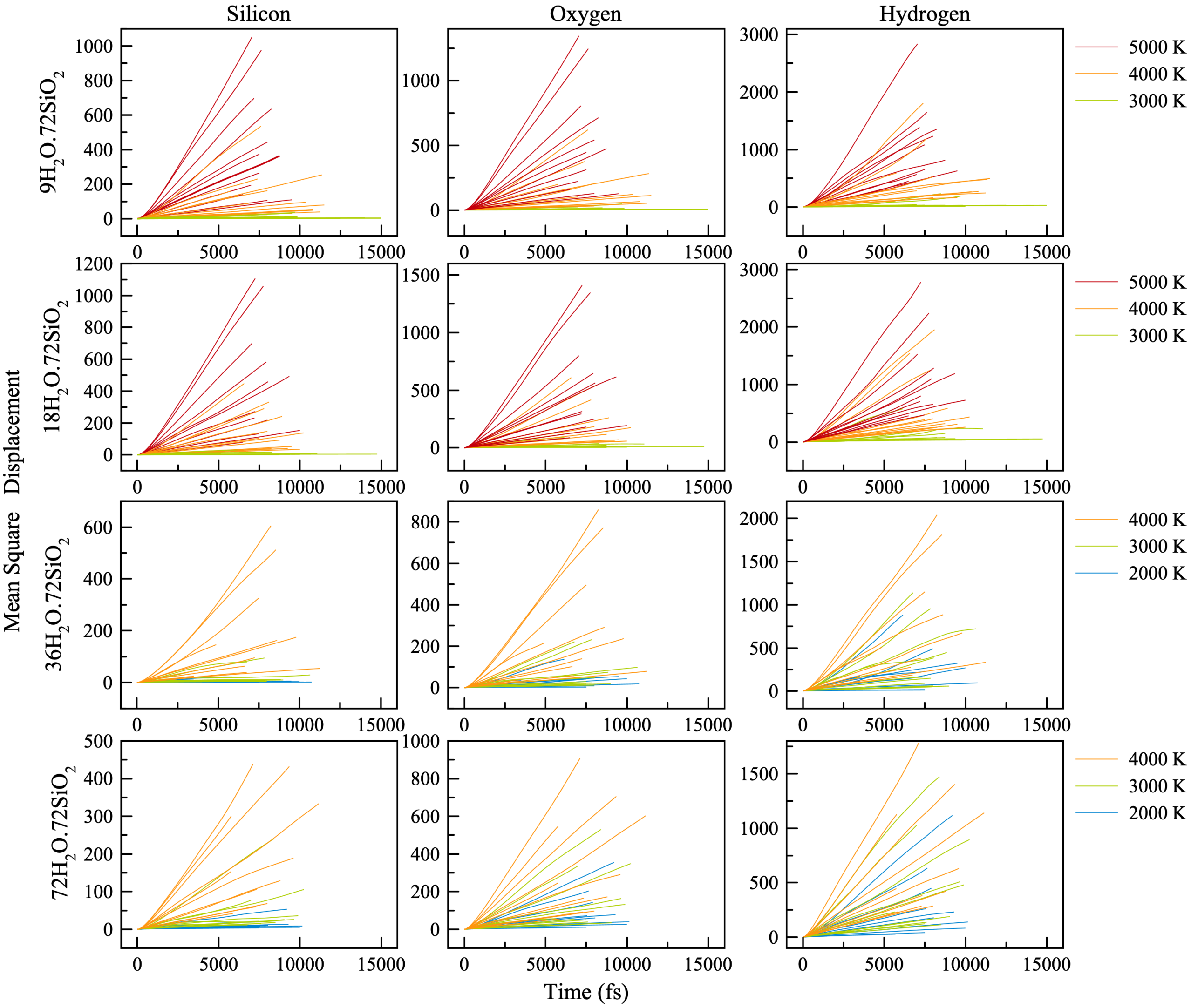

Figure E.2: Mean square displacements of hydrous fluids. Curves represent the displacement of individual densities at given temperatures, for silicon (left panels), oxygen (middle panels) and hydrogen (right panels). Colors indicate temperature, where red is 5000 K, orange is 4000 K, green is 3000 K and blue is 2000 K.

Appendix F

Diffusion coefficients

F.1 Pure SiO_2

Table F.1: Self-diffusion coefficients values of silicon and oxygen atoms on pure SiO_2 systems in the ensemble of simulated conditions.

T (K)	Density (g/cm^3)	D_{Si} (m^2/s)	D_O (m^2/s)	T (K)	Density (g/cm^3)	D_{Si} (m^2/s)	D_O (m^2/s)
4000	2.33	3.39E-09	4.56E-09	5000	0.20	5.16E-07	7.00E-07
4000	2.00	5.03E-09	7.07E-09	5500	2.33	3.19E-08	3.98E-08
4000	1.75	5.61E-09	7.03E-09	5500	2.00	3.57E-08	4.38E-08
4000	1.46	6.74E-09	8.72E-09	5500	1.75	4.53E-08	5.80E-08
4000	1.23	1.25E-08	1.25E-08	5500	1.46	7.12E-08	7.55E-08
4000	1.00	1.48E-08	1.70E-08	5500	1.23	8.73E-08	9.38E-08
4000	0.90	1.89E-08	2.55E-08	5500	1.00	1.09E-07	1.25E-07
4000	0.68	3.32E-08	3.51E-08	5500	0.90	1.46E-07	1.54E-07
4000	0.52	3.78E-08	5.81E-08	5500	0.78	1.33E-07	1.67E-07
4000	0.46	7.52E-08	1.16E-07	5500	0.67	1.87E-07	2.00E-07
4000	0.41	7.20E-08	8.03E-08	5500	0.59	1.97E-07	2.49E-07
4000	0.37	8.43E-08	7.73E-08	5500	0.52	2.34E-07	2.59E-07
4000	0.33	1.04E-07	1.54E-07	5500	0.46	2.74E-07	3.22E-07
4000	0.27	1.28E-07	1.76E-07	5500	0.41	2.99E-07	3.36E-07
4000	0.20	2.03E-07	2.53E-07	5500	0.36	3.07E-07	3.80E-07
4500	2.33	1.05E-08	1.16E-08	5500	0.33	3.56E-07	4.73E-07
4500	2.00	1.37E-08	1.79E-08	5500	0.27	5.55E-07	6.94E-07
4500	1.75	1.59E-08	2.03E-08	5500	0.20	6.09E-07	7.17E-07
4500	1.46	2.39E-08	2.67E-08	6000	2.33	4.18E-08	5.45E-08
4500	1.23	3.72E-08	4.30E-08	6000	2.00	5.18E-08	6.12E-08
4500	1.00	4.48E-08	5.37E-08	6000	1.46	7.45E-08	9.65E-08
4500	0.90	5.65E-08	6.47E-08	6000	1.23	1.12E-07	1.19E-07
4500	0.67	8.68E-08	9.29E-08	6000	1.00	1.33E-07	1.74E-07
4500	0.52	8.95E-08	1.42E-07	6000	0.78	1.73E-07	2.21E-07

Table F.1 continued from previous page

T (K)	Density (g/cm^3)	D_{Si} (m^2/s)	D_O (m^2/s)	T (K)	Density (g/cm^3)	D_{Si} (m^2/s)	D_O (m^2/s)
4500	0.46	1.78E-07	1.75E-07	6000	0.67	2.00E-07	2.24E-07
4500	0.41	1.64E-07	1.84E-07	6000	0.59	2.50E-07	2.85E-07
4500	0.33	2.28E-07	2.33E-07	6000	0.52	2.50E-07	3.06E-07
4500	0.27	2.96E-07	3.39E-07	6000	0.41	3.63E-07	4.02E-07
4500	0.20	2.78E-07	3.44E-07	6000	0.33	4.23E-07	5.59E-07
5000	2.33	2.31E-08	2.61E-08	6000	0.27	5.78E-07	7.28E-07
5000	2.00	2.23E-08	2.99E-08	7000	2.33	6.72E-08	8.10E-08
5000	1.75	2.97E-08	4.15E-08	7000	2.00	7.82E-08	1.07E-07
5000	1.46	4.24E-08	5.26E-08	7000	1.46	1.15E-07	1.37E-07
5000	1.23	6.12E-08	7.07E-08	7000	1.23	1.48E-07	1.76E-07
5000	1.00	9.04E-08	8.94E-08	7000	1.00	1.80E-07	2.03E-07
5000	0.90	9.41E-08	9.97E-08	7000	0.78	2.76E-07	2.67E-07
5000	0.67	1.71E-07	1.62E-07	7000	0.67	2.71E-07	3.16E-07
5000	0.52	1.83E-07	2.03E-07	7000	0.59	3.19E-07	3.67E-07
5000	0.46	2.33E-07	2.55E-07	7000	0.52	3.55E-07	3.88E-07
5000	0.41	2.19E-07	2.88E-07	7000	0.41	4.69E-07	4.71E-07
5000	0.33	3.45E-07	4.04E-07	7000	0.33	6.46E-07	6.93E-07
5000	0.27	4.07E-07	4.58E-07	7000	0.27	7.66E-07	8.76E-07

F.2 Hydrated systems

Table F.2: Self-diffusion coefficients values of silicon, oxygen and hydrogen atoms on $9H_2O.72SiO_2$ and $18H_2O.72SiO_2$ systems in the ensemble of simulated conditions.

$9H_2O.72SiO_2$					$18H_2O.72SiO_2$				
T (K)	Density (g/cm^3)	D_{Si} (m^2/s)	D_O (m^2/s)	D_H (m^2/s)	T (K)	Density (g/cm^3)	D_{Si} (m^2/s)	D_O (m^2/s)	D_H (m^2/s)
3000	2.72	5.25E-10	8.52E-10	7.40E-09	3000	2.81	1.17E-09	1.77E-09	1.20E-08
3000	2.21	3.37E-10	5.34E-10	3.46E-09	3000	2.29	7.21E-10	1.24E-09	8.68E-09
3000	1.82	1.47E-10	3.94E-10	3.66E-09	3000	1.89	3.60E-10	7.57E-10	5.11E-09
3000	1.52	2.83E-10	4.36E-10	2.79E-09	3000	1.57	2.54E-11	7.31E-11	1.37E-08
3000	1.28	1.95E-10	3.25E-10	1.68E-09	3000	1.32	2.14E-10	1.46E-09	1.01E-08
3000	1.09	4.21E-10	6.48E-10	2.94E-09	3000	1.13	3.65E-10	1.01E-09	5.58E-09
3000	0.93	3.41E-10	3.22E-09	4.62E-08	3000	0.97	5.85E-10	3.73E-09	2.80E-08
3000	0.81	9.90E-10	1.47E-09	4.85E-09	3000	0.83	1.98E-09	5.40E-09	3.31E-08
3000	0.70	1.80E-09	1.57E-09	4.04E-09	3000	0.73	7.27E-10	2.31E-09	1.39E-08
3000	0.54	1.29E-09	1.59E-09	3.69E-09	3000	0.56	7.68E-10	5.40E-09	4.22E-08
3000	0.42	5.20E-09	7.10E-09	3.08E-08	3000	0.44	3.23E-09	6.34E-09	3.67E-08

Table F.2 continued from previous page

$9H_2O.72SiO_2$					$18H_2O.72SiO_2$				
T (K)	Density (g/cm^3)	D_{Si} (m^2/s)	D_O (m^2/s)	D_H (m^2/s)	T (K)	Density (g/cm^3)	D_{Si} (m^2/s)	D_O (m^2/s)	D_H (m^2/s)
3000	0.34	4.76E-09	5.26E-09	9.24E-09	3000	0.35	8.56E-09	2.66E-08	1.71E-07
4000	2.72	5.71E-09	7.60E-09	3.80E-08	4000	2.81	8.03E-09	1.07E-08	5.30E-08
4000	2.21	4.78E-09	6.19E-09	3.24E-08	4000	2.29	5.66E-09	9.50E-09	4.30E-08
4000	1.82	5.39E-09	7.35E-09	2.92E-08	4000	1.89	7.18E-09	1.02E-08	4.32E-08
4000	1.52	7.69E-09	9.67E-09	4.18E-08	4000	1.57	8.83E-09	1.17E-08	5.13E-08
4000	1.28	1.16E-08	1.61E-08	7.31E-08	4000	1.32	1.77E-08	2.17E-08	5.93E-08
4000	1.09	1.51E-08	1.87E-08	4.04E-08	4000	1.13	2.22E-08	2.75E-08	6.97E-08
4000	0.93	2.12E-08	2.34E-08	6.84E-08	4000	0.97	2.30E-08	3.20E-08	8.54E-08
4000	0.81	3.77E-08	4.20E-08	7.22E-08	4000	0.83	3.09E-08	3.76E-08	7.64E-08
4000	0.70	3.48E-08	4.18E-08	1.06E-07	4000	0.73	4.61E-08	4.91E-08	1.08E-07
4000	0.54	4.75E-08	5.85E-08	1.78E-07	4000	0.56	6.42E-08	9.13E-08	2.83E-07
4000	0.42	5.34E-08	8.71E-08	4.34E-07	4000	0.44	7.11E-08	1.18E-07	4.29E-07
4000	0.34	1.28E-07	1.45E-07	2.62E-07	4000	0.35	1.20E-07	1.63E-07	4.13E-07
5000	2.72	1.95E-08	2.17E-08	1.12E-07	5000	2.81	2.01E-08	2.25E-08	1.18E-07
5000	2.21	2.20E-08	2.67E-08	1.06E-07	5000	2.29	2.55E-08	3.24E-08	1.25E-07
5000	1.82	3.60E-08	4.10E-08	1.11E-07	5000	1.89	3.04E-08	4.03E-08	1.05E-07
5000	1.52	4.71E-08	5.32E-08	1.35E-07	5000	1.57	4.58E-08	5.12E-08	1.43E-07
5000	1.28	5.92E-08	6.97E-08	1.46E-07	5000	1.32	5.43E-08	6.95E-08	1.63E-07
5000	1.09	6.96E-08	9.18E-08	1.58E-07	5000	1.13	6.36E-08	7.22E-08	1.81E-07
5000	0.93	8.62E-08	1.01E-07	2.43E-07	5000	0.97	8.82E-08	1.14E-07	2.17E-07
5000	0.81	9.52E-08	1.17E-07	2.70E-07	5000	0.83	9.46E-08	1.17E-07	2.64E-07
5000	0.70	1.34E-07	1.51E-07	2.88E-07	5000	0.73	1.26E-07	1.37E-07	2.25E-07
5000	0.54	1.70E-07	1.93E-07	3.29E-07	5000	0.56	1.73E-07	1.92E-07	3.58E-07
5000	0.42	2.20E-07	2.82E-07	3.59E-07	5000	0.44	2.41E-07	3.10E-07	4.94E-07
5000	0.34	2.60E-07	3.30E-07	7.19E-07	5000	0.35	2.68E-07	3.39E-07	6.67E-07

Table F.3: Self-diffusion coefficients values of silicon, oxygen and hydrogen atoms on $36H_2O.72SiO_2$ and $72H_2O.72SiO_2$ systems in the ensemble of simulated conditions.

$36H_2O.72SiO_2$					$72H_2O.72SiO_2$				
T (K)	Density (g/cm^3)	D_{Si} (m^2/s)	D_O (m^2/s)	D_H (m^2/s)	T (K)	Density (g/cm^3)	D_{Si} (m^2/s)	D_O (m^2/s)	D_H (m^2/s)
2000	2.45	1.97E-10	4.63E-10	2.16E-09	2000	2.28	7.35E-10	2.31E-09	8.81E-09
2000	2.02	8.03E-11	4.06E-10	2.94E-09	2000	1.90	7.96E-10	2.37E-09	7.03E-09
2000	1.68	1.08E-10	1.56E-09	1.18E-08	2000	1.60	6.63E-10	4.00E-09	1.37E-08
2000	1.42	3.28E-11	1.45E-09	9.41E-09	2000	1.36	1.04E-09	5.97E-09	2.24E-08
2000	1.20	9.91E-11	2.35E-09	1.30E-08	2000	1.17	1.91E-09	1.20E-08	3.59E-08

Table F.3 continued from previous page

$36H_2O.72SiO_2$					$72H_2O.72SiO_2$				
T (K)	Density (g/cm^3)	D_{Si} (m^2/s)	D_O (m^2/s)	D_H (m^2/s)	T (K)	Density (g/cm^3)	D_{Si} (m^2/s)	D_O (m^2/s)	D_H (m^2/s)
2000	1.03	2.37E-10	6.62E-09	4.17E-08	2000	1.01	1.84E-09	1.33E-08	4.18E-08
2000	0.89	2.52E-10	8.96E-09	5.10E-08	2000	0.88	1.35E-09	1.49E-08	5.69E-08
2000	0.78	6.36E-10	9.12E-09	1.05E-07	2000	0.68	1.49E-09	2.88E-08	9.10E-08
2000	0.60	4.32E-10	8.75E-09	5.35E-08	2000	0.53	3.41E-09	4.50E-08	1.39E-07
2000	0.47	5.10E-09	1.86E-08	8.69E-08	2000	0.43	9.62E-09	6.69E-08	2.14E-07
2000	0.38	6.63E-09	4.09E-08	2.50E-07	3000	2.77	4.73E-09	6.30E-09	3.49E-08
3000	2.45	2.01E-09	3.60E-09	2.07E-08	3000	2.28	3.40E-09	6.15E-09	2.18E-08
3000	2.02	9.40E-10	2.32E-09	1.18E-08	3000	1.90	3.15E-09	8.17E-09	2.97E-08
3000	1.68	6.63E-10	1.90E-09	8.46E-09	3000	1.60	4.69E-09	1.06E-08	2.62E-08
3000	1.42	1.52E-09	2.83E-09	9.29E-09	3000	1.36	2.34E-09	1.21E-08	3.45E-08
3000	1.20	1.21E-09	4.24E-09	3.07E-08	3000	1.17	3.89E-09	1.60E-08	6.78E-08
3000	1.03	1.51E-09	5.38E-09	3.55E-08	3000	1.01	5.61E-09	2.16E-08	8.08E-08
3000	0.89	1.72E-09	1.28E-08	7.76E-08	3000	0.88	2.76E-09	2.61E-08	8.54E-08
3000	0.78	1.79E-09	9.56E-09	7.82E-08	3000	0.68	1.62E-08	5.69E-08	1.49E-07
3000	0.60	3.14E-09	1.40E-08	1.21E-07	3000	0.53	1.73E-08	8.23E-08	2.53E-07
3000	0.47	2.08E-08	5.08E-08	2.07E-07	3000	0.43	5.06E-08	1.11E-07	3.10E-07
3000	0.38	2.17E-08	5.71E-08	2.96E-07	4000	2.77	1.21E-08	1.57E-08	6.52E-08
4000	2.45	8.10E-09	1.14E-08	4.79E-08	4000	2.28	1.42E-08	2.01E-08	5.93E-08
4000	2.02	9.61E-09	1.40E-08	4.48E-08	4000	1.90	1.35E-08	2.05E-08	6.44E-08
4000	1.68	1.16E-08	1.80E-08	5.14E-08	4000	1.60	2.53E-08	3.29E-08	7.98E-08
4000	1.42	1.55E-08	2.51E-08	6.98E-08	4000	1.36	2.41E-08	3.69E-08	8.60E-08
4000	1.20	2.11E-08	3.09E-08	8.70E-08	4000	1.17	3.40E-08	5.19E-08	1.11E-07
4000	1.03	2.97E-08	4.01E-08	1.16E-07	4000	1.01	4.46E-08	7.09E-08	1.30E-07
4000	0.89	3.15E-08	5.75E-08	1.76E-07	4000	0.88	4.96E-08	9.06E-08	1.70E-07
4000	0.78	5.36E-08	7.75E-08	1.73E-07	4000	0.68	7.97E-08	1.29E-07	2.58E-07
4000	0.60	7.45E-08	1.15E-07	2.68E-07	4000	0.53	8.98E-08	1.65E-07	3.41E-07
4000	0.47	1.06E-07	1.60E-07	3.79E-07	4000	0.43	1.05E-07	2.19E-07	4.21E-07
4000	0.38	1.27E-07	1.77E-07	4.21E-07					

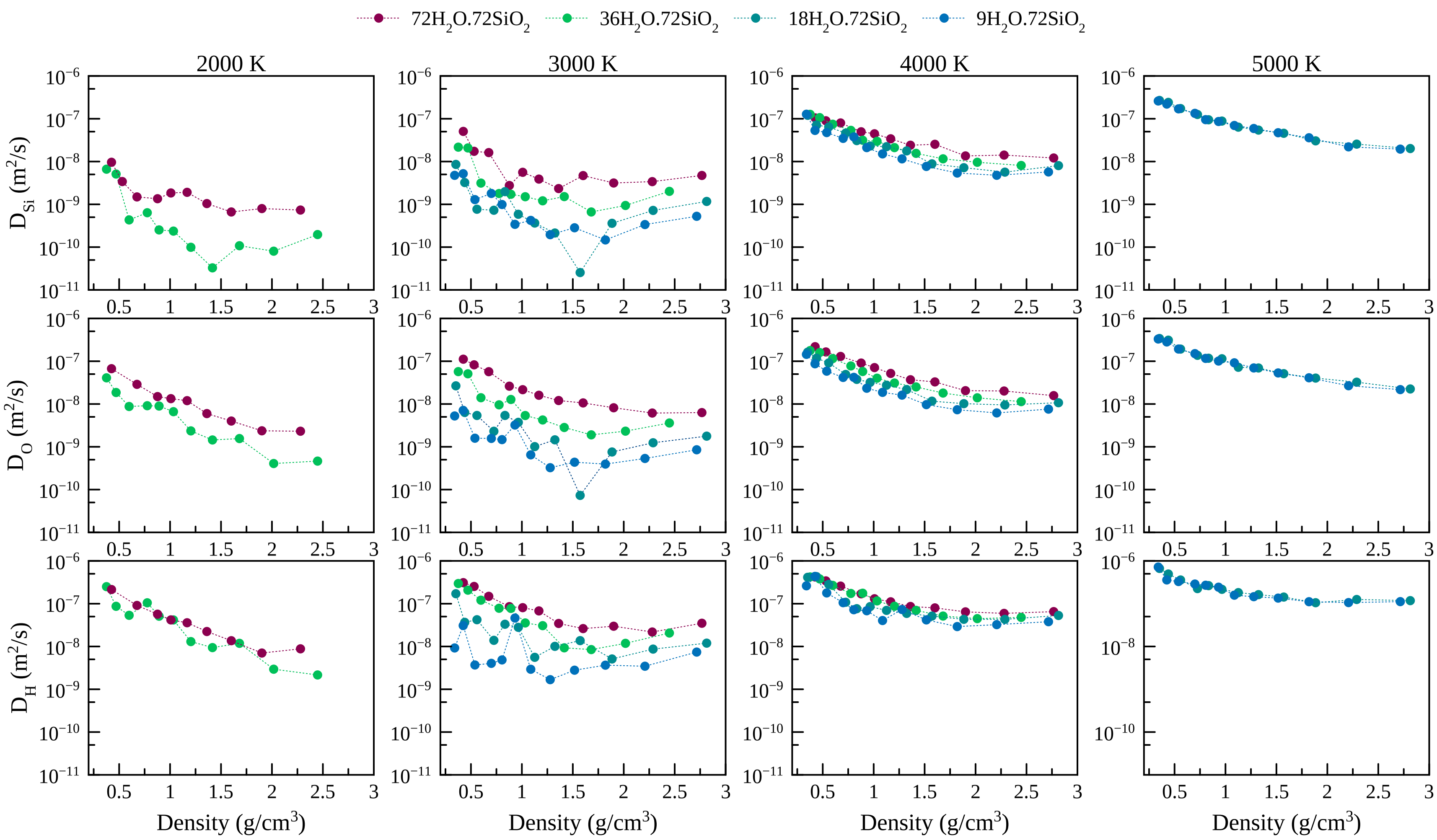

Figure F.1: Complete dataset of self-diffusion coefficients of Si, O and H for every hydrated silicate system at all temperatures.